Solitons in Magnetic Systems

PhD thesis by Sebastiano Bresolin

Supervisors:
Alessio Recati
Franco Dalfovo

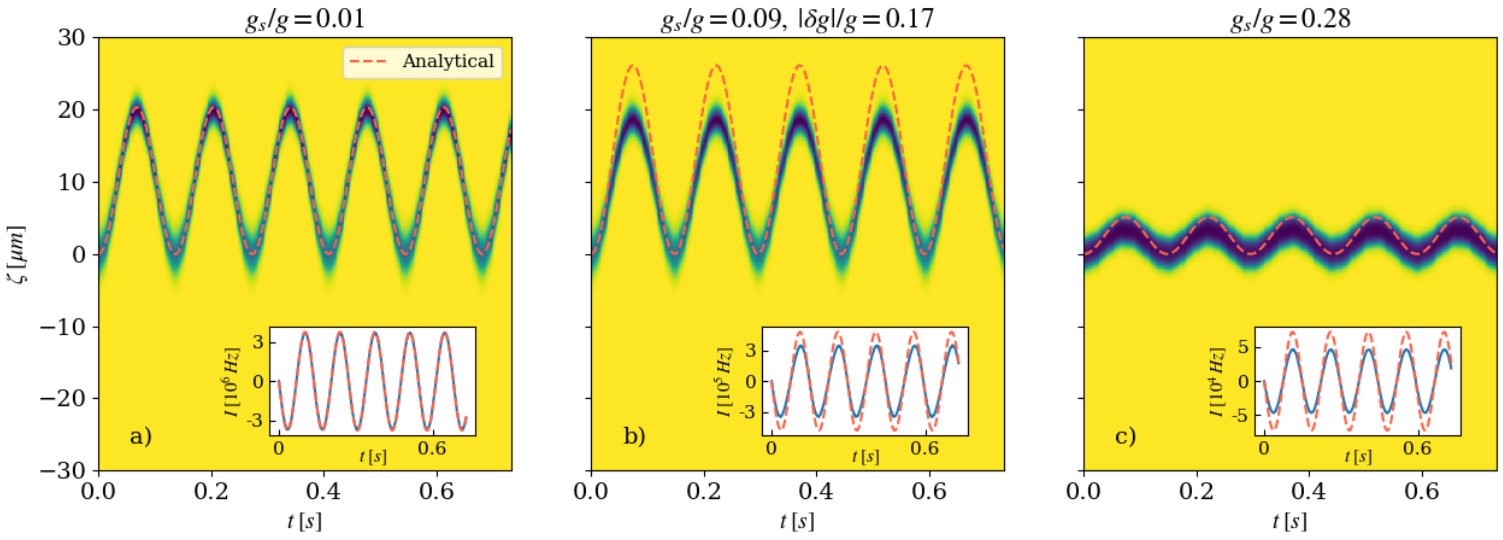

UNIVERSITÀ
DI TRENTO

Contents

1 Abstract **2**

2 Introduction **4**
2.1 Bose-Einstein condensation 4
2.2 Condensate mixtures 8
2.3 Mapping to ferromagnetic system 16
2.3.1 Non-homogeneous systems 22
2.4 Integrability 23
2.5 Solitons 25
2.5.1 Solitons in the GPE 26
2.5.2 Easy-plane solitons 28
2.5.3 Easy-axis solitons 30

3 Magnetic soliton oscillations as Josephson physics **36**
3.1 Values of the parameters used in the numerical simulations 43
3.2 Equal and Opposite Potentials 43
3.3 Adiabatic soliton motion 44
3.4 The miscible case 45

4 Soliton collisions and transmission at an interface **48**
4.1 Two-body collisions 48
4.2 Three-body collisions 53
4.3 Solitons impinging on sharp density gradients 54

5 Preliminary results and outlook **62**
5.1 Soliton bound states 62
5.2 Effects of coherent coupling 68
5.2.1 Immiscible 68
5.2.2 Miscible 77
5.3 Conclusion 81

Appendix: Numerical methods **82**

References **98**

1 Abstract

This doctoral thesis reports the results of theoretical research in the field of Bose-Einstein condensate (BEC) mixtures, with its main focus on the dynamics of solitons in such systems and with reference to the formal and physical analogies between BEC mixtures and the classical magnetization dynamics of solid-state ferromagnets. Its structure comprises an introductory chapter which lays out the physical characteristics of the systems under examination and the theoretical framework used to treat them, as well as motivating the specific avenues of research pursued, and several further chapters detailing the original contributions resulting from said research.

The premise of viewing condensate dynamics as analogous to those of another system in order to learn more about both is central to the motivations of the lines of research pursued in this thesis: specifically, it explores some aspects of the links between the behavior of mixtures of two condensates of different bosonic species with repulsive interactions and that of the magnetization distribution within classical solid-state ferromagnets. The equations used to model the two systems are respectively a pair of coupled Gross-Pitaevskii equations (GPEs) for the two condensate order parameters and the Landau-Lifshitz equation (LLE) for the magnetization vector (taken as a continuous field). Throughout the thesis, all results will depend on the use of these equations through a combination of analytical and numerical methods, and they will concern the case of a single spatial dimension.

In the Manakov limit of equal interaction constants, the coupled Gross-Pitaevskii equations become equivalent to the Landau-Lifshitz equation and a formally exact mapping is established between the two systems. In this way, exact results from the simpler Landau-Lifshitz equation can be used as starting points to understand the richer physics of condensate mixtures at generic values of the interaction constants. This approach is particularly fruitful in light of the fact that the LLE is integrable, a property it shares with the Gross-Pitaevskii equation but not with the coupled GPEs describing a mixture. Integrability of the equation means that its initial-value problem is in principle exactly solvable, a fact related to the presence of infinitely many conservation laws in the system. The theory of integrable equations predicts the existence of special exact solutions called solitons, which are characterized by simple collisional properties, and whose behavior is the focus of the original contributions presented herein. In particular, we focus on solitons of the LLE which take the form of solitary waves and map them into approximate solutions of the coupled GPEs, obtaining solitary waves whose properties may deviate from those of true solitons. The results discussed in this thesis examine the behavior of such solitary waves in situations where integrability is broken, both by virtue of the finite distance of the mixture's parameters from the Manakov limit and as the result of the addition of external fields.

The first original result presented (chapter 3) concerns a phenomenon predicted for magnetic solitons in the easy-axis LLE: when such a soliton is subjected to a uniform magnetic field gradient, it undergoes oscillations with a sinusoidal trajectory. A physical explanation for this periodicity was missing, motivating our contribution, in which we demonstrate that the same phenomenon is to be expected in a BEC mixture and interpret it as an example of Josephson physics, with the soliton acting as a mobile barrier for the current in the background condensate. This interpretation motivates us to predict that the oscillations are not peculiar to the exact soliton solution but depend essentially on the presence of a more generic mobile barrier. Working in terms of condensate mixtures allows us to shed light on the different behavior of magnetic solitons in an easy-plane ferromagnet already noted in the literature, as well as to examine the effect of going further away from the mixing-demixing transition; we find that the oscillatory effect is quite robust.

Chapter 4 presents results on the collisions of solitary waves in the miscible condensate mixture using the soliton solution of the easy-plane LLE as a starting point. Comparisons of numerical solutions of the coupled GPEs with the analytical results for magnetic solitons find good agreement in the velocity-dependent

phase shifts in two-body collisions with the analytical prediction near the Manakov limit, and deviations are observed further from this limit. Simulations of three-body collisions show a remarkable preservation, far from the Manakov limit, of the two-body nature of solitary wave interactions, a property which is guaranteed for true solitons but may be expected to be lost as integrability is broken. Finally, the behavior of solitary waves encountering the interface between two regions of different constant densities is considered, with the inhomogeneity of the system breaking integrability. This direction is motivated by the robustness, observed numerically, of such solitary waves as individual quasiparticles even in the presence of large deviations from integrability. We expect that if the preservation of the solitary wave in this scenario as a quasiparticle can be taken for granted, then its transmission or reflection across the interface and its outgoing velocity can be predicted from a simple energy conservation argument; simulations confirm the validity of the quasiparticle picture.

Finally, some preliminary results are discussed in chapter 5. In the first part, we find numerically that pairs of solitary waves in the condensate mixture may form bound states of finite lifetime, whose duration and outcome depend strongly on initial conditions. We relate this phenomenon to existing literature, in which it is understood as a general feature of solitary wave collisions in non-integrable systems, exhibiting distinctive characteristics such as a fractal structure in the dynamics. The second part of the chapter is devoted to the effects of coherent coupling on solitary waves. The coherently coupled GPEs can still be mapped to the LLE, but the additional term, which takes the form of a uniform transverse field, breaks integrability, and leads to a rich variety of new phenomena, including domain wall motion, the expansion of spin domains, and acceleration or periodic motion of single solitary waves.

2 Introduction

2.1 Bose-Einstein condensation

We begin by stating the basic elements of a theoretical description of Bose-Einstein condensates (BEC) and their mixtures, delineating the context of our work and establishing the tools we will rely on, the most central of which is the Gross-Pitaevskii equation. A more complete discussion may be found in reference [1]. The full quantum many-body description of a gas of N_{at} interacting bosons is in general a complicated problem. However, such a system undergoes the Bose-Einstein condensation phase transition, due to its bosonic statistics, when its temperature drops below some critical value T_c. A significantly simpler description is possible in this phase, which is characterized by the macroscopic occupation of one single-particle quantum state[1] $\left|\phi_0\right\rangle$ from among some complete set of states $\{\left|\phi_j\right\rangle\}$. One natural choice of basis is suggested by the fact that an important property of the gas in the condensed phase is the presence of off-diagonal long-range order, a property manifested in its one-body density matrix

$$n^{(1)}(\vec{r},\vec{r}') \equiv < \hat{\Psi}^\dagger(\vec{r})\hat{\Psi}(\vec{r}') >, \tag{1}$$

where $\hat{\Psi}(\vec{r})$ is the field operator which annihilates a particle at the position $\vec{r}$. If we choose the states $\{\left|\phi_j\right\rangle\}$ so that their wavefunctions satisfy the eigenvalue equation

$$\int n^{(1)}(\vec{r},\vec{r}')\phi_j(\vec{r}')\,\mathrm{d}^3r' = n_j\phi_j(\vec{r}), \tag{2}$$

then we can write

$$n^{(1)}(\vec{r},\vec{r}') = \sum_j n_j\phi_j^*(\vec{r}')\phi_j(\vec{r}') = N_0\phi_0^*(\vec{r}')\phi_0(\vec{r}') + \sum_{j\neq 0} n_j\phi_j^*(\vec{r}')\phi_j(\vec{r}'),$$

where n_j is the occupation number of the state $\left|\phi_j\right\rangle$, and in the condensed phase all $n_{j\neq 0}$ are of order 1 whereas N_0 is of order N_{at}. Therefore, in the thermodynamic limit implying $N_{\mathrm{at}} \to \infty$, the contribution of the condensate ϕ_0 remains finite even for $\left|\vec{r}-\vec{r}'\right| \to \infty$, while that of the sum with $j \neq 0$ vanishes. Thus $\lim_{|\vec{r}-\vec{r}'|\to\infty} n^{(1)}(\vec{r},\vec{r}')$ is non-zero, whereas it vanishes in the non-condensed phase where no single state is macroscopically occupied. This is the property called off-diagonal long-range order.

The general description of the Bose gas is in terms of the bosonic field operator $\hat{\Psi}(\vec{r})$ whose dynamics is governed by a many-body Hamiltonian, but the macroscopic occupation of the condensate state allows us to formulate a mean-field description of the system by means of the Bogoliubov approximation. We rewrite the field operator using the eigenfunctions of $n^{(1)}$ as

$$\hat{\Psi}(\vec{r}) = \sum_j \phi_j(\vec{r})\hat{a}_j = \phi_0(\vec{r})\hat{a}_0 + \sum_{j\neq 0}\phi_j(\vec{r})\hat{a}_j,$$

where $\hat{a}_j$ is the annihilation operator for the state $\left|\psi_j\right\rangle$. The Bogoliubov approximation consists in replacing $\hat{a}_0$ and its adjoint $\hat{a}_0^\dagger$ with the c-number $\sqrt{N_0}$, ignoring their operator nature. This is a good approximation for large condensate occupation numbers, since in this regime

$$\frac{[\hat{a}_0,\hat{a}_0^\dagger]}{<\hat{a}_0\hat{a}_0^\dagger>} = \frac{1}{N_0} \ll 1.$$

[1] or of several such states, but we will focus on the simplest case.

Defining $\Psi_0(\vec{r}) \equiv \sqrt{N_0}\phi_0(\vec{r})$, the field operator in the Bogoliubov approximation is

$$\hat{\Psi}(\vec{r}) = \Psi_0(\vec{r}) + \delta\hat{\Psi}(\vec{r}),$$

where $\delta\hat{\Psi}(\vec{r}) \equiv \sum_{j\neq 0} \phi_j(\vec{r})\hat{a}_j$ can be viewed as fluctuations of the field operator over its expectation value Ψ_0. The complex function Ψ_0 is the order parameter of the Bose-Einstein condensation transition, since the field operator has vanishing expectation value in the non-condensed phase. It takes a definite value thanks to the spontaneous breaking by the BEC transition of the $U(1)$ symmetry present in the system's many-body Hamiltonian (see below, Eq. 4): specifically, the symmetry breaking is reflected in the fact that the complex $\Psi_0 = \sqrt{n_0}e^{i\varphi_0}$ possesses a definite phase φ_0. To obtain our mean-field theory, we neglect $\delta\hat{\Psi}$. Since both thermal fluctuations and quantum fluctuations (due to the interactions between bosons) contribute to the finite occupation of non-condensate states, this approximation is valid for low-temperature, weakly interacting gases, i.e.

$$T \ll T_c \text{ and } \bar{n}\left|a_s\right|^3 \ll 1,$$

where $\bar{n}$ is the average density of the gas and a_s is the s-wave scattering length of two-body boson interactions. The latter condition can be obtained under the further assumption of diluteness of the gas,

$$\bar{n}r_0^3 \ll 1,$$

where r_0 is the range of the interparticle interaction. This allows N-body interactions with $N > 2$ to be neglected, since they occur much more rarely, and the effect of the two-body interaction to be entirely captured by the s-wave scattering length through the Born approximation for low-energy scattering - essentially replacing the actual interaction with a contact interaction having the correct scattering length. This simplification also affects the theory of the dynamics of the gas, which in the Heisenberg picture are given for the time-dependent field operator $\hat{\Psi}(\vec{r}, t)$ by the Heisenberg equation

$$i\hbar\frac{\mathrm{d}\hat{\Psi}}{\mathrm{d}t} = [\hat{\Psi}, \hat{H}] \tag{3}$$

with the Hamiltonian

$$\hat{H} = \int \hat{\Psi}^\dagger(\vec{r}, t)\left(-\frac{\hbar^2}{2m}\nabla^2 + \tilde{V}_{\text{ext}}(\vec{r})\right)\hat{\Psi}(\vec{r}, t)\,\mathrm{d}^3r + \frac{1}{2}\int \hat{\Psi}^\dagger(\vec{r}', t)\hat{\Psi}^\dagger(\vec{r}, t)V_{\text{int}}(\vec{r} - \vec{r}')\hat{\Psi}(\vec{r}', t)\hat{\Psi}(\vec{r}, t)\,\mathrm{d}^3r\,\mathrm{d}^3r' \tag{4}$$

for bosons of mass m, where we include a time-independent external potential $\tilde{V}_{\text{ext}}$ and the two-body interaction potential V_{int}. Using the approximations specified above, we take

$$V_{\text{int}}(\vec{r} - \vec{r}') = \tilde{g}\delta(\vec{r} - \vec{r}'), \quad \tilde{g} \equiv \frac{4\pi\hbar^2 a_s}{m},$$

leading to

$$\hat{H} = \int \hat{\Psi}^\dagger(\vec{r}, t)\left(-\frac{\hbar^2}{2m}\nabla^2 + \tilde{V}_{\text{ext}}(\vec{r})\right)\hat{\Psi}(\vec{r}, t)\,\mathrm{d}^3r + \frac{\tilde{g}}{2}\int \hat{\Psi}^\dagger(\vec{r}, t)\hat{\Psi}^\dagger(\vec{r}, t)\hat{\Psi}(\vec{r}, t)\hat{\Psi}(\vec{r}, t)\,\mathrm{d}^3r\,.$$

Inserting this into the Heisenberg equation, using the Bogoliubov approximation $\hat{\Psi}(\vec{r}, t) = \Psi(\vec{r}, t) + \delta\hat{\Psi}(\vec{r}, t)$ and neglecting the fluctuation term $\delta\hat{\Psi}(\vec{r}, t)$ yields, at lowest order[2], the Gross-Pitaevskii equation (GPE) for the evolution of the time-dependent condensate order parameter $\Psi(\vec{r}, t)$:

[2]Higher-order approximations in $\delta\hat{\Psi}$ can be used to describe perturbative deviations from mean-field theory at finite temperatures, see for example [2].

$$i\hbar\frac{\partial\Psi}{\partial t} = -\frac{\hbar^2}{2m}\nabla^2\Psi + \tilde{V}_{\text{ext}}\Psi + \tilde{g}|\Psi|^2\Psi, \tag{5}$$

which takes the form of a nonlinear Schrödinger equation (NLSE), with the normalization condition

$$\int |\Psi|^2 \mathrm{d}^3 r = N_0.$$

This is the basic form of the equation our discussion will be based on, but we will focus on the one-dimensional version, applicable in practice to quasi-one-dimensional atomic condensates. These are obtained by trapping the condensate in a highly anisotropic external potential, which confines it much less tightly in one direction - whose coordinate we will call ζ - than in the perpendicular directions. For concreteness, suppose that $\tilde{V}_{\text{ext}}$ is such that the typical length scale $a_\perp$ associated with the transverse confinement is much smaller than its counterpart a_ζ in the longitudinal direction. Then, under the further condition

$$\left(\frac{a_s}{a_\perp}\right) \ll n|a_s|^3,$$

it is possible to assume that the dynamics of the condensate in the transverse directions are frozen out, i.e. that the order parameter decomposes as $\Psi(\vec{r},t) = \psi_\perp(\vec{r}_\perp)\psi(\zeta,t)$, where $\psi_\perp$ is independent of time and normalized to 1. Inserting this into Eq. 5, we obtain the one-dimensional Gross-Pitaevskii equation

$$i\hbar\frac{\partial\psi}{\partial t} = -\frac{\hbar^2}{2m}\frac{\partial^2\psi}{\partial\zeta^2} + V_{\text{ext}}\psi + g|\psi|^2\psi, \tag{6}$$

where

$$g = \tilde{g}\int |\psi_\perp|^4 \mathrm{d}^2 r_\perp$$

is the renormalized interaction strength, $V_{\text{ext}}(\zeta) \equiv \int \tilde{V}_{\text{ext}}|\psi_\perp|^2 \mathrm{d}^2 r_\perp$, and we have eliminated a constant energy shift. Note that if $\tilde{V}_{\text{ext}} = V_\perp(\vec{r}_\perp) + V_\parallel(\zeta)$, then $V_{\text{ext}} = V_\parallel$ and $\psi_\perp$ is the ground state of $V_\perp$. In the typical case of harmonic transverse confinement, $\tilde{V}_{\text{ext}} = (m\omega_\perp^2/2)r_\perp^2 + V_\parallel$, we can approximate $\psi_\perp$ by the ground state of the quantum harmonic oscillator (thanks to the assumption $a_s \ll a_\perp$) to obtain the estimate $g = 2\hbar\omega_\perp a_s$ for the renormalized interaction strength, where $a_\perp = \sqrt{\hbar/m\omega_\perp}$.

The GPE can be obtained from the Euler-Lagrange equations for the Lagrangian density

$$\begin{aligned}\mathcal{L} =& \frac{i\hbar}{2}\left(\psi\frac{\partial\psi^*}{\partial t} - \psi^*\frac{\partial\psi}{\partial t}\right) - \mathcal{E} \\ =& \hbar n\frac{\partial\varphi}{\partial t} - \mathcal{E}\end{aligned} \tag{7}$$

with the Gross-Pitaevskii energy density

$$\begin{aligned}\mathcal{E} =& \frac{\hbar^2}{2m}\left|\frac{\partial\psi}{\partial\zeta}\right|^2 + V_{\text{ext}}|\psi|^2 + \frac{g}{2}|\psi|^4 \\ =& \frac{\hbar^2}{2m}\left(n^2(\frac{\partial\varphi}{\partial\zeta})^2 + \frac{1}{4}(\frac{\partial n}{\partial\zeta})^2\right) + V_{\text{ext}}n + \frac{g}{2}n^2.\end{aligned} \tag{8}$$

The time-independent GPE

$$\mu\psi_0 = -\frac{\hbar^2}{2m}\frac{\partial^2\psi_0}{\partial\zeta^2} + V_{\text{ext}}\psi_0 + g\left|\psi_0\right|^2\psi_0 \tag{9}$$

describes stationary states, in which the condensate density is constant in time and the time dependence of the order parameter satisfies $\psi(\zeta,t) = \psi_0(\zeta)e^{-i\mu\hbar/t}$ with real ψ_0, where

$$\mu \equiv \frac{\partial E}{\partial N_0} = \frac{1}{N_0}\int \frac{\hbar^2}{2m}\left|\frac{\partial\psi_0}{\partial\zeta}\right|^2 + V_{\text{ext}}\left|\psi_0\right|^2 + g\left|\psi_0\right|^4 \mathrm{d}\zeta$$

is the chemical potential. The time-independent equation can be obtained from the time-dependent version by inserting the stationary form for ψ into it. The GPE makes it easy to see that the condensate has a natural length scale

$$\xi \equiv \frac{\hbar}{\sqrt{2mgn}} \tag{10}$$

which expresses a balance between dispersion and nonlinearity (as it can be identified as the length scale on which spatial variations contribute an energy density comparable to that associated with a background density n), and so is typical of a stationary inhomogeneous condensate. It is called the healing length because it is the typical size of the region in which the condensate recovers its uniform density in the vicinity of a hard wall forcing the density to vanish.

A useful representation for the order parameter is in terms of the density and phase, which are real functions and directly related to physical quantities, the phase being the velocity potential for the condensate: $v = (\hbar/m)\partial_\zeta\varphi$. By inserting the definition $\psi(\zeta,t) = \sqrt{n(\zeta,t)}e^{i\varphi(\zeta,t)}$ into the GPE, we obtain the following equivalent system:

$$\begin{cases} \dfrac{\partial n}{\partial t} + \dfrac{\hbar}{m}\dfrac{\partial}{\partial\zeta}\left(n\dfrac{\partial\varphi}{\partial\zeta}\right) = 0 & \text{(11a)} \\ \hbar\dfrac{\partial\varphi}{\partial t} = -\dfrac{\hbar^2}{2m}\left(\dfrac{1}{\sqrt{n}}\dfrac{\partial^2\sqrt{n}}{\partial\zeta^2} - (\dfrac{\partial\varphi}{\partial\zeta})^2\right) - gn - V_{\text{ext}}. & \text{(11b)} \end{cases}$$

The first equation in this system has a straightforward interpretation as a continuity equation expressing particle number conservation, which is associated with the system's $U(1)$ symmetry. Indeed, it can be expressed as $\partial_t n + \partial_\zeta j = 0$ with the definition of the particle current $j = nv = n(\hbar/m)\partial_\zeta\varphi$.

The GPE can be used to study the elementary excitations of the condensate. This can be done by inserting into it the ansatz $\psi(\zeta,t) = \psi_0(\zeta) + h(\zeta,t)$ for the order parameter, where ψ_0 is the ground state solution and h is a small-amplitude perturbation whose positive- and negative-frequency components are then found to obey coupled differential equations. For a homogeneous system ($V_{\text{ext}} = 0$), ψ_0 is a constant and h can be decomposed into plane waves. The differential equations become algebraic ones, and the GPE can then be solved analytically in the limit of small perturbations by keeping only up to linear terms in $|h|$, leading to the following relationship between the wavenumber k and the frequency ω of small-amplitude perturbations:

$$\hbar\omega(k) = \sqrt{\frac{\hbar^2k^2}{2m}\left(\frac{\hbar^2k^2}{2m} + 2gn\right)}. \tag{12}$$

This is the well-known Bogoliubov dispersion relation, which corresponds to the fact that the (quantum) Hamiltonian of the system can be diagonalized under the Bogoliubov approximation by the definition of creation and annihilation operators for quasiparticles each of which contributes the energy $\epsilon(p = \hbar k) = \hbar\omega(k)$. The ground state of the gas is found to be the vacuum of such quasiparticles, and excited states to have finite quasiparticle population. Within the Gross-Pitaevskii theory, these quasiparticles appear as small-amplitude waves above the ground state of the condensate. Their spectrum is asymptotically quadratic for $|k| \to \infty$ and linear for $|k| \to 0$. The latter behavior means that the elementary excitations are phonon-like at small momenta $\hbar k$, with the speed of sound

$$c = \lim_{p\to 0} \frac{\partial \epsilon}{\partial p} = \lim_{k\to 0} \frac{\partial \omega}{\partial k} = \sqrt{\frac{gn}{m}}.$$

This gapless branch of excitations can be interpreted as the Goldstone mode associated with the spontaneous breaking of $U(1)$ symmetry.

2.2 Condensate mixtures

We are interested in the physics of mixtures of two Bose-Einstein condensates. Here the two gases are composed of distinguishable species of bosons, so that each undergoes its own condensation transition and the system can be studied as a mixture of the two components. In the general case, the two species will have different masses, but we will restrict ourselves to the case in which they have the same mass m: this is achievable with condensates of atoms of the same atomic species in two different hyperfine levels. When the temperature is low and both gases are dilute, the same arguments given in the previous section lead to the mean-field description of the system in terms of the two order parameters $\psi_1(\zeta, t)$, $\psi_2(\zeta, t)$ obeying the coupled Gross-Pitaevskii equations

$$\begin{cases} i\hbar \dfrac{\partial \psi_1}{\partial t} = -\dfrac{\hbar^2}{2m}\dfrac{\partial^2 \psi_1}{\partial \zeta^2} + V_{\mathrm{ext},1}(\zeta)\psi_1 + g_{11}|\psi_1|^2\psi_1 + g_{12}|\psi_2|^2\psi_1 + \hbar\Omega\psi_2 \\ i\hbar \dfrac{\partial \psi_2}{\partial t} = -\dfrac{\hbar^2}{2m}\dfrac{\partial^2 \psi_2}{\partial \zeta^2} + V_{\mathrm{ext},2}(\zeta)\psi_2 + g_{22}|\psi_2|^2\psi_2 + g_{12}|\psi_1|^2\psi_2 + \hbar\Omega^*\psi_1. \end{cases} \tag{13}$$

These can be obtained from the Lagrangian density

$$\mathcal{L} = \sum_{j=1,2} \frac{i\hbar}{2}\left(\psi_j^* \frac{\partial \psi_j}{\partial t} - \psi_j \frac{\partial \psi_j^*}{\partial t}\right) - \mathcal{E} \tag{14}$$

with the energy density

$$\mathcal{E}[\psi_1, \psi_2] = \sum_{j=1,2}\left[\frac{\hbar^2}{2m}\left|\frac{\partial \psi_j}{\partial \zeta}\right|^2 + V_{\mathrm{ext},j}|\psi_j|^2 + \sum_{k=1,2}\frac{g_{jk}}{2}\left|\psi_j\right|^2|\psi_k|^2\right] + \hbar(\Omega\psi_1^*\psi_2 + \Omega^*\psi_2^*\psi_1), \tag{15}$$

where $g_{21} \equiv g_{12}$. Each order parameter can be written in the form $\psi_j = \sqrt{n_j}e^{i\varphi_j}$, where n_j is the density of the j-th component and $(\hbar/m)\partial_\zeta\varphi_j$ its velocity field. We will often make use of the total density $n \equiv n_1 + n_2$, density $w = (n_1 - n_2)/n$, total phase $\Phi = \varphi_1 + \varphi_2$, and relative phase $\varphi_2 - \varphi_1$. Since the s-wave scattering length relative to a scattering event between two particles depends on their species, we must distinguish in

the mean-field coupling terms between the intraspecies interaction constants g_{11} and g_{22}, which may differ between the two species, and an interspecies interaction constant g_{12}. We will assume these are all positive, corresponding to repulsive two-body interactions. This provides a more complex parameter space than for the single-component GPE, and it will be convenient to define

$$g \equiv \frac{g_{11} + g_{22}}{2}, \quad \delta g \equiv g_{11} - g_{22}, \quad g_s \equiv g_{12} - g. \tag{16}$$

We have also included the coherent, or Rabi, coupling terms proportional to the complex parameter Ω. These allow for the possibility of particles switching from one species to another. Physically, this may be realized by shining an electromagnetic wave on the condensates, which allows atoms to transition from one hyperfine state to the other when the external field's frequency is close to the transition frequency. The quantity Ω is related to the amplitude of the wave, and is complex in accordance with the fact that the wave has a certain (arbitrary) phase. The coupled GPE system will constitute our model throughout this thesis.

The physics of the condensate mixture is similar to that of the single condensate, but is also much richer. We will discuss the differences assuming at first $\Omega = 0$, and then consider the coherently coupled case. From a general point of view, the system is obtained through two concurrent BEC transitions, in which a total $U(1) \times U(1)$ symmetry is spontaneously broken. This breaking corresponds to the definition of the two phases φ_j, and implies the continuity equations

$$\frac{\partial n_j}{\partial t} + \frac{\partial}{\partial \zeta}\left(n v_j\right) = \frac{\partial n_j}{\partial t} + \frac{\hbar}{m}\frac{\partial}{\partial \zeta}\left(n \frac{\partial \varphi_j}{\partial \zeta}\right) = 0$$

and the conservation of particle number N_j for both components. It is also visible in the existence of two separate chemical potentials

$$\mu_j = \frac{\partial E}{\partial N_j} = \frac{\partial}{\partial N_j} \int \mathcal{E}\, \mathrm{d}\zeta\,. \tag{17}$$

These appear in the stationary versions of Eq. 13, which follow from the ansatz $\psi_j(\zeta, t) = \psi_j(\zeta) e^{-i\mu_j t/\hbar}$ as

$$\begin{cases} \mu_1 \psi_1 = -\dfrac{\hbar^2}{2m}\dfrac{\partial^2 \psi_1}{\partial \zeta^2} + V_{\mathrm{ext},1}(\zeta)\psi_1 + g_{11}|\psi_1|^2\psi_1 + g_{12}|\psi_2|^2\psi_1 \\ \mu_2 \psi_2 = -\dfrac{\hbar^2}{2m}\dfrac{\partial^2 \psi_2}{\partial \zeta^2} + V_{\mathrm{ext},2}(\zeta)\psi_2 + g_{22}|\psi_2|^2\psi_2 + g_{12}|\psi_1|^2\psi_2. \end{cases} \tag{18}$$

Indeed, the chemical potentials can be seen as the Lagrange multipliers allowing the derivation of the stationary mean-field coupled GPEs by minimization of the energy E subject to the constraint of conservation of N_j - or equivalently by minimization of the grand canonical energy $G = E - \mu_1 N_1 - \mu_2 N_2$. This brings us to a discussion of the ground state of the condensate mixture, which exhibits a phase transition in the parameter space of the couplings g_{ij} (see, for example, [3]). We show this for a homogeneous system[3], in which the external potentials are zero, by examining the stability of the energy density $\mathcal{E}$ under the assumption that the condensate densities are uniform. The phases are then both arbitrary constants in the ground state, since they enter only in the kinetic term of the energy density. The Hessian matrix of $\mathcal{E}[n_1, n_2]$, under these conditions, is

[3]The homogeneous case is of direct experimental relevance thanks to the development of box-shaped potentials (see e.g. [4]), and will be our main focus. The more typical case of harmonically trapped condensates can in many cases of interest be related to the homogeneous system by way of the local density approximation.

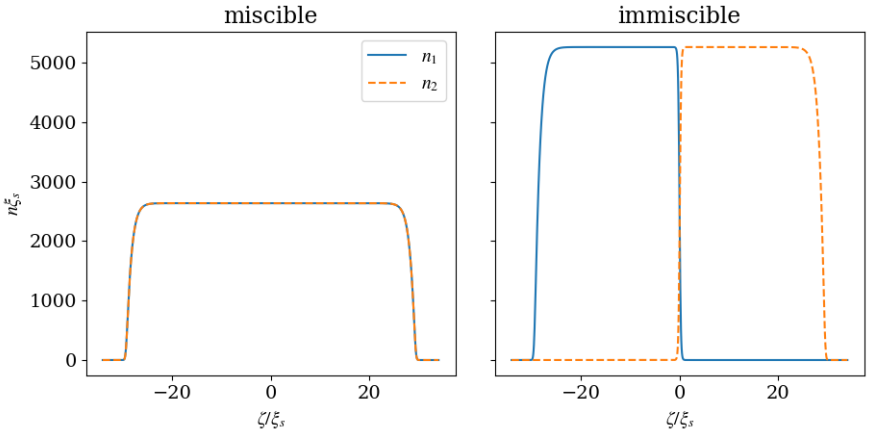

Figure 1: Condensate densities in the numerically computed ground state in a box potential in the miscible regime (left) and in the immiscible regime (right). In both cases we set $g_{11} = g_{22}$. Lengths are given in units of the spin healing length ξ_s and densities in units of its inverse. The densities in the miscible regime are idential to each other.

$$H[\mathcal{E}] \equiv \begin{pmatrix} \frac{\partial^2 \mathcal{E}}{\partial n_1^2} & \frac{\partial^2 \mathcal{E}}{\partial n_1 \partial n_2} \\ \frac{\partial^2 \mathcal{E}}{\partial n_2 \partial n_1} & \frac{\partial^2 \mathcal{E}}{\partial n_2^2} \end{pmatrix} = \begin{pmatrix} g_{11} & g_{12} \\ g_{12} & g_{22} \end{pmatrix}, \tag{19}$$

which, considering that $g_{ij} > 0$, is positive definite for $g_{11}g_{22} - g_{12}^2 > 0$. If this condition is not satisfied, the mixture is unstable with respect to separation of the two condensates, which breaks our assumption of uniform densities. Thus, the system has two possible ground states. If the interaction constants satisfy the miscibility condition

$$g_{12} < \sqrt{g_{11}g_{22}}, \tag{20}$$

then mixing between the two components is favored, since the interspecies repulsion is weaker than the intraspecies repulsion. In the ground state of a miscible system, the two condensates overlap (with equal densities if $\delta g = 0$ and the external potentials are equal), and their phases are arbitrary constants (as a function of position). When, instead, $g_{12} > \sqrt{g_{11}g_{22}}$, we have an immiscible system, whose ground state exhibits phase separation, with only a small region of overlap at the interface between the two condensates due to the balance between kinetic and interaction energies. In this case, each condensate again has an arbitrary uniform phase, but note that the relative and total phases are not well defined, since φ_j is not defined where $n_j = 0$. We will refer to this feature of the system's phase diagram as the miscibility transition. For convenience, we will call the system a mixture even in the immiscible regime, when this term is somewhat improper. In Fig. 1, we illustrate the miscible and immiscible ground states in a box potential, to give an idea of the background on which the numerical simulations used in our research are run. Two length scales are associated with the interaction energy scales present in the mixture: the density healing length and the spin healing length, defined respectively as

$$\xi_d \equiv \frac{\hbar}{\sqrt{2m(2g+|gs|)n}} \quad \text{and} \quad \xi_s \equiv \frac{\hbar}{\sqrt{2m|g_s|n}}. \tag{21}$$

The dynamical properties of the system differ between the miscible and immiscible phase. We will briefly discuss their elementary excitation spectra: naturally, in an immiscible system, each condensate has its own excitations of the kind described in the previous section. The more interesting case is that of the miscible system, where the overlapping configuration of the two condensates gives rise to two branches of elementary excitations: in the density mode, the condensates oscillate in phase with each other, while in the spin mode they oscillate in counterphase. Both modes are gapless, and can be viewed as the Goldstone modes associated with the spontaneous breaking of the continuous $U(1) \times U(1)$ symmetry. They can also be understood as hybridizations of the elementary excitations of the two condensates. These modes can be studied by linearizing the coupled GPEs for small-amplitude perturbations over their uniform ground state, and their dispersion relations are (see [1]):

$$\hbar\omega_{d,s}(k) = \sqrt{\frac{\hbar^2k^2}{2m}\left(\frac{\hbar^2k^2}{2m} + 2mc_{d,s}^2\right)} \tag{22}$$

where

$$c_{d,s}^2 = \frac{g_{11}n_1 + g_{22}n_2 \pm \sqrt{(g_{11}n_1 - g_{22}n_2)^2 + 4n_1n_2g_{12}^2}}{2m} \tag{23}$$

are the density and spin speeds of sound. When $g_{11} = g_{22} = g$ and $n_1 = n_2 = n/2$, this simplifies to

$$\begin{cases} c_d^2 = \dfrac{(2g - |g_s|)n}{2m} & \text{(24a)} \\ c_s^2 = \dfrac{|g_s|n}{2m}, & \text{(24b)} \end{cases}$$

highlighting the role of g_s in the properties of the mixture's elementary excitations. The spectra in this special case are illustrated in Fig. 2. From this expression it is also easy to see that if all interaction constants are equal, and at equal densities, then $g_s = 0$ and the spin mode's spectrum is quadratic, becoming a branch of massive excitations.

Both the ground state and the excitation spectrum of a mixture are altered considerably by the presence of coherent coupling $\Omega = |\Omega|e^{i\varphi_\Omega}$ (see [5]). As already mentioned, the definite phase of the Rabi field reduces the symmetry of the system, fixing the value of the relative phase in a stationary state and breaking the individual conservation of particle number for the two condensates. Now only the total particle number $N_{\text{tot}} = N_1 + N_2$ is conserved and, correspondingly, the system has a single chemical potential

$$\mu = \frac{\partial E}{\partial N_{\text{tot}}}. \tag{25}$$

We return to the question of the ground state of a homogeneous mixture by examining the energy density, which in terms of the variables n_j and φ_j reads

$$\mathcal{E} = \sum_{j=1,2}\left[\frac{\hbar^2}{2m}\left(\frac{1}{2n_j}(\frac{\partial n_j}{\partial\zeta})^2 + n_j(\frac{\partial\varphi_j}{\partial\zeta})^2\right) + \sum_{k=1,2}\frac{g_{jk}}{2}n_jn_k\right] + 2\hbar\sqrt{n_1n_2}|\Omega|\cos\big(\varphi+\varphi_\Omega\big),$$

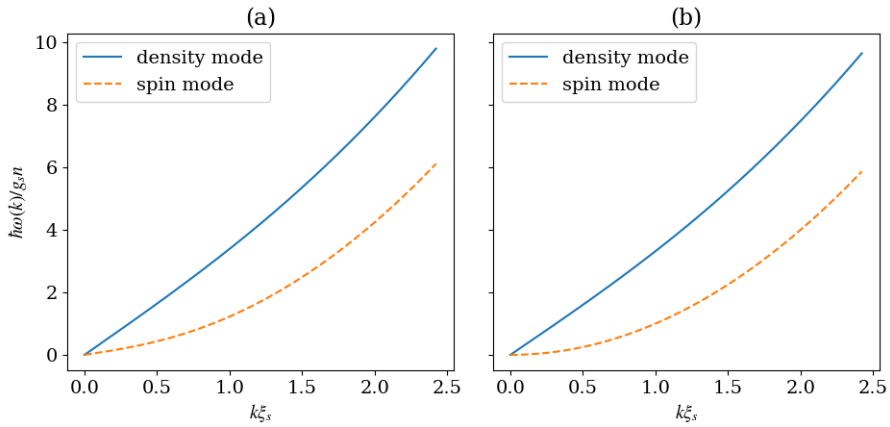

Figure 2: Spectra of the elementary excitations of a miscible condensate mixture with $g_{11} = g_{22} = g$ and $n_1 = n_2$. ξ_s is the spin healing length. Both the density and the spin dispersion relations are linear for $k \to 0$, meaning the long-wavelength excitations have a well-defined speed of sound, and become quadratic for $k \to \infty$. The qualitative features of the spectra are the same at general values of interaction constants and densities. In panel (a), we use $g_s < 0$ (miscible regime), while panel (b) shows the spectra at the critical point $g_s = 0$, displaying the softening of the spin mode.

from which it is clear that the state of minimum energy must have uniform densities and uniform phases such that $\cos(\varphi + \varphi_\Omega) = -1 \implies \varphi + \varphi_\Omega = (2k+1)\pi$. We emphasize, however, that, unlike in the case $\Omega = 0$, a generic stationary state with uniform density may have non-uniform relative phase as long as the total phase is uniform. For the ground state, we are thus left with

$$\mathcal{E} = \frac{g_{11}}{2} n_1^2 + \frac{g_{22}}{2} n_2^2 + g_{12} n_1 n_2 - 2\hbar|\Omega|\sqrt{n_1 n_2},$$

and look for its minimum with respect to n_1 and n_2. We assume $g_{11} = g_{22} = g$, which will allow us to find the key properties of the ground state more easily. The extrema of $\mathcal{E}$ must satisfy $\partial\mathcal{E}/\partial n_1 = \partial\mathcal{E}/\partial n_2$, yielding the condition

$$\left(g - g_{12} + \frac{\hbar|\Omega|}{\sqrt{n_1 n_2}} \right)(n_1 - n_2) = 0,$$

which has two solutions as a function of the density difference $n_1 - n_2$, each of which is the minimum of $\mathcal{E}$ in a different range of parameters. The ground state thus has

$$\begin{cases} n_1 - n_2 = 0 & \text{for } g_s < \frac{2\hbar|\Omega|}{n} \quad \text{(26a)} \\ n_1 - n_2 = \pm n\sqrt{1 - \left(\frac{2\hbar|\Omega|}{g_s n}\right)^2} & \text{for } g_s > \frac{2\hbar|\Omega|}{n}. \quad \text{(26b)} \end{cases}$$

Like in the case of $\Omega = 0$, the coherently coupled mixture has two phases. However, the distinction is now between a polarized phase and an unpolarized phase, and the phase transition occurs at a higher value

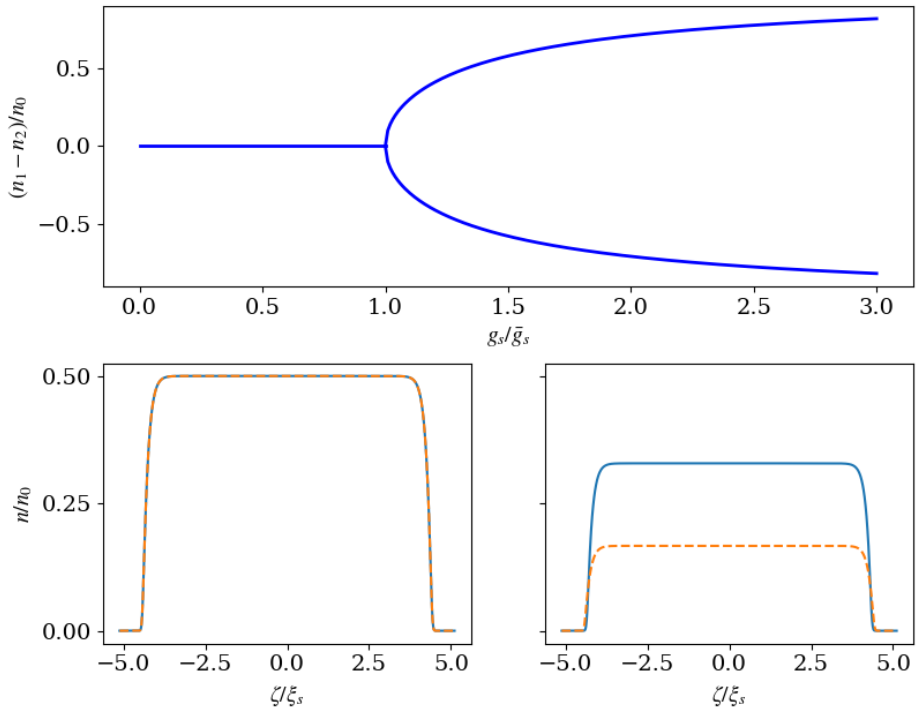

Figure 3: Top: ground state polarization of a coherently coupled mixture as a function of the interspecies repulsion g_{12} at $\delta g = 0$. The system exhibits a phase transition from a paramagnetic mixture below the critical value $\bar{g}_s \equiv 2\hbar|\Omega|/n$ to a ferromagnetic mixture whose ground state can take positive or negative polarization above it. The polarization approaches ± 1 as g_s grows. Bottom row: examples of numerical ground states of a coherently coupled mixture in a box potential in the paramagnetic (left) and ferromagnetic (right) regimes.

of interspecies repulsion than before, since the miscibility condition for a mean-field coupled mixture with $\delta g = 0$ reads $g_s < 0$. The two phases are referred to as paramagnetic and ferromagnetic, respectively. If, for positive g_s, we take g_s to vary at constant Ω, we can mark this magnetic transition with the critical parameter $\bar{g}_s \equiv 2\hbar|\Omega|n$, while if we vary Ω at constant g_s we can define the critical frequency $\Omega_c \equiv g_s n/2\hbar$. The dependence of the ground state polarization is illustrated in Fig. 3. If the mixture is asymmetrical, i.e. $\delta g \neq 0$, the ground state has a non-zero polarization even in the paramagnetic phase, and the degeneracy between positive and negative polarization is lifted, since it is favorable for the component with the higher intraspecies repulsion to have the lower density ([5]).

The reduction in symmetry caused by the presence of Rabi coupling also affects the excitation spectrum of the mixture, leaving only one gapless branch of excitations - the density branch - corresponding to the Goldstone mode associated with the remaining $U(1)$ symmetry. The spin mode instead acquires a gap proportional to $|\Omega|$, and at the critical point $g_s = 2\hbar|\Omega|/n$, the gap closes and the mode becomes linear at small k, in contrast to the quadratic behavior seen for $\Omega = 0$. The spectra in the paramagnetic phase with $\delta g = 0$ are:

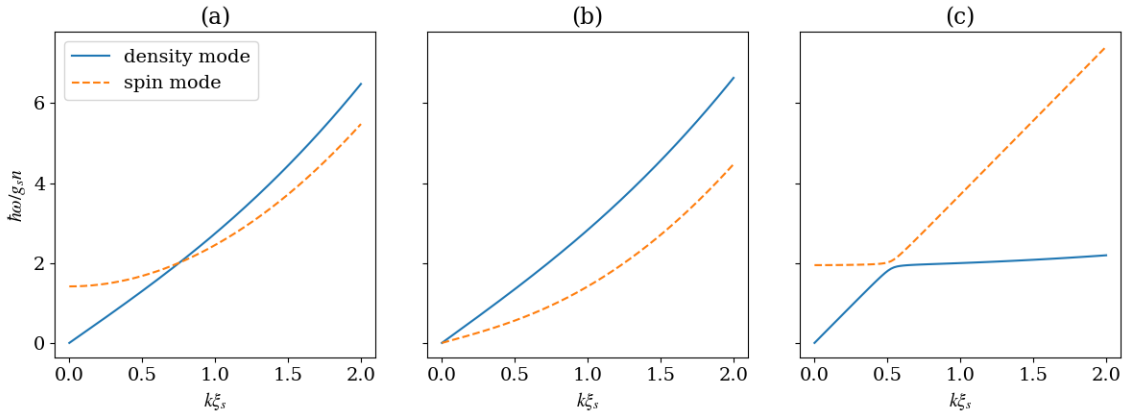

Figure 4: Elementary excitation spectra of the coherently coupled mixture with $\delta g = 0$ in the paramagnetic phase (panel a), at the critical point $g_s = \bar{g}_s$ (panel b), and in the ferromagnetic phase (panel c).

$$\begin{cases} \hbar\omega_d(k) = \sqrt{\dfrac{\hbar^2k^2}{2m}\left(\dfrac{\hbar^2k^2}{2m} + (2g + g_s)n\right)} & \text{(27a)} \\ \hbar\omega_s(k) = \sqrt{\dfrac{\hbar^2k^2}{2m}\left(\dfrac{\hbar^2k^2}{2m} - g_s n + 4\hbar|\Omega|\right)} + 2\hbar|\Omega|(-g_s n + 2\hbar|\Omega|). & \text{(27b)} \end{cases}$$

The density excitation spectrum is unchanged with respect to the $\Omega = 0$ case, and the spin and density branches cross at the momentum $k_0 = \sqrt{\frac{2m|\Omega|}{\hbar}\left(\frac{g}{g+g_s-\bar{g}_s} - 1\right)}$, a feature that can be seen in Fig. 4. The spectra of both the ferromagnetic mixture and the paramagnetic mixture with $\delta g \neq 0$, which are qualitatively similar in that their ground states are both polarized, also exhibit a gapped spin mode and a gapless phononic density mode, but the crossing is avoided. Analytical expressions for these cases are given in reference [6].

Coherent coupling gives rise to internal Bose-Josephson physics [7, 8], in which the dynamics of the population imbalance are coupled to those of the relative phase between the two condensates. In addition to its inherent interest, this aspect of the mixture's dynamics will be relevant in chapter 5, so we give it a brief treatment here, following reference [9]. We restrict our attention to uniform systems and dynamics in which the total density and total current are constants (see also section 2.3), leaving the relative density $Z \equiv (n_1 - n_2)/n$ (which for uniform densities is equal to the relative population imbalance $(N_1 - N_2)/N_{\text{tot}}$) and relative phase φ as dynamical variables. This pair is often visualized as parametrizing a Bloch sphere, whose points have the height Z and the polar angle φ. Restating the coupled GPEs in terms of these variables, we obtain the Bose-Josephson equations

$$\begin{cases} \dot{Z} = 2\Omega\sqrt{1 - Z^2}\sin\varphi & \text{(28a)} \\ \dot{\varphi} = 2\Omega Z\left(\Lambda + \dfrac{\cos\varphi}{\sqrt{1 - Z^2}}\right), & \text{(28b)} \end{cases}$$

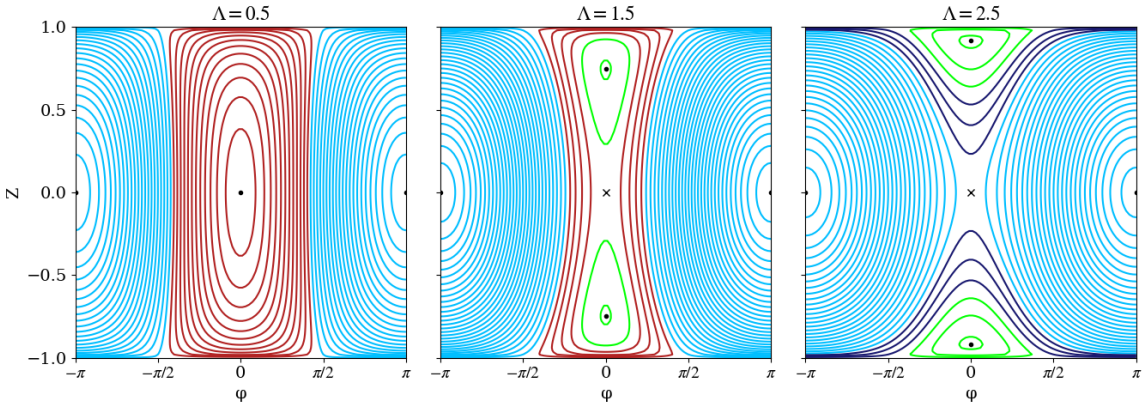

Figure 5: Trajectories admitted by the Bose-Josephson equations for different values of Λ, in the Rabi regime (left panel), the Josephson or self-trapping regime (middle panel), and deep enough into the Josephson regime to allow running-phase modes (right panel). New fixed points at $Z = \pm\sqrt{1-\Lambda^{-2}}$ appear for $|\Lambda| > 1$. The plots show the different kinds of trajectories of the system: plasma oscillations in cyan, π oscillations in red, Josephson oscillations in green, and running-phase modes in indigo. Which dynamics will be realized depends on where in the phase space the initial state lies, as well as on Λ.

where $\Lambda \equiv g_s n/2\hbar\Omega$. In a stationary state, $\dot{\varphi} = \dot{Z} = 0$, the relative phase is either $\varphi_0 = 0$ or $\varphi_0 = \pi$, while the relative density is either $Z_0 = 0$ or, if $|\Lambda| > 1$, may take the polarized values $Z_0 = \pm\sqrt{1-\Lambda^{-2}}$, in accordance with the fact that the mixture is paramagnetic for $|\Lambda| < 1$ and ferromagnetic for $|\Lambda| > 1$. The points of stable equilibrium in the phase space are those with $\varphi = \pi$ (for our chosen sign of Ω in the GPEs); those with $\varphi = 0$ are maxima of the energy. All these stationary states behave as fixed points around which the system orbits during its constant-energy dynamics, which admit several regimes distinguished by the value of Λ and by the initial state (see Fig. 5).

For $|\Lambda| < 1$, the so-called Rabi regime, the system orbits around the fixed point $(Z, \varphi) = (0, 0)$ or $(0, \pi)$, so that the relative density and phase both oscillate with amplitudes depending on the initial state, and the time average of the relative density vanishes. This is easily interpreted as the population-switching dynamics of the coherent coupling (or precession about an effective transverse field) dominating in the paramagnetic phase. These evolutions are commonly known as plasma oscillations (when the system orbits its ground state) and π oscillations (when the system orbits its energy maximum, which differs from the ground state by a π relative phase rotation). When $|\Lambda| > 1$, the Josephson regime is entered. The fixed point $(0, 0)$ becomes unstable and bifurcates into the two stable fixed points $\left(\pm\sqrt{1-\Lambda^{-2}}, 0\right)$ (the degenerate ground states of the ferromagnetic mixture), and a separatrix appears, distinguishing two types of trajectories. In the first type, the system orbits one of the fixed points at finite Z, and the relative density never changes sign as both it and the relative phase oscillate: the system exhibits self-trapping. However, if the initial state is far enough from the finite-Z fixed points to cross the separatrix, the system will orbit the fixed point $(0, \pi)$, describing plasma oscillations. At $|\Lambda| > 2$, a third regime emerges in which the separatrix encloses the poles of the Bloch sphere, giving rise to self-trapped trajectories, orbiting one of the finite-Z fixed points, in which φ increases or decreases monotonically rather than oscillating: these are called running-phase modes. Again, plasma oscillations are also present. The oscillations of the uniform system are characterized, in the

small-amplitude limit, by the frequency

$$\omega_J^2 = 4\Omega^2 \left(-\Lambda \sqrt{1 - Z_0^2} \cos \varphi_0 + \frac{1}{1 - Z_0^2} \right). \tag{29}$$

Which has several interesting limits as a function of Ω at fixed g_s and n_0. For $\Omega \to 0$, ω_J tends to the finite value $2\Omega_c$, which corresponds to the chemical potential difference $\mu_2 - \mu_1 = g_s n$ of an immiscible system in a region where $n_2 = 0$: in this limit, the amplitude of Z oscillations vanishes and we recover the phase rotation of a stationary non-coherently-coupled system. For $\Omega \to +\infty$, ω_J is asymptotic to Ω, since the coherent coupling dominates completely. The frequency also has a cusp, vanishing with infinite derivative as it approaches Ω_c from either side. Thus the period of oscillations diverges as the system approaches the transition between Rabi and Josephson regimes. This phenomenon is known as critical slowing down.

2.3 Mapping to ferromagnetic system

In this section, we show that the coupled Gross-Pitaevskii equations (Eq. 13) admit a limit in parameter space - namely, the Manakov limit $|g_s| \ll g$, $|\delta g| \ll g$ (so named for the work on the coupled GPEs with all interaction constants equal in [10]) - in which they become equivalent to the dissipationless uniaxial Landau-Lifshitz equation, which is a well-established tool in the macroscopic theory of the dynamics of the magnetization vector field in classical ferromagnets [11, 12]. We state it here for reference:

$$\frac{\partial \vec{M}}{\partial t} = \frac{2\mu_0}{\hbar} (\vec{H}_{\text{eff}} + \vec{H}_{\text{ext}}) \wedge \vec{M} \tag{30}$$

where $\vec{M}(\zeta, t)$ is the magnetization vector field, μ_0 is the Bohr magneton, $\vec{H}_{\text{ext}}$ is an external magnetic field, and $\vec{H}_{\text{eff}} = \tilde{\alpha} \partial_\zeta^2 \vec{M} - \tilde{\beta} M_z$ is an effective magnetic field with the parameters $\tilde{\alpha}$ and $\tilde{\beta}$ determined by the properties of the material. Physically, the effective field is related to the structure of the crystal lattice that makes up the ferromagnet, and from the perspective of a microscopic spin model its first term arises from the exchange interaction between neighboring spins and the second one from the anisotropy of the lattice couplings. The description of ferromagnetic materials may require more general forms of the Landau-Lifshitz equation, which admits biaxial anisotropy (corresponding to the addition of a term proportional to M_x to the effective field) and the inclusion of a dissipation term, but these are not relevant to our discussion and cannot be mapped to Eq. 13. Returning to the dissipationless uniaxial equation (which for brevity we will refer to here as the LLE), three cases can be distinguished according to the sign of the anisotropy constant β.

The isotropic ferromagnet, for which $\beta = 0$, will not concern us. For $\beta \neq 0$, the system has an anisotropy axis, which for our definition of $\vec{H}_{\text{eff}}$ coincides with the z axis. For $\beta > 0$, we have an easy-axis ferromagnet, in whose ground state, in the absence of an external field, the magnetization vector is uniform and parallel to the anisotropy axis (which is then also called the easy axis). For $\beta < 0$, we have an easy-plane ferromagnet, where the ground state magnetization, again for $\vec{H}_{\text{ext}} = 0$, is uniform but oriented in an arbitrary direction in the plane perpendicular to the anisotropy axis (the easy plane). A few further features of easy-axis and easy-plane ferromagnets will be discussed below.

The equivalence between Eqs. 13 and 30 takes the form of a straightforward and formally exact mapping between the two, with direct correspondences between the quantities that appear in each, and it allows analytical and numerical results established in one context to be "translated" into the other and be expected to hold within a certain parameter regime. On a theoretical level, it gives us grounds for discussing the physics of BEC mixtures in terms of "magnetic" phenomena. On a technical one, it allows research into

BEC mixtures to take advantage of the rich literature on ferromagnetism for results that may be less easily arrived at through direct use of the GPE. While this may be interesting in its own right, what makes it more than a mere exercise is the fact that the coupled GPEs are mathematically more complex than the LLE - this can be immediately seen, for example, from the fact that the two complex order parameters of the former give four independent dynamical variables, while the three-dimensional vector of fixed length of the latter only gives two. This makes the coupled GPEs less tractable analytically, and corresponds to the fact that the physics of a condensate mixture is in general richer than that of a ferromagnet described by Eq. 30. Thus, a possible approach to exploring the wider phenomenology of a condensate mixture is to use the conceptual and technical simplifications in the LLE to establish results that can serve as a starting point from which to probe deviations in behavior in broader regions of the parameter space of the coupled GPEs. Conversely, the mapping can also illuminate the physics of ferromagnets in cases where certain mechanisms are more readily grasped in the condensate picture. Furthermore, the great experimental advantages available in the control and measurement of atomic condensates can make it possible to directly observe phenomena that it is unfeasible to see in solid-state ferromagnets. The results presented in chapter 3 exemplify these factors.

We begin to explore the mapping in detail by restating the coupled GPEs, rather than in terms of the complex order parameter vector $\Psi = \left(\psi_1,\ \psi_2\right)^T$, in terms of a spin vector which emerges from the condensate mixture's density matrix (see [13])

$$\hat{A} = \Psi^* \otimes \Psi = \begin{pmatrix} |\psi_1|^2 & \psi_1^*\psi_2 \\ \psi_2^*\psi_1 & |\psi_2|^2 \end{pmatrix}.$$

Like any two-by-two Hermitian matrix, this can be decomposed onto the identity matrix and the three Pauli matrices $\vec{\sigma} = (\sigma_1, \sigma_2, \sigma_3)^T$, leading to a new set of variables describing the system: the total density $n = \mathrm{Tr}(\hat{A}) = |\psi_1|^2 + |\psi_2|^2$ and the spin vector

$$\vec{s} = \mathrm{Tr}(\vec{\sigma}\hat{A}) = \begin{pmatrix} \psi_1^*\psi_2 + \psi_2^*\psi_1 \\ i(\psi_1^*\psi_2 - \psi_2^*\psi_1) \\ |\psi_1|^2 - |\psi_2|^2 \end{pmatrix}. \tag{31}$$

Note that $|\vec{s}| = n$. Substitution into Eq. 13 gives the following system of equations for the evolution of the density, the spin vector, and the velocity field $v = j/n = (n_1 v_1 + n_2 v_2)/n$:

$$\begin{cases} \dfrac{\partial n}{\partial t} + \dfrac{\partial}{\partial \zeta}(nv) = 0 & \text{(32a)} \\ m\dfrac{\partial v}{\partial t} + \dfrac{\partial}{\partial \zeta}\left(\dfrac{mv^2}{2} + \dfrac{g_s s_z^2}{2n} + \hbar\Omega\dfrac{s_x s_z}{s_x^2 + s_y^2} + \mu + V_{\mathrm{ext},1} + V_{\mathrm{ext},2} - \dfrac{\hbar^2}{2m\sqrt{n}}\dfrac{\partial^2\sqrt{n}}{\partial\zeta^2} + \dfrac{\hbar^2}{8mn^2}\left|\dfrac{\partial\vec{s}}{\partial\zeta}\right|^2 \right) = 0 & \text{(32b)} \\ \dfrac{\partial\vec{s}}{\partial t} + \dfrac{\partial\vec{j}_s}{\partial\zeta} = \vec{H}(\vec{s}) \wedge \vec{s}, & \text{(32c)} \end{cases}$$

with the nonlinear effective magnetic field

$$\vec{H}(\vec{s}) = 2\Omega\vec{e}_x + \left(\frac{g_s}{\hbar}s_z - \frac{\delta g}{2\hbar}n + \frac{V_1 - V_2}{\hbar}\right)\vec{e}_z,$$

and where we have introduced the spin current density

$$\vec{j}_s = v\vec{s} + \frac{\hbar}{2mn}\frac{\partial\vec{s}}{\partial\zeta} \wedge \vec{s}.$$

The first and second terms in the definition of $\vec{j}_s$ are respectively known as the spin advection and the quantum torque. We have assumed, without loss of generality, that Ω is real and positive, and will continue to work under this assumption. If $\Omega = |\Omega|e^{i\varphi_\Omega}$ has a non-zero phase, then it enters the above equation as a field oriented at an angle φ_Ω from the x axis in the xy plane, but since it is the only field involved which breaks rotational symmetry about the z axis, it can always be aligned along $\vec{e}_x$ through a change in coordinates.

The first equation in this system can be viewed straightforwardly as a continuity equation expressing the conservation of total particle number, with j being the Noether current associated to the spontaneously broken global $U(1)$ symmetry. The second equation takes the form of an Euler equation relating the evolution of the velocity field to the various contributions to the energy of the system. The third equation is of similar form to the first, but is made more complicated by the source term which incorporates precession of the spin vector about external fields as well as a nonlinear field proportional to g_s. It can also be read as a continuity equation for the spin current, with its conserved charge being the components of the total spin, for $g_s = \delta g = 0$ and in the absence of external fields, in which case the conservation law is associated with the system's $SU(2)$ symmetry. For arbitrary values of the interaction constants, this symmetry is in general explicitly broken, and only the z component of the total spin is conserved - this is a manifestation of the reduction of the $SU(2)$ symmetry to a $U(1)\times U(1)$ symmetry and the corresponding conservation of both species' particle number, or equivalently of both the total population and the relative population $\int s_z \, \mathrm{d}\zeta = N_1 - N_2$. A non-zero value of Ω breaks this conservation law as well: physically, this is due to coherent coupling making it possible for the bosons in the condensates to switch species. In the magnetic picture, it appears as the effect of a transverse field contributing precession around the x axis to the dynamics. In this formulation, the Bose-Josephson equations discussed in section 2.2 are obtained from Eq. 32c for $\delta g = 0$ and in the uniform limit where the ζ derivative of the spin current can be neglected, so that they take the form $\partial_t \vec{s} = (2\Omega, 0, g_s s_z/\hbar) \wedge \vec{s}$.

The similarity to the LLE of the coupled GPEs recast in this form is apparent. Indeed, we will see that the crucial effect of taking the Manakov limit is that the total density decouples from the spin dynamics and becomes a constant n_0. It follows that the equations in system 32 decouple, with the first equation becoming a statement of the divergencelessness of the current j, which in one spatial dimension implies it is a constant, and from its definition $j = nv$ it follows that the total velocity is also a constant, i.e. if there are no variations in density, there cannot be any variations in flow velocity without violating particle number conservation. This means that there is a reference frame where j and v are zero. The second equation accordingly becomes trivial and the system is entirely described by the equation of motion of the spin, Eq. 32c, which in turn is simplified. In the reference frame where $j = 0$ the spin advection term in the spin current vanishes, and the derivative of the spin current simplifies greatly: $\partial_\zeta \vec{j}_s = (\hbar/2mn_0)(\partial_\zeta^2 \vec{s} \wedge \vec{s} + \partial_\zeta \vec{s} \wedge \partial_\zeta \vec{s}) = (\hbar/2mn_0)\partial_\zeta^2 \vec{s} \wedge \vec{s}$. This term is directly analogous to the field $\vec{H}_{\text{eff}}$ in Eq. 30, so that Eq. 32c, after appropriate rescaling of variables, takes the form of a Landau-Lifshitz equation, which is thus equivalent to the coupled GPEs in the Manakov limit.

To see explicitly that the total density reduces to a constant, we parametrize the spin vector using spherical coordinates, which are useful quantities conceptually, having clear meanings both in the context of the condensate mixture and in that of the ferromagnet. We thus define

$$\begin{pmatrix} \psi_1 \\ \psi_2 \end{pmatrix} = \sqrt{n} e^{i\Phi/2} \begin{pmatrix} \cos\frac{\theta}{2} e^{-i\varphi/2} \\ \sin\frac{\theta}{2} e^{i\varphi/2} \end{pmatrix},$$

which is equivalent to the parametrization $\vec{s} = n\,(\sin\theta\cos\varphi,\ \sin\theta\sin\varphi,\ \cos\theta)^T$ along with $j = (n\hbar/2m)(\partial_\zeta\Phi - \cos\theta\partial_\zeta\varphi)$. In terms of the condensate mixture, we are working with the total density n, relative density $\cos\theta$, total phase Φ, and relative phase φ. We will also refer to $\cos\theta$ as the z-magnetization. Substitution of these definitions into Eq. 13 yields the time evolution equations

$$
\begin{cases}
\hbar\dfrac{\partial n}{\partial t} = -\dfrac{\hbar^2}{2m}\dfrac{\partial}{\partial\zeta}\left(n\dfrac{\partial\Phi}{\partial\zeta} - n\cos\theta\dfrac{\partial\varphi}{\partial\zeta}\right) & \text{(33a)}\\
\hbar\dfrac{\partial\theta}{\partial t} = -\dfrac{\hbar^2}{2mn}\dfrac{\partial}{\partial\zeta}\left(n\sin\theta\dfrac{\partial\varphi}{\partial\zeta}\right) - \dfrac{\hbar^2}{2m}\dfrac{\partial\Phi}{\partial\zeta}\dfrac{\partial\theta}{\partial\zeta} - 2\hbar\Omega\sin\varphi & \text{(33b)}\\
\hbar\dfrac{\partial\Phi}{\partial t} = -\dfrac{\hbar^2}{2m}\left[\dfrac{1}{2n^2}(\dfrac{\partial n}{\partial\zeta})^2 - \dfrac{1}{n}\dfrac{\partial^2 n}{\partial\zeta^2} - \dfrac{\cot\theta}{n}\dfrac{\partial}{\partial\zeta}\left(n\dfrac{\partial\theta}{\partial\zeta}\right) + \dfrac{1}{2}\left((\dfrac{\partial\Phi}{\partial\zeta})^2 + (\dfrac{\partial\varphi}{\partial\zeta})^2 + (\dfrac{\partial\theta}{\partial\zeta})^2\right)\right] & \\
\qquad - (2g+g_s)n - \dfrac{\delta g}{2}n\cos\theta - 2\hbar\Omega\dfrac{\cos\varphi}{\sin\theta} - (V_{\text{ext},1}+V_{\text{ext},2}) & \text{(33c)}\\
\hbar\dfrac{\partial\varphi}{\partial t} = \dfrac{\hbar^2}{2mn\sin\theta}\dfrac{\partial}{\partial\zeta}\left(n\dfrac{\partial\theta}{\partial\zeta}\right) - \dfrac{\hbar^2}{2m}\dfrac{\partial\Phi}{\partial\zeta}\dfrac{\partial\varphi}{\partial\zeta} + g_s n\cos\theta - \dfrac{\delta g}{2}n - 2\hbar\Omega\dfrac{\cos\varphi}{\tan\theta} + V_{\text{ext},1} - V_{\text{ext},2}. & \text{(33d)}
\end{cases}
$$

To show the decoupling of the total density from the rest of the dynamics, we consider its behavior with respect to a stationary state, assuming the system is homogeneous, with at most a detuning in the external potentials, i.e. $V_{\text{ext},1} = -V_{\text{ext},1} = \Delta/2$. In this case the stationary state is uniform with some magnetization depending on the detuning Δ, that is, $n(\zeta,t) = n_0$, $\theta(\zeta,t) = \theta_0$. It may have currents, though not if it is the ground state, if $\Omega \neq 0$. The above equation for $\partial_t\Phi$ then reads

$$
\hbar\left.\frac{\partial\Phi}{\partial t}\right|_{\text{st}} = -(2g+g_s)n_0 - \frac{\delta g}{2}n_0\cos\theta_0 - \frac{\hbar^2}{4m}\left[(\left.\frac{\partial\Phi}{\partial\zeta}\right|_{\text{st}})^2 + (\left.\frac{\partial\varphi}{\partial\zeta}\right|_{\text{st}})^2\right] - 2\hbar\Omega\frac{\cos\varphi_{\text{st}}}{\sin\theta_0}
$$

which, for $\Omega = 0$, has the usual meaning of phase rotation in a stationary state. In order to compare the total phase dynamics in a generic scenario to this simpler evolution, we define $\tilde{\Phi} \equiv \Phi - \Phi|_{\text{st}}$. Inserting this into Eq. 33c, we solve for the density fluctuation $(n-n_0)/n_0$. To make the time and length scales involved clear, we write the result in terms of the rescaled variables $\zeta/\xi_s \to \zeta$, $t/\tau_s \to t$, where $\xi_s = \hbar/\sqrt{2m|g_s|n_0}$, $\tau_s = \hbar/|g_s|n_0$. This leads to

$$
\begin{aligned}
\frac{n-n_0}{n_0} =& \frac{|g_s|}{2g+g_s}\left[-\frac{\partial\tilde{\Phi}}{\partial t} - \frac{1}{2n^2}(\frac{\partial n}{\partial\zeta})^2 - \frac{1}{n}\frac{\partial^2 n}{\partial\zeta^2} - \frac{\cot\theta}{n}\frac{\partial}{\partial\zeta}\left(n\frac{\partial\theta}{\partial\zeta}\right) + \frac{1}{2}\left((\frac{\partial\Phi}{\partial\zeta})^2 + (\frac{\partial\varphi}{\partial\zeta})^2 + (\frac{\partial\theta}{\partial\zeta})^2\right)\right]\\
&+ \frac{|g_s|}{2g+g_s}\left[-\frac{1}{2}\left((\left.\frac{\partial\Phi}{\partial\zeta}\right|_{\text{st}})^2 + (\left.\frac{\partial\varphi}{\partial\zeta}\right|_{\text{st}})^2\right) - \frac{2\hbar\Omega}{|g_s|n_0}\left(\frac{\cos\varphi}{\sin\theta} - \frac{\cos\varphi_{\text{st}}}{\sin\theta_0}\right)\right]\\
&+ \frac{\delta g}{2(2g+g_s)}\left[\cos\theta_0 - \frac{n}{n_0}\cos\theta\right].
\end{aligned}
\tag{34}
$$

From this expression it is clear that if we take the Manakov limit $|g_s| \ll g$, $|\delta g| \ll g$, then as long as the dynamical variables involved do not experience large variations on the spin time and length scales[4], we have $|n-n_0| \ll n_0$: the density can be approximated by the constant n_0. This is the essential step in the derivation of the LLE. To complete it, we return to Eqs. 33 and consider the consequences of the constraint $n(\zeta,t) = n_0$. Equation 33a now reads $\partial_\zeta j = 0$: as already mentioned, the total particle current becomes constant. Since

[4]Strictly speaking, we also require that θ is not too close o 0 or π, where the cot θ term diverges. If θ reaches these values at some point, meaning that one of the two species reaches zero density, our argument offers no guarantee that total density fluctuations will remain small. In the scenarios we have explored numerically, this does not pose much of an impediment to our use of the LLE.

$j = nv$, we choose to work in the reference system in which the constant value of j is zero. In this case, the continuity equation further simplifies to the condition

$$\frac{\partial \Phi}{\partial \zeta} - \cos\theta \frac{\partial \varphi}{\partial \zeta} = 0, \tag{35}$$

meaning that the total phase is no longer independent of the other variables but can be solved for once the relative phase (whose dynamics remain coupled to those of the relative density) is known. This fact is not dependent on the choice of reference frame, of course, our convention being merely a convenient choice of the value of the constant in the general expression $\partial_\zeta \Phi - \cos\theta \partial_\zeta \varphi = \text{const}$. Two of the four dynamical variables initially present in our system have been eliminated. The two remaining ones obey the following coupled equations, given in dimensionless form:

$$\begin{cases} \dfrac{\partial \theta}{\partial t} = -2\cos\theta \dfrac{\partial \theta}{\partial \zeta}\dfrac{\partial \varphi}{\partial \zeta} - \sin\theta \dfrac{\partial^2 \varphi}{\partial \zeta^2} - \omega_R \sin\varphi & \text{(36a)} \\ \dfrac{\partial \varphi}{\partial t} = \dfrac{1}{\sin\theta}\dfrac{\partial^2 \theta}{\partial \zeta^2} + \left(\epsilon - (\dfrac{\partial \varphi}{\partial \zeta})^2\right)\cos\theta - \omega_R \dfrac{\cos\varphi}{\tan\theta} + \omega_D, & \text{(36b)} \end{cases}$$

where we have introduced the dimensionless quantities

$$\omega_R \equiv \frac{2\hbar\Omega}{|g_s| n_0}, \quad \omega_D \equiv \frac{\Delta}{|g_s| n_0} - \frac{\delta g}{2|g_s|}, \quad \epsilon \equiv \frac{g_s}{|g_s|}. \tag{37}$$

Note that, at constant density, the difference in intraspecies interaction strengths δg enters the equations in the same way as a detuning in the external potentials, as a constant contribution to $\partial_t \varphi$. In the absence of coherent coupling, this term can be eliminated by introducing the variable $\tilde{\varphi} \equiv \varphi - \omega_D t$: the pair $(\theta, \tilde{\varphi})$ obey Eqs. 36 with $\omega_D = 0$.

It is straightforward to check, by writing out each term in the variables (θ, φ), that this system is equivalent to the Landau-Lifshitz equation for the dimensionless magnetization vector $\vec{M} = -\vec{s}/n_0$

$$\frac{\partial \vec{M}}{\partial t} = (\vec{H}_{\text{eff}} + \vec{H}_{\text{ext}}) \wedge \vec{M} \tag{38}$$

with the fields

$$\vec{H}_{\text{eff}} = \frac{\partial^2 \vec{M}}{\partial \zeta^2} + \epsilon M_z \vec{e}_z, \quad \vec{H}_{\text{ext}} = \omega_R \vec{e}_x + \omega_D \vec{e}_z, \tag{39}$$

showing that in the Manakov limit $|g_s| \ll g$, $|\delta g| \ll g$, the coupled GPEs with uniform external potentials predict evolution at constant and uniform total density and reduce to an LLE where the Rabi coupling appears as a uniform transverse field and the detuning as a uniform longitudinal field (with respect to the anisotropy axis z). Eq. 38 can be obtained directly from Eq. 32c, written in adimensional units, by setting $n = n_0$ and $v = 0$ and defining $\vec{M} = -\vec{s}/n_0$. The correspondences between the condensate picture and the ferromagnet picture are straightforward: the constant density of the former takes the meaning of the constant magnitude of the magnetization vector of the latter; at each position and time, the relative density of the mixture is analogous to the z component of the magnetization vector, and the relative phase to its polar angle. The sign of ϵ in the effective field appearing in the LLE indicates the type of anisotropy: easy-axis for $\epsilon = 1$ and easy-plane for $\epsilon = -1$, and in the limit of small g_s and δg, this distinction corresponds exactly to that between a immiscible and miscible mixture, respectively, since the criterion for miscibility $g_{12} < \sqrt{g_{11} g_{22}}$

becomes equivalent to $g_s < 0$ in this limit. This correspondence is reflected in the physics of the respective systems, as is visible at its most basic level in their ground states. That of a miscible mixture at $\delta g = 0$ and with equal particle numbers in the two components sees them overlap completely, with equal densities and an arbitrary relative phase between them, which translates to the easy-plane ferromagnet's equilibrium state with a uniform magnetization vector lying in the xy plane at an arbitrary angle. Likewise, the ground state in the immiscible case exhibits phase separation between the two components, and maps to the easy-axis ground state where the magnetization vector is everywhere oriented along the z axis. An external differential potential $V_{\text{ext},1} - V_{\text{ext},2}$ acting on the condensate mixture is analogous to an external magnetic field in the z direction acting on the ferromagnet, contributing to precession of the magnetization vector in the xy plane, the precession frequency being analogous to the chemical potential difference. As noted previously, the coherent coupling appears in the LLE picture as a transverse field (taken arbitrarily along $\vec{e}_x$). Its effect on a ferromagnet is analogous to its role in the condensate mixture as described in the previous section: in the ground state, it fixes the polar angle of the magnetization and favors its alignment in the transverse plane even at values of the anisotropy constants which would in its absence give rise to an easy-axis system. According to the relative values of the anisotropy constants and the transverse field, the system has a transition between an unpolarized and a partially polarized phase, with $\cos\theta$ always less than 1 and decreasing to 0 as Ω increases in the latter case.

The system in Eq. 36 can be obtained as the Euler-Lagrange equations for the following Lagrangian density (an approach which was used, for example, in [14]):

$$\mathcal{L} = \frac{\partial\varphi}{\partial t}\cos\theta - \frac{1}{2}\left[(\frac{\partial\theta}{\partial\zeta})^2 + \left((\frac{\partial\varphi}{\partial\zeta})^2 + \epsilon\right)\sin^2\theta\right] - \omega_R\sin\theta\cos\varphi - \omega_D\cos\theta. \tag{40}$$

It is also interesting to recast the system in Hamiltonian form, in which it describes the dynamical variable φ and its conjugate momentum $\pi_\varphi \equiv \partial\mathcal{L}/\partial\dot{\varphi} = \cos\theta$. The Hamiltonian density is

$$\begin{aligned}\mathcal{H} =& \pi_\varphi\frac{\partial\varphi}{\partial t} - \mathcal{L}\\ =& \frac{1}{2}\left[(\frac{\partial\theta}{\partial\zeta})^2 + \left((\frac{\partial\varphi}{\partial\zeta})^2 + \epsilon\right)\sin^2\theta\right] + \omega_R\sin\theta\cos\varphi + \omega_D\cos\theta\\ =& \frac{1}{2}\left[\frac{1}{1-\pi_\varphi^2}(\frac{\partial\pi_\varphi}{\partial\zeta})^2 + \left((\frac{\partial\varphi}{\partial\zeta})^2 + \epsilon\right)(1-\pi_\varphi^2)\right] + \omega_R\sqrt{1-\pi_\varphi^2}\cos\varphi - \omega_D\pi_\varphi.\end{aligned} \tag{41}$$

The Hamilton equations are

$$\frac{\partial\varphi}{\partial t} = \frac{\delta\mathcal{H}}{\delta\pi_\varphi}, \quad \frac{\partial\pi_\varphi}{\partial t} = -\frac{\delta\mathcal{H}}{\delta\varphi}, \tag{42}$$

where $\frac{\delta}{\delta\phi} \equiv \frac{\partial}{\partial\phi} - \frac{\partial}{\partial t}\frac{\partial}{\partial\partial_t\phi} - \frac{\partial}{\partial\zeta}\frac{\partial}{\partial\partial_\zeta\phi}$, yielding

$$\begin{cases}\dfrac{\partial\varphi}{\partial t} = -\dfrac{1}{1-\pi_\varphi^2}\dfrac{\partial^2\pi_\varphi}{\partial\zeta^2} - \dfrac{\pi_\varphi}{(1-\pi_\varphi^2)^2}(\dfrac{\partial\pi_\varphi}{\partial\zeta})^2 - \pi_\varphi\left((\dfrac{\partial\varphi}{\partial\zeta})^2 + \epsilon\right) - \omega_R\dfrac{\pi_\varphi\cos\varphi}{\sqrt{1-\pi_\varphi^2}} + \omega_D\\ \dfrac{\partial\pi_\varphi}{\partial t} = \dfrac{\partial}{\partial\zeta}\left((1-\pi_\varphi^2)\dfrac{\partial\varphi}{\partial\zeta}\right) + \omega_R\sqrt{1-\pi_\varphi^2}\sin\varphi.\end{cases} \tag{43}$$

In this context of these formalisms, some conservation laws of the system are illuminated more clearly. For $\omega_R = 0$, the Lagrangian density is independent of φ, giving rise to a continuity equation for π_φ with the conserved current $(1 - \pi_\varphi^2)\partial_\zeta \varphi$. This is related to the conservation of the total z-magnetization

$$N = \int \pi_{\varphi,0} - \pi_\varphi \, \mathrm{d}\zeta = \int \cos\theta_0 - \cos\theta \, \mathrm{d}\zeta \implies \frac{\mathrm{d}N}{\mathrm{d}t} = 0 \tag{44}$$

in the absence of Rabi coupling, where $\pi_{\varphi,0}$ and θ_0 are the stationary values of the respective quantities (N is strictly speaking the total deviation from the background z-magnetization, since the integral of $\cos\theta$ would diverge in the ground state of the easy-axis system). Another important conserved quantity, associated with the spatial translation invariance of the system, is the canonical momentum, which we give in dimensional units for later convenience. Since in dimensional units $\pi_\varphi = (n_0\hbar/2)\cos\theta$, the canonical momentum is

$$\begin{aligned} P &= \int (\pi_{\varphi,0} - \pi_\varphi)\frac{\partial\varphi}{\partial\zeta}\,\mathrm{d}\zeta = \frac{n_0\hbar}{2}\int (\cos\theta_0 - \cos\theta)\frac{\partial\varphi}{\partial\zeta}\,\mathrm{d}\zeta \\ &= \frac{n_0\hbar}{2}\left(\cos\theta_0 \int \frac{\partial\varphi}{\partial\zeta}\,\mathrm{d}\zeta - \int \frac{\partial\Phi}{\partial\zeta}\,\mathrm{d}\zeta\right) = \frac{n_0\hbar}{2}\left(\cos\theta_0\Delta\varphi - \Delta\Phi\right). \end{aligned} \tag{45}$$

Again, we have accounted for the non-zero background value of π_φ so that the integrals converge. The canonical momentum is thus seen to reduce to a non-local quantity entirely due to the contribution of asymptotic phase changes. Indeed, the local momentum is, by definition, the integral of the total current, which is zero everywhere (up to a constant background value which needs to be subtracted away in a reference frame where it is non-zero). As a consequence, P should be understood in the LLE and the Manakov-limit coupled GPEs as a periodic variable, since it is a sum of phases, which are defined modulo 2π.

2.3.1 Non-homogeneous systems

In the derivation given for the mapping between GPEs and LLE, we assumed the external potentials to be uniform. The inclusion of generic external potentials complicates the reasoning given for the homogeneous system because, while the stationary state is still free of currents, it no longer has uniform densities, i.e. we have $n(\zeta, t) = n_0(\zeta)$ and $\theta(\zeta, t) = \theta_0(\zeta)$. The above argument can be followed in much the same way, but with two major differences: first, the kinetic terms in Eq. 33 (those proportional to $\hbar^2/2m$) no longer vanish even in the stationary state, and we denote them by K for brevity. For convenience, we take here $\Omega = 0$. In the expression for their stationary value $K|_{\mathrm{st}}$, the terms involving derivatives of Φ and φ therefore vanish. The second difference encountered is that since n_0 now varies spatially, the time and length units must be defined using some other value of density, which we take to be an arbitrary value $\bar{n}$. Proceeding as before, we now have

$$\hbar\frac{\partial\Phi}{\partial t}\bigg|_{\mathrm{st}} = -(2g + g_s)n_0 - \frac{\delta g}{2}n_0\cos\theta_0 + K|_{\mathrm{st}}$$

and, in units of $\tau = \hbar/g_s\bar{n}$ and $\xi = \hbar/\sqrt{2mg_s\bar{n}}$,

$$\frac{n - n_0}{n_0} = \frac{\bar{n}}{n_0}\frac{g_s}{2g + g_s}\left[-\frac{\partial\tilde{\Phi}}{\partial t} + K|_{\mathrm{st}} - K\right] + \frac{\delta g}{2(2g + g_s)}\left[\cos\theta_0 - \frac{n}{n_0}\cos\theta\right]. \tag{46}$$

Note that the external potentials do not explicitly enter this expression. The extra terms they give rise to with respect to the uniform case do not change our argument qualitatively: again, if the variations in

the dynamical variables they cause are of order unity on the scale of τ and ξ, the corresponding density fluctuations are suppressed in the Manakov limit. However, the different rescaling in the present case gives rise to the factor $\bar{n}/n_0$ multiplying the first term, so the appropriate limit to take is now $|g_s|\bar{n}/n_0 \ll g$. Since the value of $\bar{n}$ is arbitrary, it is always possible to choose it so that this requirement is equivalent to the Manakov limit - for instance by choosing $\bar{n} = \min(n_0(\zeta))$ - unless the external potentials are such that $n_0(\zeta)$ vanishes at some point, in which case our argument can never guarantee that density fluctuations remain small everywhere and the equivalence between coupled GPEs and LLE may be expected to fail in a region around the point of vanishing density.

As before, we still obtain the condition $\partial_\zeta j = 0$, although the relation giving the total phase now reads $\partial_\zeta \Phi - \cos\theta \partial_\zeta \varphi = \text{const.}/n_0$, so that Φ must be solved for in a way that depends on the form of $n_0(\zeta)$. Thus we are again left with equations for the relative density and relative phase, but they now contain extra terms:

$$\begin{cases} \dfrac{\partial\theta}{\partial t} = -2\cos\theta \dfrac{\partial\theta}{\partial\zeta}\dfrac{\partial\varphi}{\partial\zeta} - \sin\theta \dfrac{\partial^2\varphi}{\partial\zeta^2} - \dfrac{\sin\theta}{n}\dfrac{\partial n}{\partial\zeta}\dfrac{\partial\varphi}{\partial\zeta} - \omega_R \sin\varphi & \text{(47a)} \\ \dfrac{\partial\varphi}{\partial t} = \dfrac{1}{\sin\theta}\dfrac{\partial^2\theta}{\partial\zeta^2} + \left(\epsilon - (\dfrac{\partial\varphi}{\partial\zeta})^2\right)\cos\theta + \dfrac{1}{n\sin\theta}\dfrac{\partial n}{\partial\zeta}\dfrac{\partial\theta}{\partial\zeta} - \omega_R \dfrac{\cos\varphi}{\tan\theta} + \omega_D, & \text{(47b)} \end{cases}$$

where now

$$\omega_R \equiv \frac{2\hbar\Omega}{|g_s|\bar{n}}, \quad \omega_D(\zeta) = \frac{V_{\text{ext},1}(\zeta) - V_{\text{ext},2}(\zeta)}{|g_s|\bar{n}} - \frac{\delta g n_0}{2 g_s \bar{n}}, \quad \epsilon = \frac{g_s}{|g_s|}. \tag{48}$$

These extra terms mean that the magnetization vector does not evolve according to a Landau-Lifshitz equation. Thus, the mapping fails for a generic inhomogeneous condensate mixture. Our attempts to apply LLE results to such scenarios, which follow in the text, may be justified by more heuristic arguments. Since we are interested primarily in the dynamics of solitons, which are localized objects, non-uniform background densities and potentials may be considered approximately flat in the neighborhood of the soliton as long as the scale on which they vary are much larger than the typical size of the soliton. Section 4.3 explores the validity of treating a soliton as a quasiparticle in such a scenario. A different situation is one in which external potentials are applied to an initially homogeneous system. In this case, the problem with non-uniform equilibrium densities illustrated in this section does not arise: instead, an analogous argument will treat the effect of the potentials by adding a term $-(V_{\text{ext},1} + V_{\text{ext},2})$ to the first parentheses in Eq. 34, with $n_0(\zeta) = \text{const.}$ Consequently, the mapping is still valid, but an additional criterion for the constancy of the total density throughout the evolution is established: namely, the constraint that the sum of the external potentials varies by a small amount compared to the chemical potential across the system. This case is addressed in more detail in chapter 3.

2.4 Integrability

The one-dimensional Landau-Lifshitz equation belongs to the class of integrable partial differential equations [15], whose initial-value problem can be solved analytically thanks to hidden symmetries present in their mathematical structure. The modern theory of integrability dates to the introduction in 1967 of the inverse scattering transform (IST) method [16], which was first used to solve the Korteweg-de Vries equation, applicable (for instance) to surface waves in water. Subsequent advances ([17, 18, 19, 20]) developed this method into a systematic and well-understood theory. Integrable equations form an important class of physical models: though not very numerous, they possess some degree of universality, being fruitfully applicable to a wide range of physical systems, especially in classical physics and especially in one spatial

dimension. Important examples include the nonlinear Schrödinger equation, which describes slowly varying wave envelopes in weakly nonlinear and dispersive media and is applicable to physical scenarios such as light propagating in nonlinear optical fibers, quasi-one-dimensional Bose-Einstein condensates (being identical to the 1D GPE), and waves in plasmas, and the sine-Gordon equation, which is the simplest field equation with a periodic potential and arises in a variety of situations, including dislocations in a crystal lattice, long Josephson junctions, and in certain limits of the coherently coupled GPEs (see [21]). A two-dimensional example is the Kadomtsev-Petviasvhili equation, which is analogous to the one-dimensional Korteweg-de Vries equation. The mean-field coupled GPEs with all interaction constants equal, meaning $g_s = \delta g = 0$, are known as the Manakov model, which is integrable and was solved in [10]. It is important to distinguish this scenario, exactly at the miscibility transition, from the regime we call the Manakov *limit* ($g_s,\ \delta g \ll g$), which we will focus on. The latter case is infinitesimally close to the transition but retains a notion of miscibiility or immiscibility. Correspondingly, the Manakov-limit coupled GPEs map to the anisotropic LLE, while the Manakov model maps to the isotropic LLE, which we will not make use of.

The equations cited are nonlinear partial differential equations, which are in general not amenable to a comprehensive theory of their behavior. The underlyling reason for the special tractability of integrable systems is related to the fact that they possess an infinite number of non-trivial conservation laws (whose conserved quantities, where applicable, include the familiar integrals of motion such as energy and momentum), a property which is not immediately apparent from the equations themselves, but which restricts the dynamics they admit stringently and systematically enough for them to be treated analytically at a very general level. The IST method takes advantage of this fact: it involves finding an auxiliary eigenvalue equation associated to the original integrable equation, and in so doing defining a formalism in which the infinite family of conservation laws is more readily accessible. Schematically[5], the most basic form of the IST approach (extensions of the original method are required for various equations, including the LLE) involves the following elements. Given an integrable equation for the evolution of a function $u(\zeta, t)$, there exists a so-called Lax pair of linear operators $(\hat{L}, \hat{A})$ whose coefficients depend on u and its derivatives which allow the equation to be rewritten in the form

$$\frac{\partial \hat{L}}{\partial t} + [\hat{L}, \hat{A}] = 0, \tag{49}$$

which translates into the system

$$\begin{cases} \hat{L}\Psi = \lambda\Psi & \text{(50a)} \\ \dfrac{\partial \Psi}{\partial t} = \hat{A}\Psi & \text{(50b)} \end{cases}$$

of auxiliary linear equations. For example, the auxiliary eigenvalue problem for the Korteweg-de Vries equation takes the form of a time-independent Schrödinger equation in which u appears as a potential for Ψ. One proceeds by finding the eigenfunctions, or scattering data, of Eq. 50a, which will in general consist of the discrete spectrum $\{S_n\}$ of bound states and the continuum $S(\lambda)$. The key to the usefulness of this auxiliary formalism is that the scattering data obey, quite generally, the trivial time evolution

$$\begin{cases} \dfrac{\partial S_n(t)}{\partial t} = \omega_n S_n(t) \\ \dfrac{\partial S(\lambda, t)}{\partial t} = i\omega(\lambda) S(\lambda, t). \end{cases} \tag{51}$$

[5]For a thorough discussion see for example [22, 23].

This allows the initial-value problem for the original equation to be solved by using the initial condition $u(\zeta, 0)$ to write the operators $\hat{L}$ and $\hat{A}$ and finding the spectrum of $\hat{L}$ at $t = 0$, then finding the scattering data at an arbitrary time t according to the above trivial evolution, and finally recovering $u(\zeta, t)$ from them (this last step being known as the inverse scattering problem). Within this formalism, the infinite conservation laws for the integrable system can be constructed in terms of the scattering data.

The integrability of the Landau-Lifshitz equation makes the mapping to the Gross-Pitaevskii system, whose physics is in general richer, potentially particularly fruitful under a certain approach: the original work presented in this thesis will be concerned with the behavior of well-understood analytical solutions of the LLE, translated into the coupled GPE language, under conditions which break integrability. Since integrability is a relatively rare property among all possible PDEs, adding arbitrary terms to an integrable equation will usually result in a non-integrable one. However, as long as the original equation is not modified too drastically, one may hope to study deviations from the integrable behavior in a controlled way - indeed, a perturbative theory for quasi-integrable equations exists (see e.g. [24]). In this spirit, we will use analytical and numerical tools to treat the coupled GPEs with the inclusion of several elements which take them beyond the behavior of their integrable limit: finite values of g_s and δg, non-zero external potentials, non-uniform initial total densities, and non-zero coherent coupling. A finite system size, such as that of our simulations, and spatial discretization also break integrability, but we did not delve into the consequences of this, and kept to situations in which finite-size effects are negligible or under control. Physically, the applicability of integrable models is always limited, including in conceptually important ways (for instance, a truly integrable system does not admit thermalization). In our case, an additional source of non-integrability in an experimental scenario is dimensionality: the integrability of our LLE depends on its being defined in one spatial dimension, the validity of which in the description of actual condensate mixtures is based on the approximation of a highly elongated cloud.

2.5 Solitons

Integrable equations are characterized by - and indeed, their study has largely been motivated by - the existence of solitons, a special class of analytical solutions describing nonlinear excitations, including solitary waves (which are localized at a certain position and retain their shape as they move), the kind of excitation we will be interested in. A soliton's analytical expression may depend on one or more parameters. As an example, bions in the easy-axis LLE (see below) are parametrized by two variables, which may be taken to be the soliton velocity and the precession frequency of the magnetization vector. In terms of the IST formalism, solitons correspond to bound states in the spectrum of the scattering problem associated to the given integrable equation, and the parameters that characterize them are given by the (complex) eigenvalues corresponding to those bound states, hence their special role in the study of integrable equations. Indeed, the discrete scattering data of an equation's auxiliary eigenvalue problem always correspond to solitons, while the continuous scattering data always correspond to radiation.

Non-integrable equations may also admit solitary waves as exact solutions [25, 26]. What distinguishes solitons in the strict sense from generic solitary waves is the simplicity of their collisional properties. In the general case, collision between solitary waves may be a complicated event after which the waves may not emerge as well-defined objects, or may emerge with very different properties. Integrable equations, in contrast, admit N-soliton solutions, analytical solutions describing the simultaneous presence of N solitons with different velocities. The essential traits of soliton collisions are the following:

i. No radiation is emitted during a collision between two solitons.

ii. Collisions between two solitons leave them (asymptotically) unchanged. In a two-soliton state, the pair

approach each other from infinite separation at $t = -\infty$, in which limit the state reduces to a sum of two single solitons. They will approach each other, collide, and move away from each other again. As their separation approaches infinity again at $t = +\infty$, they recover their initial properties, i.e. reduce again to single solitons with the same parameters as the incoming ones. The sole effect of their interaction is a so-called phase shift: their positions are changed by a certain amount with respect to the trajectories they would have followed in the respective one-soliton states. The phase shifts are determined analytically by the soliton parameters.

iii. Solitons only experience two-body interactions. This means that the effects on a soliton of any collisions in an N-soliton state are the same as those that would follow from separate collisions with each of the other solitons involved. Thus, in the asymptotic past and the asymptotic future, an N-soliton state decomposes into the sum of N single-soliton states, with the only difference between $t = +\infty$ and $t = -\infty$ being the order of the solitons and that each one will have accrued a phase shift equal to the sum of the phase shifts due to two-way collisions with every soliton it encounters, regardless of the details of the intervening dynamics (during which the state cannot be separated into a sum of N solitons).

The specific forms of solitons across different integrable systems are quite varied, from famous examples such as the kinks and breathers of the sine-Gordon equation or the sech^2 soliton of the Korteweg-de Vries equation to less well-known ones including solitons with discontinuous slopes and ones with oscillatory trajectories. We will report only the functional forms of solitons belonging to the (single-component) GPE and to the LLE, and will not discuss exhaustively all soliton families of these equations, but only the simplest examples, which we used in our work. References [26, 25, 27, 28, 29, 15, 30, 31, 32, 33, 34, 35] discuss the integration of the Landau-Lifshitz and coupled nonlinear Schrödinger equations and their solitons.

2.5.1 Solitons in the GPE

The GPE with repulsive interactions admits a family of solitons parametrized by their velocity, of the form [36]

$$\psi(\zeta - vt) = \sqrt{n_0}\left(i\frac{v}{c} + \sqrt{1 - \frac{v^2}{c^2}}\tanh\left(\frac{\zeta - vt}{\sqrt{2}\xi}\sqrt{1 - \frac{v^2}{c^2}} \right) \right) \tag{52}$$

Such a soliton consists of a dip in density (on a uniform background n_0) with a phase jump across it, as illustrated in Fig. 2.5.1. Its characteristics are determined by its velocity v: the soliton's amplitude is given by its minimum density

$$n(0) = n_0\frac{v^2}{c^2}$$

and the phase variation across it is

$$\Delta\varphi \equiv \varphi(+\infty) - \varphi(-\infty) = -2\arccos\left(\frac{v}{c}\right).$$

For $v = 0$, the minimum density is zero and the phase changes discontinuously by $-\pi$ at its center. This object is known as a dark soliton, whereas a member of this family with finite velocity is sometimes called a gray soliton. The soliton's width is inversely proportional to $\sqrt{1 - v^2/c^2}$, and its total depletion with respect to a uniform condensate is

$$N_D \equiv \int n_0 - n\,\mathrm{d}\zeta = 2\sqrt{2}n_0\xi\sqrt{1 - \frac{v^2}{c^2}}.$$

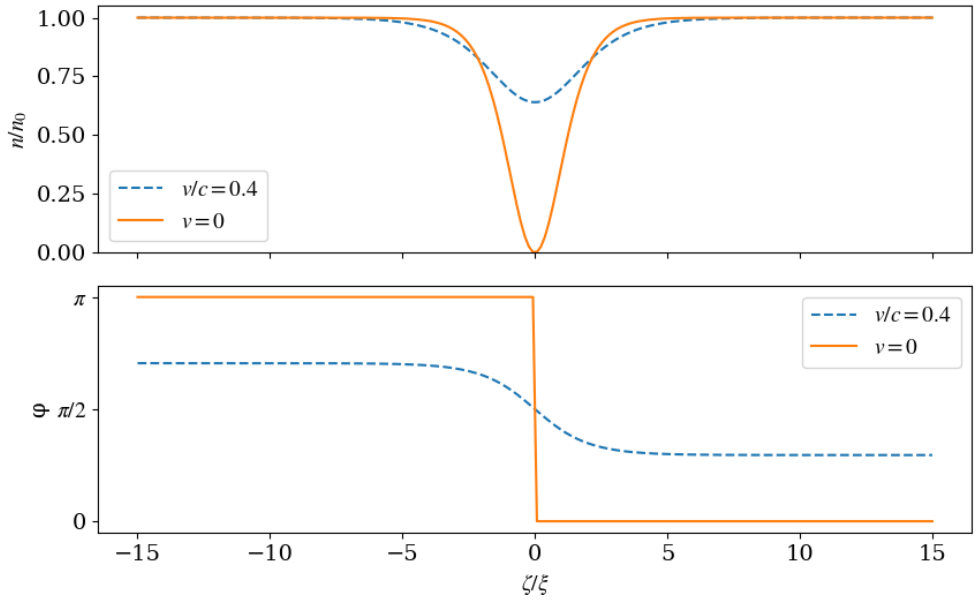

Figure 6: Density and phase of a soliton of the repulsive single-component GPE for two different values of its velocity.

From these expressions it is clear that a soliton is in some sense a nonlocal object, since it can be thought of as connecting two different ground states infinitely far to either side of it, each one uniform but with a different phase. The same will also be true for the solitons of the coupled GPEs. On the other hand, one can treat a soliton as a quasiparticle, a localized object which retains its properties as it evolves and interacts with other structures. These aspects are clarified by calculating the momentum and energy associated with the soliton, which will also provide us with some conceptual tools that will be important later on. From the Lagrangian density in Eq. 7, one calculates the conjugate momenta $\pi = \partial\mathcal{L}/\partial\dot{\psi} = (i\hbar/2)\psi^*$ and $\bar{\pi} = \partial\mathcal{L}/\partial\dot{\psi}^* = (-i\hbar/2)\psi$, or, in terms of the dynamical variables n and φ, $\pi_n = \partial\mathcal{L}/\partial\dot{n} = 0$ and $\pi_\varphi = \partial\mathcal{L}/\partial\dot{\varphi} = \hbar n$ (note that all momentum is associated with φ). Thus the canonical momentum is

$$\begin{aligned} P &= \int (\pi_\varphi - \pi_\varphi^0)\frac{\partial\varphi}{\partial\zeta}\,\mathrm{d}\zeta = \hbar\int (n-n_0)\frac{\partial\varphi}{\partial\zeta}\,\mathrm{d}\zeta \\ &= 2\hbar n_0\left[-\frac{v}{c}\sqrt{1-\frac{v^2}{c^2}} + \arccos\left(\frac{v}{c}\right)\right]. \end{aligned} \tag{53}$$

The soliton's momentum can be split into two contributions: the local momentum $P_{\mathrm{loc}} = \hbar\int n\partial_\zeta\varphi\,\mathrm{d}\zeta = m\int j\,\mathrm{d}\zeta$, which is the momentum carried by the particle current of the order parameter in Eq. 52, and the counterflow momentum $P_{\mathrm{cfl}} = -\hbar n_0\int\partial_\zeta\varphi\,\mathrm{d}\zeta = -\hbar n_0\Delta\varphi$. The latter is a global quantity which accounts for the different asymptotic values of the phase on either side of the soliton. Its presence can be understood by considering a soliton defined on a ring of very large radius. In this case, it is clear that the order parameter given above should be corrected by a counterflow current contributing an asymptotic phase difference $-\Delta\varphi$ in order to ensure that the phase is single-valued. This counterflow induced by the presence of a soliton is an

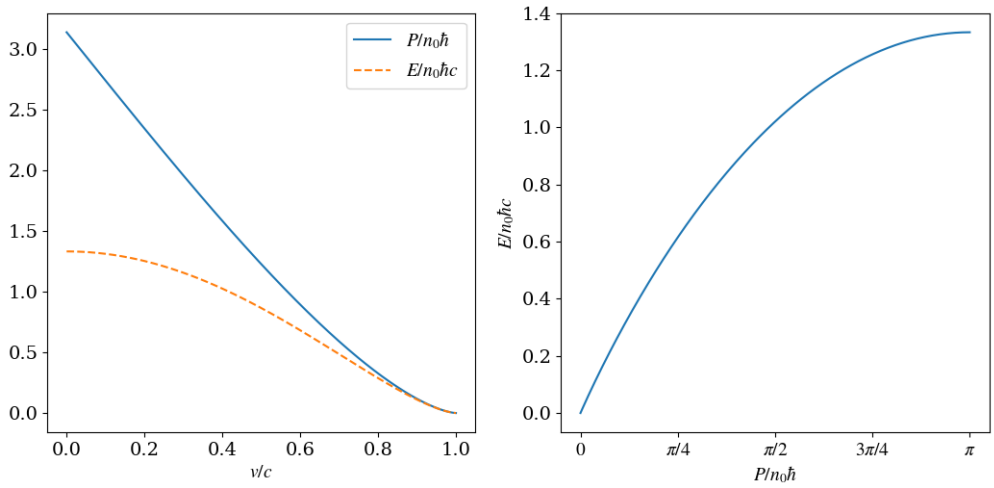

Figure 7: Left: energy and momentum, given in dimensionless units, of a gray soliton of the GPE as a function of its velocity. Right: dispersion relation $E(P)$ of the gray soliton. The curvature of $E(P)$ is always negative.

important feature to take into account, and will be central to the considerations of chapter 3.

The energy of the soliton can be calculated as the difference in the grand canonical energy between the state with the soliton and that without it, resulting in

$$\begin{aligned} E =& \int \frac{\hbar^2}{2m}|\psi|^2 + \frac{g}{2}(n-n_0)^2 \,\mathrm{d}\zeta \\ =& \frac{4}{3}n_0\hbar c\left(1-\frac{v^2}{c^2}\right)^{\frac{3}{2}}. \end{aligned} \tag{54}$$

The energy and momentum are the essential quantities involved when treating the soliton as a quasiparticle, with the dispersion relation $E(P)$ giving its velocity as $\partial E/\partial P$, which one can check is equal to v. The effective mass $m^* \equiv (\partial^2 E/\partial P^2)^{-1}$ of the soliton is always negative, with its low-P limit being $m^*(0) = -4n_0\hbar/c$, which is intuitively consistent with the fact that the soliton consists of a density depletion.

2.5.2 Easy-plane solitons

The solitons of the Landau-Lifshitz equation show both similarities and differences compared to those of the GPE. To begin with, the LLE possesses a considerably richer variety of solitons than the GPE, admitting several families of such objects. We will focus on the simplest of these, which are those where the space and time coordinates enter only through the combination $\zeta - vt$. In the easy-plane case, the simplest family is parametrized by a single parameter, typically taken to be the soliton velocity. The components of the

magnetization vector in the one-soliton solution of this family are given by [15]

$$\begin{cases} \mu_z = \dfrac{\kappa}{\beta}\operatorname{sech}(W(\zeta,t)) \\ \mu_x + i\mu_y = \tanh(W(\zeta,t)) - i\dfrac{\lambda}{\beta}\operatorname{sech}(W(\zeta,t)) \\ W(\zeta,t) = 2\kappa(\zeta + 2\lambda t), \quad \lambda^2 + \kappa^2 = \beta^2 \end{cases} \tag{55}$$

where ζ is in units of the magnetic length $\ell_M = \sqrt{\alpha/\beta}$, t is in units of the inverse of the magnetic frequency $\omega_0 = 2\beta\mu_0 M_0$, and $\vec{\mu} = \vec{M}/M_0$; β is the anisotropy parameter. With this notation, the soliton travels at the constant velocity $v = -2\lambda$. Through the mapping demonstrated in section 2.3, this expression yields the following one in the GPE language (see also [14]):

$$\begin{cases} n_{1,2} = \dfrac{n_0}{2}\left[1 \pm \sqrt{1-u^2}\operatorname{sech}\left(\sqrt{1-u^2}\dfrac{\zeta - uc_s t}{\xi_s}\right)\right] \\ \cot(\varphi) = -\dfrac{1}{u}\sinh\left(\sqrt{1-u^2}\dfrac{\zeta - uc_s t}{\xi_s}\right) \\ \tan(\Phi + C) = -\dfrac{\sqrt{1-u^2}}{u}\tanh\left(\sqrt{1-u^2}\dfrac{\zeta - uc_s t}{\xi_s}\right), \end{cases} \tag{56}$$

where $u = v/c_s$ is the soliton velocity in units of the spin speed of sound c_s and ξ_s is the spin healing length. We will refer to this soliton family as magnetic solitons. The integration constant C may be chosen to satisfy the boundary condition $\Phi(-\infty) = 0$. The condensate densities and phases in such a soliton are illustrated in Fig. 8.

Magnetic solitons have several similarities to the solitons of the single-component GPE, although they entail both a depletion in one component and a concomitant bump in the other such that the total density remains constant: their amplitudes and inverse widths are proportional to $\sqrt{1-u^2}$, with the depleted component reaching zero density at the center of the soliton for $u = 0$, and the phase of each component varies between two different asymptotic values. However, while the change in total phase depends on u, the relative phase always goes from $\varphi(-\infty) = 0$ to $\varphi(+\infty) = \pi$. The population difference between the two components, meaning the number of particles in the soliton, is also independent of u: $N_1 - N_2 = \int n_1 - n_2 \,\mathrm{d}\zeta = \pi n_0 \xi_s$ (in the LLE language, the total z-magnetization is $\int \cos\theta \,\mathrm{d}\zeta = \pi/4\beta$). The energy and momentum of these solitons (illustrated in Fig. 9) is

$$\begin{cases} P = n_0\hbar\dfrac{u}{|u|}\arccos(|u|) & \text{(57a)} \\ E = n_0\hbar c_s\sqrt{1-u^2} = n_0\hbar c_s \sin\left(\dfrac{|P|}{n_0\hbar}\right). & \text{(57b)} \end{cases}$$

The momentum can be calculated explicitly using the given expressions for $\cos\theta$ and φ or by taking advantage of Eq. 45 which relates it to the asymptotic phase changes. In the present case, $\cos\theta_0 = 0$ and

$$\Delta\Phi = -2\arctan\left(\frac{\sqrt{1-u^2}}{u}\right) = -2\frac{u}{|u|}\arccos(|u|),$$

leading to the above expression for P (the choice to include the factor $u/|u|$ coincides with a choice of which branch of the inverse trigonometric functions to use). The vanishing of the local momentum means

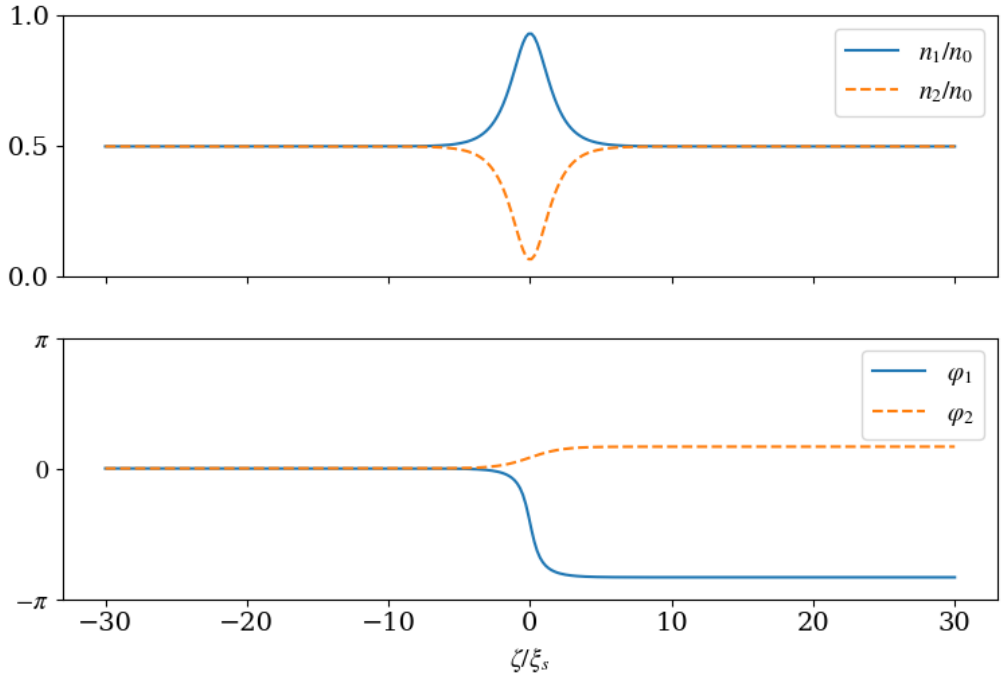

Figure 8: Condensate densities and phases in the one-parameter single-soliton solution valid in the miscible Manakov limit given in Eq. 52, with the velocity parameter $u = 0.5$.

that $P/n_0\hbar$ should be understood as a periodic variable which takes values in an interval of length π, and allows the energy to be explicitly written as a function of the momentum, giving a simple expression for the soliton's dispersion relation. Quite unlike that of an ordinary particle, it is non-monotonic and periodic (however, see chapter 3 for an argument why this periodicity is physically irrelevant). The effective mass is

$$m^* = -\frac{n_0\hbar}{c_s \sin\left(P/n_0\hbar\right)} = -\frac{n_0\hbar}{c_s\sqrt{1-u^2}},$$

which is always negative and diverges for $u \to \pm 1$, in which limit the soliton vanishes as a density perturbation and becomes an infinitely wide relative phase profile.

2.5.3 Easy-axis solitons

The simplest family of solitons of the easy-axis Landau-Lifshitz equation is parametrized by two quantities, so they are also known as bions. One possible choice for the pair of parameters is the velocity -2λ and the precession frequency ω. In the same adimensional units of Eq. 55, the components of the magnetization vector in a bion are [37]:

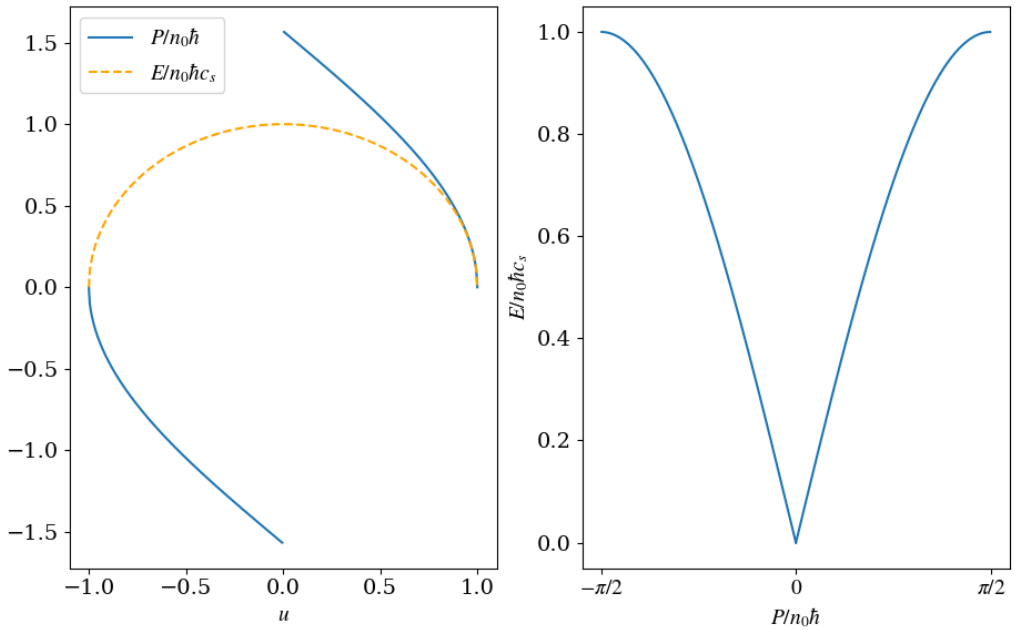

Figure 9: Energy and momentum of a soliton solution of the miscible Manakov-limit coupled GPEs. Both are plotted as functions of u in the left panel, while the right panel shows the dispersion relation $E(P)$.

$$\begin{cases} \mu_z = & 1 - \dfrac{4(1-\omega-\lambda^2)}{2-\omega-\sqrt{\omega^2+4\lambda^2}+2\sqrt{\omega^2+4\lambda^2}\cosh^2(\sqrt{1-\omega-\lambda^2}(\zeta+2\lambda t))} \\ \mu_x + i\mu_y = & 2\sqrt{2}\dfrac{\sqrt{1-\omega-\lambda^2}\sqrt{2\sqrt{\omega^2+4\lambda^2}\cosh^2(\sqrt{1-\omega-\lambda^2}(\zeta+2\lambda t))-\sqrt{\omega^2+4\lambda^2}+\omega+2\lambda^2}}{2\sqrt{\omega^2+4\lambda^2}\cosh^2(\sqrt{1-\omega-\lambda^2}(\zeta+2\lambda t))-\sqrt{\omega^2+4\lambda^2}+2-\omega} \\ & \cdot \exp\left(i\lambda\zeta + i\arctan\left(\dfrac{-2\lambda\sqrt{1-\omega-\lambda^2}}{\sqrt{\omega^2+4\lambda^2}+\omega+2\lambda^2}\tanh\left(\sqrt{1-\omega-\lambda^2}\zeta+2\lambda t\right)\right)\right). \end{cases} \tag{58}$$

This solution only exists in a region of parameter space defined by the inequality $\omega+\lambda^2 \leq 1$. In the GPE language, we have

$$\begin{cases} n_1 = & n_0\left[1-\dfrac{2(1-\omega-\frac{u^2}{4})}{2-\omega-\sqrt{\omega^2+u^2}+2\sqrt{\omega^2+u^2}\cosh^2(\sqrt{1-\omega-\frac{u^2}{4}}\frac{\zeta-uc_st}{\xi_s})}\right] \\ n_2 = & n_0\dfrac{2(1-\omega-\frac{u^2}{4})}{2-\omega-\sqrt{\omega^2+u^2}+2\sqrt{\omega^2+u^2}\cosh^2(\sqrt{1-\omega-\frac{u^2}{4}}\frac{\zeta-uc_st}{\xi_s})} \\ \varphi = & -\dfrac{u}{2}\dfrac{\zeta}{\xi_s}+\arctan\left(\dfrac{u\sqrt{1-\omega-\frac{u^2}{4}}}{\sqrt{\omega^2+u^2}+\omega+\frac{u^2}{2}}\tanh\left(\sqrt{1-\omega-\dfrac{u^2}{4}}\dfrac{\zeta-uc_st}{\xi_s}\right)\right) \\ \Phi = & u\dfrac{\zeta}{\xi_s}-\varphi \end{cases} \tag{59}$$

where the soliton moves at the velocity $v = uc_s$ and the total phase Φ is determined up to an arbitrary function of time. The physical precession frequency is $\omega_0\omega = (g_s n_0/\hbar)\omega$. The condition on the parameters now reads $\omega + u^2/4 \leq 1$. The structure of a bion is that of a region of depleted density in the majority component (whose asymptotic density is n_0) filled by the minority component (which is completely concentrated in the soliton, since its density vanishes at infinity). The total z-magnetization is

$$N = \int(1-\cos\theta)\frac{\mathrm{d}\zeta}{\xi_s} = 2\mathrm{arsinh}\left(2\sqrt{\frac{1-\omega-\frac{u^2}{4}}{\omega^2+u^2}}\right). \tag{60}$$

Entering into a little more detail, an important distinction in the family of bions is made by the sign of ω. For $\omega < 0$, the $u = 0$ solution (illustrated in Fig. 10, while the non-stationary solution is shown in Fig. 11) reads

$$\begin{cases} n_{1,2} = & \dfrac{n_0}{2}\left[1\pm\left(1-2\dfrac{1+|\omega|}{1+|\omega|\cosh^2(\sqrt{1+|\omega|}\frac{\zeta}{\xi_s})}\right)\right] \\ \varphi = & \dfrac{\pi}{2}\,\mathrm{sign}(\zeta). \end{cases} \tag{61}$$

Similarly to the easy-plane case, the static bion with negative frequency has a central z-magnetization of ± 1, and a phase discontinuity of π at its center. Its width decreases with increasing $|\omega|$. Indeed, $|\omega|$ should be taken significantly less than 1 to avoid the soliton's size being smaller than the spin healing length, in which case its long-wavelength description breaks down.

For $\omega > 0$, on the other hand, we have at $u = 0$

$$\begin{cases} n_{1,2} = & \dfrac{n_0}{2}\left[1\mp\dfrac{1-\frac{\omega}{1-\omega}\cosh^2(\sqrt{1-\omega}\frac{\zeta}{\xi_s})}{1+\frac{\omega}{1-\omega}\cosh^2(\sqrt{1-\omega}\frac{\zeta}{\xi_s})}\right] \\ \varphi = & 0, \end{cases} \tag{62}$$

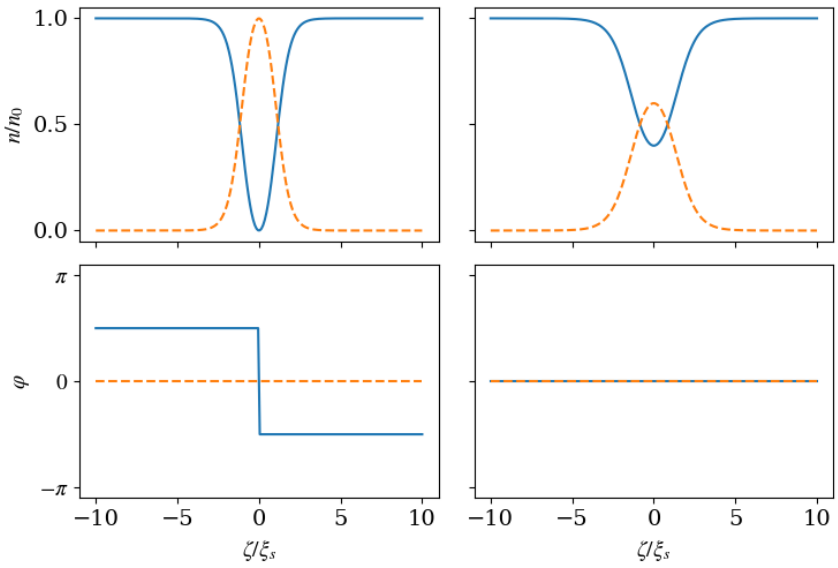

Figure 10: Condensate densities and phases in the stationary bion solution valid in the immiscible Manakov limit, as given by Eq. 59, for $u = 0$. On the left, $\omega = -0.4$, and on the right $\omega = 0.4$. Solid lines show the density and phase of component 1 and dashed lines those of component 2.

which differs from the negative-frequency case in that the order parameters are real and even rather than real and odd, and in that the central value of $\cos\theta$ now depends on ω and never reaches -1. Aside from these differences, the structure of the bions with negative and positive ω are quite similar. In both cases, they can be viewed as a bound state of two domain walls of opposite sign, with the region between them constituting a magnetized domain with respect to the uniform ground state. Indeed, in the limit of small ω and u, the soliton solution decomposes into a sum of two infinitely separated domain walls. Bions are illustrated in terms of quantities relative to condensate mixtures in Fig. 11.

The energy and momentum of the bion are (Fig. 12)

$$\begin{cases} P = n_0\hbar\dfrac{u}{|u|}\arccos\left(\dfrac{\omega+u^2/2}{\sqrt{\omega^2+u^2}}\right) & \text{(63a)} \\ E = 4n_0\hbar c_s\sqrt{1-\omega-\dfrac{u^2}{4}} = n_0\hbar c_s\left(4\tanh\left(\dfrac{N}{4}\right)+8\dfrac{\sin^2(P/2n_0\hbar)}{\sinh(N/2)}\right), & \text{(63b)} \end{cases}$$

from which it can be checked that $\partial E/\partial P = uc_s$. The last equation showcases the use of the alternative pair of parameters for the bion family (P, N), which are given above as functions of (ω, u).

The fact that N is an integral of motion even in the presence of external fields along z, which can lead to non-constant P, ω, and u, will be useful in chapter 3. There, we also explore the consequences of the fact that the bion's dispersion relation is periodic. Having introduced the theoretical elements the succeeding chapters will rely on, we now move to the presentation of the original results which constitute the body of this thesis.

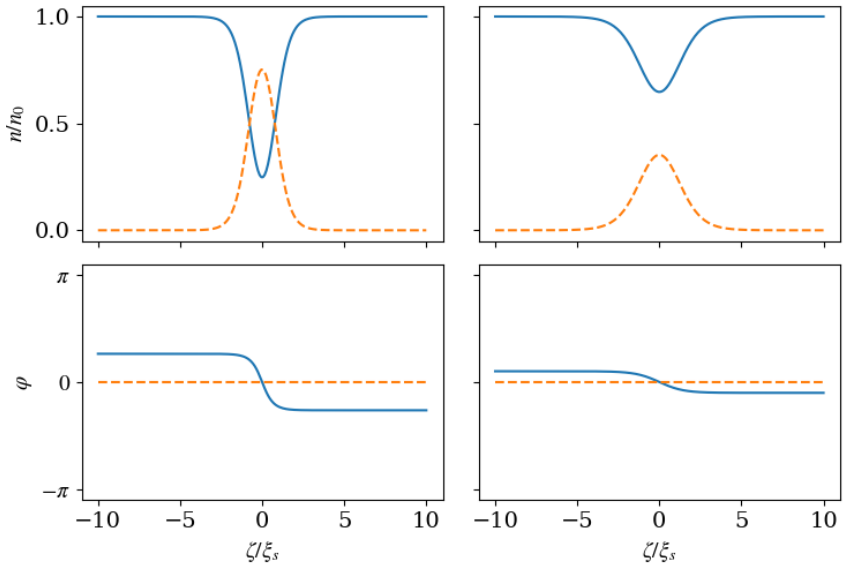

Figure 11: Condensate densities and phases in the bion solution valid in the immiscible Manakov limit, as given by Eq. 59, for $u = 0.8$. On the left, $\omega = -0.4$, and on the right $\omega = 0.4$. Solid lines show the density and phase of component 1 and dashed lines those of component 2. For clarity, phases are plotted with their constant-gradient terms subtracted, thus we graph $\varphi_1 - (3/2)\zeta/\xi_s$ and $\varphi_2 - (1/2)\zeta/\xi_s$.

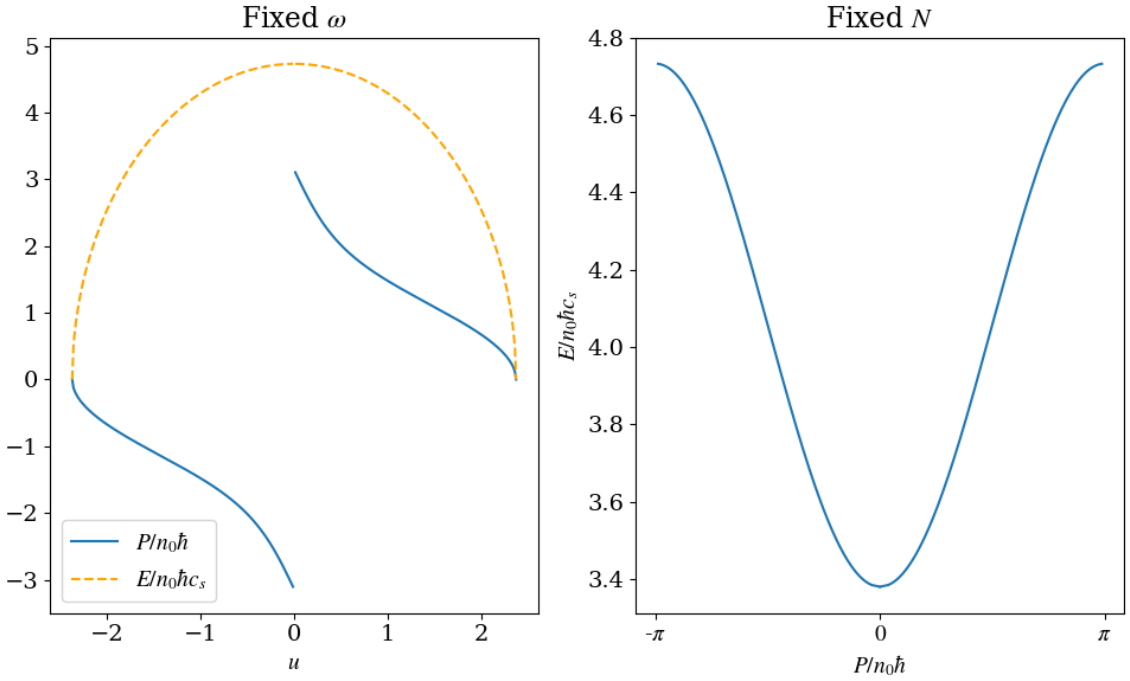

Figure 12: Energy and momentum of a bion solution of the immiscible Manakov-limit coupled GPEs. Both are plotted as functions of u at fixed $\omega = -0.4$ in the left panel, while the right panel shows the dispersion relation at fixed $N(\omega = -0.4, u = 0) \approx 4.96$. This will a useful representation of the dispersion because N is an integral of motion of the system even in the presence of external fields directed along z, in which case ω and u are not constant.

3 Magnetic soliton oscillations as Josephson physics

Periodic motion under the effect of a uniform force field is a counterintuitive phenomenon occurring in some peculiar dissipationless quantum-mechanical systems. The most well-known example is represented by Bloch oscillations of a particle in a periodic potential predicted at the dawn of quantum mechanics [38], which are due to the wave nature of particles and the consequent energy band structure. Another remarkable example due to quantum coherence is the AC Josephson effect, where a fixed voltage induces an oscillating current across a superconducting junction [39]. Such an effect also exists in other systems which break a continuous symmetry [40]. In particular it occurs in superfluid ^{3}He [41, 42] and ^{4}He [43] and in systems exhibiting Bose-Einstein condensation (BEC), such as ultra-cold gases [44, 45, 46], magnons [47] and exciton-polaritons [48]. Two weakly coupled ferromagnets or antiferromagnets can also demonstrate the AC Josephson effect for the spin current in a mechanism referred to as the spin-Josephson effect, see, e.g., [49, 50, 51, 51, 52].

A different instance of oscillatory motion under a DC drive concerns certain solitons in Galilean-invariant systems. To our knowledge, such behavior was first discussed in [53, 54], in the context of solitonic solutions of the dissipationless Landau-Lifshitz equation (LLE). More recently, similar dynamics have been found for two solitonic solutions in spinor condensates in ultra-cold gases: a magnetic soliton in a two-component BEC with very specific interaction strengths [55] and a ferro-dark soliton in the ferromagnetic phase of a spin-1 BEC [56]. Furthermore, it has been shown in [57, 58] that a single impurity in a zero-temperature one-dimensional Bose gas also exhibits a peculiar damped oscillating dynamics under a constant force.

In the LLE, Kosevich and collaborators attributed the strange dynamics to the periodic dispersion relation – just as in Bloch oscillations – and to the stability under an external uniform magnetic field of the easy-axis magnetic solitons. In the case of spinor condensates, the reason for the numerically observed dynamics was related to the oscillation between two solitonic solutions with positive and negative mass [55, 56]. Finally, for the impurity in the one-dimensional Bose gas the explanation of the periodic motion was based on the impurity cutting the gas and behaving as the barrier of a mobile Josephson junction [59], and on Bragg reflection induced by the strong bath correlation and the characteristic 1D spectrum [58].

In this section we first exploit the mapping between Bose mixtures and ferromagnetic systems to give a unified interpretation of this phenomenon alternative to previous ones [53, 55]: we argue that, as for the single impurity model of Ref. [59], the oscillations of the soliton in the presence of a constant force – such as represented in Fig. 13 – are due to an unconventional Josephson effect. This interpretation suggests that the phenomenon is not restricted to the exact solitonic solution or to regimes where the mapping between a two-component BEC and a ferromagnet is valid. We proceed to show that, indeed, the oscillating dynamics under a constant force is a more general feature of small spin domains. We then discuss the miscible case separately.

Such a robustness implies that it should be possible to (i) directly observe oscillating dynamics in a Galilean-invariant system using present technology in cold gas platforms (thus contributing to settle the controversy concerning the possible observation of this phenomenon [60, 61, 62]) and (ii) realize the analog of the voltage-current characteristic of a superconducting Josephson junction (SJJ). So far, indeed, the Josephson effect in BEC has been related to the coherent relative density oscillations between two weakly linked condensates, either in double well traps or in two hyperfine levels [44, 45, 63]. Such a dynamics is described by the so-called Bose-Josephson junction equations, i.e., nonrigid pendulum equations [7, 8], which interestingly show some new phenomena not observable with SJJs. The magnetic soliton, or more generally the magnetic domain under the external potential, instead realizes a perfect analogue of the AC SJJ (see also [64]). In addition, the Josephson junction picture provides an intuitive explanation of why solitons in an easy-plane ferromagnet, or equivalently in a miscible BEC mixture, are not expected to exhibit similar oscillations. Thanks to the miscible nature of the mixture, the soliton in this case does not constitute a barrier, so

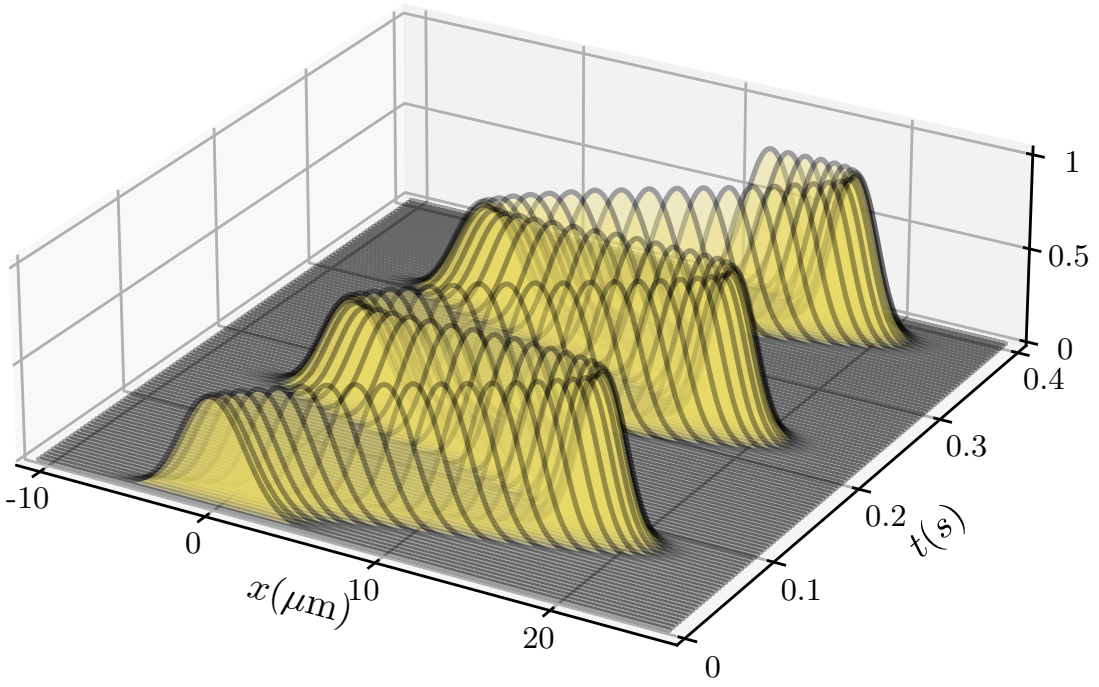

Figure 13: Numerical results for the evolution under a constant force of a dark-bright soliton in an immiscible mixture condensate of two hyperfine states of Na ($|F = 1, m_F = -1\rangle$ and $|F = 2, m_F = -2\rangle$). We represent the density of the minority component (in arbitrary units) as a function of position and time.

a Josephson junction is not realized.

We consider a magnetic soliton in an immiscible condensate mixture in the Manakov limit. The functional form of such a soliton, given in section 2.5.3, is characterized by two parameters: the conserved quantity associated to the total z-magnetisation $N = \int (1-\cos\theta)\,\mathrm{d}\zeta$ (in the Bose-mixture language $N = 2N_2/n_0\xi_s$, where N_2 is the number of atoms of the minority component) and the total momentum $P = (n_0\hbar/2)\int \partial_\zeta\varphi(1-\cos\theta)\,\mathrm{d}\zeta$. In terms of these quantities, the soliton energy reads:

$$\frac{E_{\mathrm{sol}}}{n_0\hbar c_s} = 4\tanh(N/4) + 8\,\frac{\sin^2(P/2n_0\hbar)}{\sinh(N/2)}. \tag{64}$$

This is a periodic function of the momentum, which suggests that if we apply a constant external force, such that the momentum increases linearly in time, the soliton should respond by oscillating. We stress that an adiabatic approximation is involved in this reasoning, which assumes that the application of the external force is able to explore the dispersion relation, i.e., that the Gross-Pitaevskii evolution of an initial soliton state leads to another state within the soliton family. This is valid provided the external potentials vary slowly enough to be approximately constant over the width of the soliton.

Motivated by the reasoning just outlined, we define an "external force" in the context of our binary BEC as an external quantity which is proportional to the time derivative of the system's total momentum, and so we set out to calculate $\dot{P}$. Clearly, in the absence of external potentials, the momentum is an integral of motion, as the system possesses spatial translation symmetry. This can be checked using the dynamical equations.

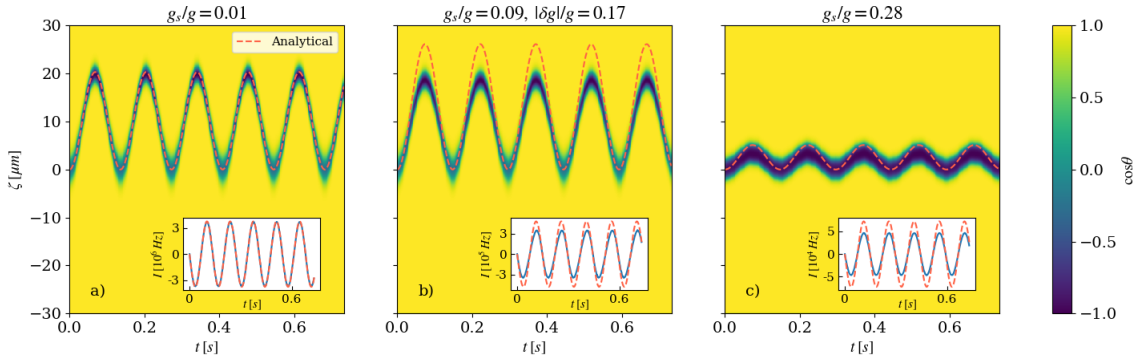

Figure 14: Numerical evolution of a spin domain under a linear differential potential for different values of the interaction strengths; (a) : $g_s/g = 0.01$, (b) : $g_s/g = 0.09$ and $|\delta g|/g = 0.17$, (c) : $g_s/g = 0.28$. The color plots display the relative density $\cos\theta$ as a function of position and time, while the insets show the particle current in the majority component across the spin domain during the same time interval. Close to the Manakov limit, the analytical expression in Eq. 67 accurately describes the domain's trajectory, while as g_s or δg increase, oscillations persist in the current and in the position of the domain, and their period is well-matched by our prediction. At the same time, the amplitude of the periodic trajectory decreases, so that the configuration comes to mimic a static Josephson junction in the high-g_s limit. Panel (b) shows that the phenomenon is visible and the amplitude and period reasonably close to predictable values with experimentally achievable interaction strengths.

Once this is established, we can ask how the momentum evolves for non-zero external potentials. To avoid having to solve the full dynamical equations with the addition of the potential terms, we examine the case in which the potentials are slowly varying on the length scales characterizing the state of the system. For a magnetic soliton, for example, the characteristic size is $\xi_s/\sqrt{1-u^2}$. In this limit, we assume that a solution of the dynamical equations found in the absence of external potentials remains an approximate solution after their inclusion up to a position-dependent phase rotation: that is, we assume that $\partial_t\varphi = \partial_t\varphi\big|_{\omega_D=0} + \omega_D(\zeta)$ (in the dimensionless units of Eq. 36b). With this approximation, it is straightforward to calculate the time derivative of the momentum:

$$
\begin{aligned}
\frac{2}{n_0\hbar}\dot{P} &= \frac{\mathrm{d}}{\mathrm{d}t}\int_{-\infty}^{+\infty}(1-\cos\theta)\frac{\partial\varphi}{\partial\zeta}\,\mathrm{d}\zeta \\
&= \int_{-\infty}^{+\infty}(1-\cos\theta)\frac{\partial}{\partial t}\frac{\partial\varphi}{\partial\zeta} + \frac{\partial\varphi}{\partial\zeta}\frac{\partial}{\partial t}(1-\cos\theta)\,\mathrm{d}\zeta \\
&= \int_{-\infty}^{+\infty}(1-\cos\theta)\frac{\partial}{\partial\zeta}\frac{\partial\varphi}{\partial t} + \frac{\partial\varphi}{\partial\zeta}\frac{\partial}{\partial t}(1-\cos\theta)\,\mathrm{d}\zeta \\
&\approx \int_{-\infty}^{+\infty}(1-\cos\theta)\frac{\partial}{\partial\zeta}\left(\frac{\partial\varphi}{\partial t}\bigg|_{\omega_D=0} + \frac{g_s n_0}{\hbar}\omega_D(\zeta)\right) + \frac{\partial\varphi}{\partial\zeta}\frac{\partial}{\partial t}(1-\cos\theta)\,\mathrm{d}\zeta \\
&= \frac{2}{n_0\hbar}\dot{P}\bigg|_{\omega_D=0} + \frac{g_s n_0}{\hbar}\int_{-\infty}^{+\infty}(1-\cos\theta)\frac{\mathrm{d}\omega_D}{\mathrm{d}\zeta}\,\mathrm{d}\zeta\,.
\end{aligned}
$$

We are thus left with

$$\dot{P} = \frac{g_s n_0^2}{2} \int_{-\infty}^{+\infty} (1 - \cos\theta) \frac{\mathrm{d}\omega_D}{\mathrm{d}\zeta} \, \mathrm{d}\zeta \tag{65}$$

for the general case of a slowly varying differential potential. To obtain a constant force, it is sufficient to suppose that the differential potential is a linear function:

$$\omega_D(\zeta) = \omega_D(0) + \eta\zeta \implies \dot{P} = \frac{g_s n_0^2}{2} \eta N. \tag{66}$$

We are thus led, by analogy with Newton's second law, to consider the dynamics of a magnetic soliton under the application of linear potentials with a small gradient $\eta \ll \sqrt{1-u^2}$. More specifically, we will assume $V_{\mathrm{ext},1} = 0$ and $V_{\mathrm{ext},2}/g_s n_0 = -\eta\zeta$, which is a convenient choice for simulations because applying a potential only to the localized minority component decreases border effects in a finite system, thanks to the fact that $V_{\mathrm{ext},2}$ may have a larger slope without attaining excessively large values in the smaller region where the density of the minority component is non-zero.[6]

In this scenario, N remains exactly constant while $\dot{P} \propto \eta N$: the differential potential gradient assumes the role of a constant force, and the momentum increases linearly in time. Within the adiabatic approximation we can use Eq. (64) to find the evolution of the soliton position X through the relation $\dot{X} = \partial E_{\mathrm{sol}}/\partial P$ [65]. This yields

$$X(t) = X(0) + 4\xi_s \frac{\cos\big(P(0)/n_0\hbar\big) - \cos\big(P(t)/n_0\hbar\big)}{\eta N \sinh(N/2)}. \tag{67}$$

Since $P(t)$ is linear, we find a sinusoidal trajectory. This motion corresponds to an adiabatically conserved energy $E = E_{\mathrm{sol}} - (\eta N X) n_0 \hbar c_s$. In dimensional units, the constant force applied to the soliton is

$$f = N_2 \frac{\mathrm{d}V_{\mathrm{ext},1} - V_{\mathrm{ext},2}}{\mathrm{d}\zeta} = \frac{\eta N_2 g_s n_0}{\xi_s}$$

and the period

$$\mathcal{T} = \frac{2\pi\hbar n_0}{f}$$

is independent of g_s. The dimensional amplitude is

$$\mathcal{A} = \frac{4 g_s n_0^3 \xi_s}{f \sinh\big(N_2/n_0\xi_s\big)},$$

a decreasing function of g_s.

We performed simulations to check our prediction, solving Eq. 13 numerically starting from a stationary soliton-like state obtained from imaginary-time evolution via the procedure detailed in [66], and under a potential consisting of a hard wall confining both components to a region much larger than the soliton, supplemented by a linear potential acting on the minority component. For concreteness, and because it is a promising experimental platform, we take the mass to be that of ^{23}Na. The results of our simulations are illustrated in Fig. 14: panels (a) and (c) respectively illustrate the good quantitative agreement of our predictions for the dynamics close to the Manakov limit and the persistence of the phenomenon and reasonable

[6] See 3.2 for a discussion of the case $V_{\mathrm{ext},1} + V_{\mathrm{ext},2} = 0$, which is in general safer with respect to the condition of constant total density, but leads to the introduction of a higher-frequency component in the soliton oscillations due to boundary effects. In the general case, the variation of $V_{\mathrm{ext},1} + V_{\mathrm{ext},2}$ across the system must be small compared to gn_0 to guarantee $n_0 = \mathrm{const.}$, as explained in section 2.3.1.

agreement with predictions for larger g_s/g, which we will discuss shortly. Panel (b) displays the results of a simulation performed with experimentally accessible parameters, using the scattering lengths between the $|F = 1, m_F = -1\rangle$ and $|F = 2, m_F = -2\rangle$ hyperfine states of ^{23}Na, demonstrating good agreement with our predictions even in the case where the condition $g_{11} \neq g_{22}$ breaks the mixture's $\mathbb{Z}_2$ symmetry, and presenting evidence that it is possible to observe soliton oscillations in the laboratory.

Previous works have described soliton oscillations like those we predict as Bloch oscillations [53] or attributed them to the periodically changing sign of the soliton's effective mass [55]. Although these are appropriate descriptions of a quasiparticle with a periodic dispersion relation, they do not explain why the dispersion is periodic in the first place. To do so, it is fruitful to step back from the quasiparticle picture and to consider the soliton as a configuration of a phase-coherent field. Indeed, the momentum and dispersion relation of this and other solitons are properly defined only by accounting for a global quantity, namely the counterflow momentum (cf. [67, 68, 65] and [1], Ch. 5). Once this is done, one finds that the momentum P is proportional to the majority-component phase difference at infinity $\Delta\varphi_1 \equiv \varphi_1(+\infty) - \varphi_1(-\infty)$, since total current conservation allows the momentum to be expressed as $P = (n_0\hbar/2)\int(\partial_x\varphi - \partial_x\Phi)\,\mathrm{d}x = -n_0\hbar\Delta\varphi_1$. We now propose what we consider to be a more insightful explanation of magnetic soliton oscillations by explicitly deriving Josephson equations which hold in the slightly immiscible mixture with a spin domain subject to a small uniform differential potential gradient.

The Josephson effect was first described in the context of superconducting circuits [39]. A superconducting Josephson junction is composed of a thin layer of insulating material separating two superconductors. In this situation, a constant electric current will flow across the junction in the absence of a potential difference across it (DC Josephson effect), and if a constant potential difference is applied, the current through the junction is sinusoidal in time (AC Josephson effect). These phenomena are essentially due to coherence of the electrons in superconductors, where a complex order parameter attributable to condensation of Cooper pairs is defined. This order parameter may have different values on either side of the barrier, in which case electrons will tunnel across it with a current proportional to the sine of the phase difference in the two superconductors. At the same time, the time derivative of this phase is proportional to the potential difference across the junction, accounting for both the DC and the AC effects. The phenomenon is described by the Josephson equations for the current I, phase difference ϕ, and potential difference ΔV:

$$\begin{cases} I = I_c \sin(\phi) & \text{(68a)} \\ \dfrac{\partial\phi}{\partial t} = \dfrac{2e}{\hbar}\Delta V, & \text{(68b)} \end{cases}$$

where the critical current I_c depends on the properties of the junction.

This configuration has clear analogies to our system, where coherence also plays a major role. As a matter of fact, the Josephson effect is a quite general feature of systems with a spontaneously broken continuous symmetry [40]. This symmetry breaking implies the definition of an order parameter in the system; whenever it takes two different uniform values in two regions connected by a weak coupling, it is possible to derive Josephson equations for the Noether current associated with the broken symmetry, describing a generalized DC Josephson effect, as well as an AC effect when a chemical potential difference is imposed between the two regions. In the latter case, the energy difference immediately implies a time dependence, which is oscillatory for the evolution derived from a quantum-mechanical treatment of the order parameter dynamics.

This is exactly the situation realized by a soliton in an immiscible condensate mixture. The majority component is described by the order parameter ψ_1 associated with the spontaneous breaking of $U(1)$ symmetry, which implies that the condensate has a definite phase φ_1, and the order parameter is defined in two regions separated by the minority component condensate. The essential role of the minority component thus

appears as that of a barrier, which weakly couples the regions to either side of it thanks to the immiscibility of the system. The Noether current associated with the broken symmetry is simply the particle current of the majority component, which tunnels through the barrier. The difference in our scenario with respect to the more familiar case is that the barrier's position is not fixed. However, in the reference frame comoving with the soliton, the conditions for the realization of a Josephson junction are met. As long as the total density is constant and n_2 can be considered zero outside of the soliton core, the majority density n_1 is the same on either side of the barrier in the absence of an external potential, so the difference in the chemical potential μ_1 across the barrier is zero. This implies the occurrence of the DC Josephson effect, which has a rather trivial interpretation in terms of condensate physics: the variation in density in the soliton is associated, by virtue of local particle number conservation, with a non-zero current density. The majority-component particle current through the soliton is

$$\begin{aligned} I(t) =& \frac{\mathrm{d}}{\mathrm{d}t}\int_{X(t)}^{+\infty} n_1(\zeta,t)\,\mathrm{d}\zeta = -n_0\dot{X}(t) = -n_0\frac{\partial E_{\mathrm{sol}}}{\partial P} = -2n_0c_s\frac{\sin\left(P/n_0\hbar\right)}{\sinh(N/2)} \\ =& I_0\sin\left(\Delta\varphi_1\right) \end{aligned}$$

with $I_0 = 2n_0c_s/\sinh(N/2)$. Here we have used the fact that the soliton moves rigidly and that the momentum, which is an integral of motion, is given by $P = -n_0\hbar\Delta\varphi_1$ (according to Eq. 45 with the immiscible ground state condition $\cos\theta_0 = 1$). Since the relevant variation of φ_1 occurs within the soliton core, the phase difference at infinity $\Delta\varphi_1$ is approximately equal to the phase difference across the soliton, so that the above expression takes the form of the Josephson equation for the current. The DC Josephson effect thus emerges as a restatement of the familiar fact that a soliton moves at constant velocity in the absence of external fields.

The more interesting case is that with a non-zero potential difference. The application of an external linear potential acting on ψ_1 contributes to the chemical potential μ_1, applying a chemical potential difference between either side of the barrier proportional to the slope of $V_{\mathrm{ext},1}$. Thus the conditions are realized for the occurrence of the AC Josephson effect. The above reasoning for the current can be repeated in the same way, except that $\dot{X}(t) = \partial E/\partial P \neq$ const. since P is now a function of time. Also, the soliton no longer moves rigidly during its dynamics, but the weaker assumption that it is symmetrical with respect to its center is sufficient for us to write $I = -n_0\dot{X}$. The restatement of the result $\dot{P} = (g_s n_0^2/2)\eta N$ in terms of the relation between the momentum and the majority-component phase change yields an expression for the time derivative of $\Delta\varphi_1$. The resulting pair takes the form of Josephson equations for our immiscible system:

$$\begin{cases} I(t) = I_0\sin\left(\Delta\varphi_1\right) & \text{(69a)} \\ \dfrac{\mathrm{d}}{\mathrm{d}t}\Delta\varphi_1 = -\dfrac{\eta N}{2}, & \text{(69b)} \end{cases}$$

where t is given in units of $g_s n_0/\hbar$. Note that the second equation is a general result in the immiscible Manakov limit, independent of the configuration of the system. As for the superconducting junction, the critical current I_0 is determined by the properties of the junction, as it depends on the number of atoms N_2 in the barrier and on the quantities n_0 and g_s, but not on the external parameter η. The total z-magnetization N associated with the barrier also determines how strongly the external potential influences the phase, analogously to the Cooper pair charge $2e$ that appears in the equations for the superconductor. We write Eq. 69b in adimensional units to underline this; in dimensional units it reads $\mathrm{d}\Delta\varphi\,/\,\mathrm{d}t = -f/n_0\hbar$. Taking into account $I_0 = -n_0\dot{X}$, one recovers the trajectory in Eq. 67 from these equations as a consequence of the AC Josephson effect.

It is noteworthy that the apparent complication of a mobile barrier actually simplifies the equations in our regime: the density on either side of the soliton remains constant while the left and right populations change thanks to the fact that the soliton position changes. This means that the only contribution to the chemical potential difference across the junction is that due to the external potential gradient. The constant density also implies that the full Bose-Josephson physics more usually encountered in BECs, wherein the density imbalance and the phase difference between two condensates are both dynamical variables obeying coupled nonlinear differential equations, is not realized; in particular, there is no self-trapping regime in our case. One may say that the system keeps itself in the linear regime of the Bose-Josephson junction, i. e. the limit of zero population imbalance. As a result, we have a bosonic system reproducing the physics of a superconducting Josephson junction.

The following picture thus emerges: in the soliton structure we consider, the left and right part of the majority component are separated by the minority component which acts as the analogue of a weak link between two superconductors. In such a configuration, an external potential generates a linear increase over time of the phase difference $\Delta\varphi_1$ between the right and left parts of the majority component [69], as described by Eq. 69b. The current induced in the majority component by this phase mismatch is a periodic function of $\Delta\varphi_1$ [see Eq. 69b] and thus of time. The resulting oscillations trigger, by total particle number conservation, similar and opposed oscillations of the minority component, as observed in Fig. 13. The immiscibility of the two components makes the structure particularly robust and the interpretation of the soliton as a Josephson junction does not depend on the precise values of the mixture's interaction parameters. Thus, although we used the decoupling from the total density dynamics close to the Manakov limit and the mapping to the Landau-Lifshitz equation to treat the problem analytically, we expect oscillations to occur under a constant differential potential gradient even far away from the Manakov limit, as well as for localized spin domains more generally, rather than for solitons specifically. We have confirmed this by solving Eq. 13 numerically for increasing values of g_s (we increase g_{12} while keeping g_{11} and g_{22} constant). Examples of the results are shown in Fig. 14(b,c). We observe an oscillatory trajectory whose period is inversely proportional to the external potential gradient and does not depend strongly on g_s or δg.

The particle current remains sinusoidal, with an amplitude decreasing with increasing g_s, consistent with the fact that this corresponds to a greater energy barrier for the current to tunnel through. While our prediction for the critical current and oscillation amplitude deviate from simulations at higher g_s and δg, the period continues to match, consistently with the fact that the Josephson frequency does not depend on the characteristics of the junction.

These observations strengthen the proposed Josephson-junction interpretation and reframe the sinusoidal soliton trajectory found in an easy-axis ferromagnet and in a slightly immiscible condensate mixture as a special case of a more general phenomenon. In the LLE language, magnetic soliton oscillations in easy-axis ferromagnets are, according to our picture, to be interpreted as manifestations of the spin Josephson effect, with the soliton itself acting as a junction. This interpretation was missed for a long while after the problem was noticed in ferromagnets, but it arises naturally if considered in terms of an immiscible two-component BEC. In both the ferromagnet and the binary condensate, phase coherence in the order parameter plays the key role.

We expect an oscillating current to arise in a binary condensate mixture any time a junction is realized, irrespective of the precise parameter values or profile of the initial state. Possible avenues for future research therefore include the effects of the Josephson mechanism under conditions different from the ones considered here. Having presented the main result of this section, we address some technical aspects of their derivation and consider the miscible case in the following.

3.1 Values of the parameters used in the numerical simulations

We present here the parameters used in the simulations whose results are reported above. The code, which is described in the Appendix, numerically solves coupled one-dimensional Gross-Pitaevskii equations whose interaction strengths are obtained from three-dimensional values, renormalized as for a cigar-shaped condensate in a harmonic trap with $\omega_y = \omega_z \equiv \omega_\perp \gg \omega_x$. We denote as $a_\perp = (\hbar/m\omega_\perp)^{1/2}$ the transverse harmonic oscillator length and by a_{ij} the s-wave scattering length characterizing the low-energy 3D interaction between components i and j. We work in the 1D mean field regime [70] where $(a_{ij}/a_\perp)^2 \ll n_0 a_{ij} \ll 1$. In this regime $g_{ij}^{1D} = 2\hbar\omega_\perp a_{ij}$. The results in Fig. 14 are obtained for $a_{11} = a_{22} = 54.5a_0$, $a_{12} = 55.1a_0$, where a_0 is the Bohr radius. In panel (b) we use $a_{11} = 54.5a_0$, $a_{22} = 64.3a_0$, and $a_{12} = 64.3a_0$, which are the scattering lengths between the hyperfine states $|F = 1, m_F = -1\rangle$ and $|F = 2, m_F = -2\rangle$ of ^{23}Na, while in panel (c) we keep $a_{11} = a_{22} = 54.5a_0$ and use $a_{12} = 69.6a_0$. The total densities at the center of the trap are $n_0^{(a)} = 3.3 \cdot 10^9 \mathrm{m}^{-1}$, $n_0^{(b)} = 3.6 \cdot 10^8 \mathrm{m}^{-1}$, and $n_0^{(c)} = 3.3 \cdot 10^8 \mathrm{m}^{-1}$.

The different potentials acting on the two components can be realized by means of a combined magneto-optical potential whose magnetic and optical parts are both linear. The electric field will exert the same force f_E on both components, while the magnetic field will affect the component with larger magnetic moment more strongly. Formally, we can write the external potential contribution to the Hamiltonian as

$$\hat{V}_{\mathrm{ext}} = f_B \hat{\zeta} \left(|1\rangle\langle 1| - 2\,|2\rangle\langle 2|\right) + f_E \hat{\zeta}\left(|1\rangle\langle 1| + |2\rangle\langle 2|\right),$$

where we use the shorthand notation $|F\rangle \equiv |F, m_F = -F\rangle$ ($F = 1$ or 2). The condition to obtain $V_1 = 0$, $V_2 = f \cdot \zeta$ therefore becomes

$$\begin{cases} f_B + f_E = 0 \\ -2f_B + f_E = f, \end{cases}$$

which is solved by $f_B = -f_E = -f/3$. The magnetic potential gradients used in the simulations correspond, through the expression $V_B = \mu_B |\mathbf{B}|/2$ (where μ_B is the Bohr magneton) for the magnetic moment potential energy, to magnetic field gradients of 1.1 G/m, 0.9 G/m, and 1.2 G/m respectively. For such gradients the magnetic field change is very small over the size of the cloud and the scattering lengths are thus practically constant.

3.2 Equal and Opposite Potentials

The sum $V_{\mathrm{ext},1} + V_{\mathrm{ext},2}$ couples to the total density n in the Lagrangian of the system, and has no equivalent in the Landau-Lifshitz picture, where the magnitude of the magnetization vector is strictly constant. For these reasons, it may seem preferable to use equal and opposite linear potentials to study the dynamics of the condensate mixture, to ensure $V_{\mathrm{ext},1} + V_{\mathrm{ext},2} = 0$ and avoid exciting the total density degree of freedom. Actually, as indicated in the main text, a non-zero total potential does not necessarily break the condition of constant density. In fact, using $V_{\mathrm{ext},1} = -V_{\mathrm{ext},2} = \eta\,\zeta/2$ complicates the dynamics by acting on the majority component across the entire size of the system, causing the initially flat majority density profile to tilt back and forth periodically, as an effect of the edges of the system. These oscillations affect the motion of the soliton, showing up as a higher-frequency component in its trajectory, as shown in Fig. 15. The effect is more noticeable at higher g_s/g, since the amplitude of the Josephson oscillations on which the finite-size oscillations are superimposed becomes smaller as the energy barrier grows higher. Thus the trajectory comes to look very different from the sinusoidal curve seen at low g_s/g - but nonetheless the particle current remains sinusoidal. In this case, a non-sinusoidal trajectory and variations in the background density conspire to keep the behavior of the current in line with the AC Josephson effect, although its period is modified.

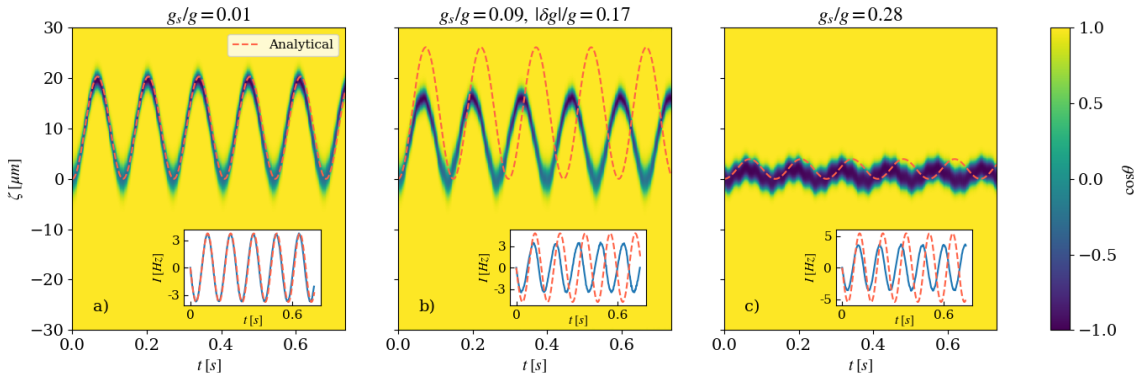

Figure 15: Numerical evolution of a spin domain under a linear differential potential with $V_{\text{ext},1} = -V_{\text{ext},2}$ for different values of the interspecies interaction strength. At higher g_s/g, the higher-frequency component due to background density oscillations becomes more visible, but the current remains sinusoidal rather than resembling the domain's trajectory.

3.3 Adiabatic soliton motion

A more detailed view of the approximations we utilize in our analytic treatment can be reached by considering the energy of the system. In a generic configuration of the coupled condensates, with the boundary conditions $n_1 \to n_0$ and $n_2 \to 0$ at $\zeta \to \pm\infty$, the energy is given by the Gross-Pitaevskii expression

$$\begin{aligned} E_{GP} = \int \Big[&\frac{\hbar^2}{2m}\left(|\partial_\zeta \psi_1|^2 + |\partial_\zeta \psi_2|^2\right) + V_{\text{ext},1}(n_1 - n_0) \\ &+ V_{\text{ext},2} n_2 + \frac{g}{2}(n_1^2 + n_2^2 - n_0^2) + g_{12} n_1 n_2 \Big] \, \mathrm{d}\zeta \,, \end{aligned} \tag{70}$$

which, in the limit of small and positive $g_{12} - g$ implying constant total density, in adimensional variables and using the (θ, φ) variables, reduces to

$$\begin{aligned} E = \int \Big[&\tfrac{1}{2}(\partial_\zeta \theta)^2 + \tfrac{1}{2}\sin^2\theta(1 + (\partial_\zeta \varphi)^2) \\ &+ \omega_D(\zeta)(\cos\theta - 1) \Big] \, \mathrm{d}\zeta \,. \end{aligned} \tag{71}$$

This expression corresponds to the energy of an equivalent magnetic system governed by the easy-axis Landau-Lifshitz equation. If (θ, φ) are those of a soliton solution parametrized by the position X and momentum P, this yields the energy

$$\begin{aligned} E &= E_{\text{sol}}(P) + \int \omega_D(\zeta)(\cos\theta - 1)\, \mathrm{d}\zeta \\ &\approx E_{\text{sol}}(P) - \omega_D(X) N, \end{aligned} \tag{72}$$

where E_{sol} is the soliton's energy as given in Eq. 64 and N is the total z-magnetization. The final expression in (72) gives the Hamiltonian governing the adiabatic motion of the soliton, X and P being the relevant canonical variables. It is obtained in the approximation that $\omega_D(\zeta)$ varies over a typical length scale much larger than the width of the soliton. For linear potentials, this means $\eta \ll 1$.

It should be noted that, if the external potentials are too large, they will break the condition of constant total density and thus prevent the mapping of the coupled GPEs to a Landau-Lifshitz equation, invalidating our analytical treatment and complicating the interpretation as a Josephson junction. Quantitatively, this means that the difference between the maximum and minimum values of the external potentials should be small compared to the chemical potential. This criterion is suggested by the arguments of section 2.3.1, and simulations show that if this condition is violated, large density gradients in the initially flat background form and lead to shock waves which quickly break the junction. Numerically, the oscillations are robust up until this happens. Note that, by only applying a potential to the minority component, this condition is weakened, as only the potential difference over the region where the minority density is non-zero is relevant. In this case, the condition becomes equivalent to the one discussed above, imposing $\eta \ll 1$.

3.4 The miscible case

The research reported in this section stemmed from the observation that easy-axis magnetic solitons have a periodic dispersion relation. This is also true of magnetic solitons in the easy-plane LLE. Thus, similar questions to those we have considered above can be posed for a miscible mixture: can the periodicity in the dispersion relation be attributed to the creation of a mobile Josephson junction? Does this result in an oscillatory current across the soliton when it is subjected to a linear differential potential and is this accompanied by periodic motion of the soliton itself? Does this effect also arise in the generic case of a magnetized domain (as opposed to a true soliton), as it does in immiscible mixtures? Our investigations suggest that some fundamental differences exist between the miscible and immiscible regimes.

A key difference regards the formation of a mobile Josephson junction. In an immiscible mixture, a region where one component has a high density is able to act as a barrier to the other component. In a miscible mixture, on the other hand, mixing between the two components is favored, so such a configuration can no longer be said to constitute an effective barrier. Rather, the initial barrier is typically unstable and will quickly be destroyed by the mixing of the two condensates (even in the absence of an external force). In the absence of a stable barrier, the argument leading to an interpretation in terms of a Josephson effect is untenable.

The situation is somewhat different when dealing with solitons. In this case, even in the miscible case the object in question is stable and has its own dynamics: a soliton translates unperturbed at constant velocity in a homogeneous system, and in a weakly inhomogeneous system, its motion can be described thanks to a local density approximation [65]. In the presence of a linear potential acting differently on the two components, this approach runs into some difficulties. One of them is the question of the stability of the soliton under such a force: it may happen that, favoring mixing, the force destroys the soliton (see below). Another aspect is the behavior of the easy-plane soliton for increasing velocity: let us assume that a soliton initially at rest is subject to a constant force that drags it toward negative ζ and linearly increases its momentum[7]. In this case, its representative point (E_{sol}, P) in Fig. 16 will move from the left-most point of the curve ($V = 0^-$) down to the origin, following the black dispersion relation. When the representative point gets close to the origin, the width of an easy-plane soliton diverges and its amplitude vanishes[8]. In this situation the adiabatic hypothesis breaks down and the soliton decays into elementary excitations.

A way to avoid this decay is to introduce a hard wall potential which prevents a constant rate of increase of the momentum. In this case, the velocity and momentum of the soliton bouncing off the hard wall are reversed and the soliton changes branch of the dispersion relation, as illustrated schematically by the red

[7] The soliton is accelerated counter to the force.

[8] In this instance, the behavior of the easy-plane soliton is similar to that of a dark soliton in a one component condensate, as discussed in a limiting case in Ref. [71].

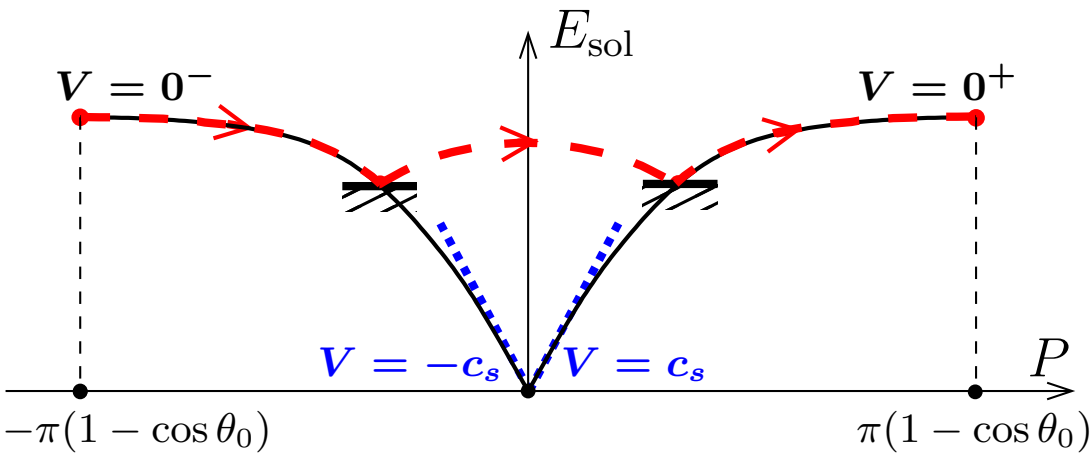

Figure 16: Black solid line: Dispersion relation of the easy-plane soliton for a relative background density $(n_1 - n_2)/n_0 = \cos\theta_0$. In adimensional units, $|P|$ varies between 0 and $\pi(1-\cos\theta_0)$ and $E_{\rm sol}$ between 0 and $2\sin\theta_0 - 2\theta_0\cos\theta_0$. The dashed blue lines correspond to the hydrodynamic limit: $E_{\rm sol} = \pm c_s\, P$, with $c_s = \sin\theta_0$. Thick dashed red line: adiabatic motion with the soliton bouncing off a hard wall (see the text).

dashed line in Fig. 16. Conservation of energy will let the representative point of the soliton reach the rightmost point of the dispersion relation (with zero velocity) and then start over the same downward motion. This is the analog of a ball bouncing off the ground under the effect of the gravitational acceleration.

We tested this scenario by running numerical simulations to probe the behavior of solitons in a miscible mixture under a constant external force for various values of several parameters (the relative values of the particle numbers N_1 and N_2, the total density, the interaction strength g_s, the external force, the initial velocity of the soliton) and the results, of which two representative examples are presented in Fig. 17, are compatible with the above scenario: the soliton is initially accelerated counter to the force (towards negative ζ in our case) until it reaches the wall of the box potential in which the simulations are run. At this point it bounces back and moves in the positive ζ direction until it stops and starts the same motion again. We note, however, that the adiabatic hypothesis breaks down for forces typically smaller than for easy-axis solitons (as already pointed out in [37]). In the presence of a sizeable external force (i.e., when η increases), the velocity of the soliton is large by the time of the bounce, and this is associated to a breakdown of adiabaticity: the width of the soliton is large at the point where the gradient of external potential is the greatest. In this case, the bouncing is accompanied by a sizeable amount of radiation, as illustrated in the right-hand panel of Fig. 17. A slightly counter-intuitive phenomenon is then observed: the soliton, having lost energy during the bounce, sees its velocity increased and is thus able to reach a point further away from the hard wall than its initial position. This effect is increased at the next bouncings, eventually leading to a decay of the soliton. This mechanism is clearly at work in the right-hand panel of Fig. 17 and also, although in a less pronounced way, in the left-hand panel (which corresponds to a lower value of η).

When the adiabatic approximation holds, one can describe its motion by considering the soliton as a classical particle [65]. The situation is particularly simple in a miscible mixture with equal proportion of the two components, as considered in Fig. 17. In this case the position X of the center of the soliton during its

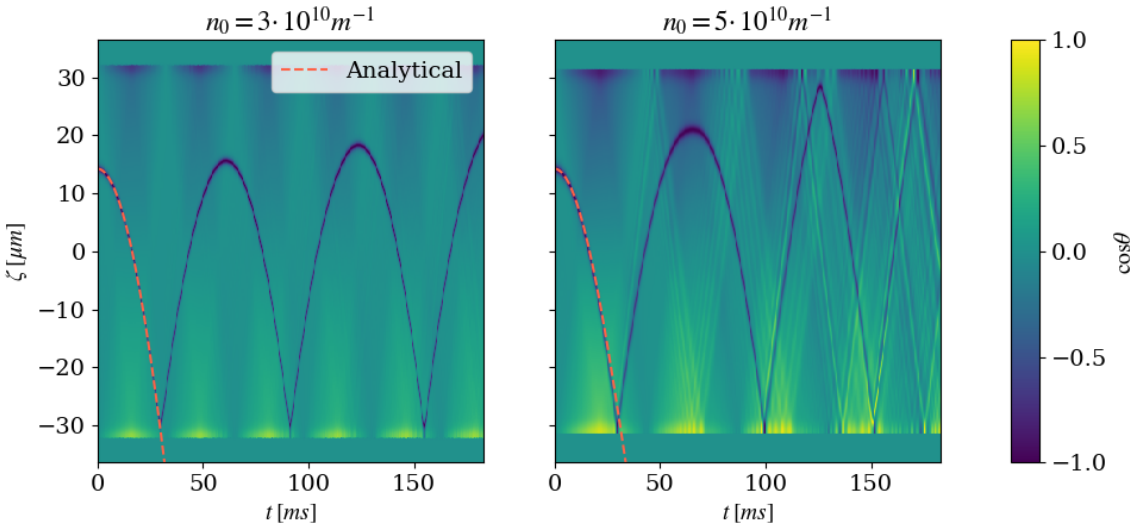

Figure 17: Numerical evolution of a magnetic soliton in a miscible mixture ($g_s/g = -0.01$) under a linear differential potential with gradient $\eta = 1.6 \times 10^{-3}$ (upper panel) and $\eta = 1.3 \times 10^{-2}$ (lower panel). The background relative density is initially zero ($n_1 = n_2$: $\cos\theta_0 = 0$). The soliton in the upper panel is stable on the timescale in which the one in the lower one is destroyed. The dashed curves correspond to the analytic prediction (67).

initial motion before bouncing is given, in adimensional units, by

$$X(t) = X(0) - \frac{2}{\eta\pi}\left[1 - \cos(\eta\pi t/2)\right] . \tag{73}$$

The good agreement of this prediction with the numerical simulations presented in Fig. 17 supports the above analysis of the ingredients governing the dynamics of an easy-axis soliton.

It is worth emphasising that during our numerical simulations, the miscible mixture proved much more delicate to treat within an adiabatic approximation than the immiscible one. As stated above, we attribute this difference to the robustness granted by phase separation to a spin domain in the immiscible phase, thanks to which the dynamics are not very sensitive to the initial condition. In the miscible phase, on the other hand, it is important for the initial state and all subsequent states in a hypothetical adiabatic evolution to be close to a magnetic soliton state. However, we know the exact solitonic solutions only at the demixing transition, whereas for finite $|g_s|/g$, these states are only approximate solutions of the Gross-Pitaevskii equation. Decreasing $|g_s|/g$ makes this discrepancy less significant, but also makes spin excitations softer (as can be seen, for example, from the spin speed of sound $c_s = \sqrt{|g_s| n_0/2m}$). This means that any external field will excite the spin channel more strongly, making adiabaticity harder to achieve. Correspondingly, it proved necessary in simulations to raise the total density in order to find good agreement with Eq. (73).

4 Soliton collisions and transmission at an interface

In light of the special collisional properties of solitons in integrable equations, it is interesting to investigate the behavior of colliding solitary waves in the coupled GPE system, in which the non-zero value of g_s or δg breaks integrability. If $g_s \ll g$ and $\delta g \ll g$, we may expect the collisions to be similar to the integrable case. We will present results for collisions in a miscible system. Our approach will be to run simulations of the coupled GPEs with various values of g_s and δg in which solitary waves approximating the soliton solutions given in Eq. 56 are made to collide. While these are exact solutions with solitonic collisional properties in the limit $g_s,\ \delta g \to 0$, the simulations will demonstrate deviations from the integrable behavior. In particular, we find that the waves retain their identities after colliding, allowing us to calculate phase shifts and obtain good agreement with the IST prediction for the LLE at small g_s and δg, while the collisions become increasingly inelastic farther from the Manakov limit (in the sense that the solitary wave parameters, in particular their velocities, are modified by the collision). We also test the property, which holds as a theorem for an integrable system, of N-body collisions reducing to pairwise interactions in the case $N = 3$, and find that this property is remarkably robust.

4.1 Two-body collisions

In an integrable system, collisions between two solitons emit no radiation and leave the solitons unchanged except for a phase shift determined by the soliton parameters - in the present case, their velocities. The exact expression for the phase shifts is determined from the asymptotic properties of the corresponding two-soliton solution. Both[9] are given explicitly in [15]. For a collision between two solitons with parameters $\kappa_{1,2}$, the phase shifts read:

$$\Delta\phi_{1,2} = \mp\frac{1}{2\kappa_{1,2}} \ln\left(\beta^2 \frac{(\kappa_1+\kappa_2)^2}{(\lambda_1\kappa_2 - \lambda_2\kappa_1)^2}\right), \tag{74}$$

or, in the GPE language,

$$\Delta\phi_{1,2} = \mp\frac{1}{\sqrt{1-u_{1,2}^2}} \ln\left(\frac{\left(\sqrt{1-u_1^2}+\sqrt{1-u_2^2}\right)^2}{\left(u_1\sqrt{1-u_2^2} - u_2\sqrt{1-u_1^2}\right)^2}\right), \tag{75}$$

where the subscript 1 (2) denotes the slower (faster) soliton. We will also refer to this expression for $\Delta\phi_1$ as $\Delta\phi(u_1, u_2)$ later. This adimensional quantity corresponds to a position shift of $\Delta\phi\,\xi_s$.

Note that the phase shifts are functions of the two soliton velocities separately and not only of their difference, consistently with the lack of Galilean invariance in the dynamical equations. For clarity, we will give results for collisions in which the solitary waves have equal and opposite velocities $\pm u$. In this case, Eq. 75 simplifies to

$$\Delta\phi_{1,2} = \mp\frac{1}{\sqrt{1-u^2}} \ln\left(\frac{1}{u^2}\right).$$

The additional separation after the collision with respect to the unperturbed trajectories, graphed in Fig. 18, is thus

[9] The cited article contains a typo in the expression for the phase shifts: it should contain β^2, as reported here, rather than β.

$$\Delta s \equiv (\Delta\phi_2 - \Delta\phi_1)\xi_s = \frac{2\xi_s}{\sqrt{1-u^2}} \ln\left(\frac{1}{u^2}\right). \tag{76}$$

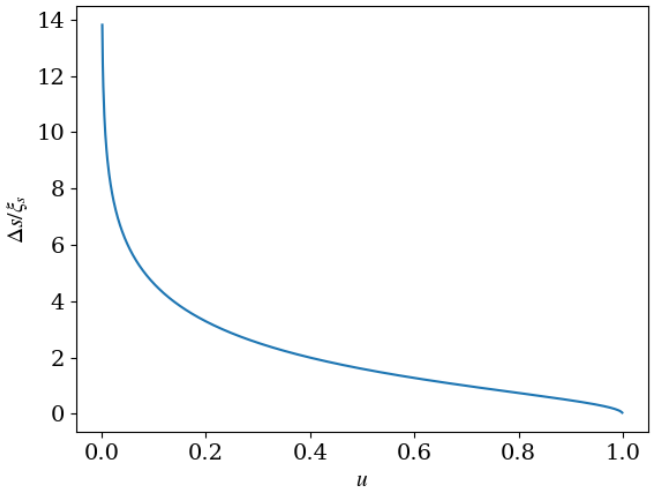

Figure 18: Separation shifts in a collision between two solitons of equal and opposite velocities in the easy-plane Manakov limit, as given by the inverse scattering transform method.

The separation shift is a monotonically decreasing function of u, diverging for $u \to 0$ and vanishing with vertical slope for $u \to 1$. It is also true in Eq. 75 that each soliton's phase shift is a monotonically decreasing function of its velocity at a fixed value of the other soliton's velocity. We may say that the faster a soliton moves, the less it is affected by its interaction with another soliton.

We compare this expression with the results of numerical solutions of the coupled GPEs. In our simulations, we begin by numerically calculating the ground state order parameters of the condensate mixture in a box potential, for a closer approximation of experimentally relevant conditions, which results in almost uniform densities, except at the edges of the system, and vanishing phases. We then multiply these functions by the expression in Eq. 56 to obtain a soliton-like initial state. In the case of multiple solitons, we repeat this procedure at multiple positions, taking advantage of the fact that an exact 2-soliton solution is asymptotically equivalent to the sum of two 1-soliton solutions in the limit of infinite separation between the two objects. Explicitly, the numerical ground state density is used in place of the constant n_0 in the expression $n_{1,2} = (n_0/2)(1 \pm \cos\theta(\zeta - \zeta_0) \pm \sigma \cos\theta(\zeta + \zeta_0))$, where $\cos\theta$ is given by Eq. 56 and $\sigma = \pm 1$, corresponding to soliton pairs of like or opposite z-magnetization. The expression in parentheses is an approximation of a two-soliton state as a sum of single-soliton states, which becomes exact in the limit of large separations $\zeta_0 \to \infty$. Similarly, the phase of the initial state is the sum of the analytical single-soliton solutions centered in $\pm\zeta_0$. An example of an initial state with two solitons is shown in Fig. 19. Note that the lack of dependence of the phase shifts on the sign of the magnetization in the solitons predicted by the preceding expressions is borne out by simulations, so we report results obtained where all solitons have negative magnetization.

This state is not an exact solution of Eq. 13 due to the finite values of g_s and/or δg and the finite size of the system, as well as the finite separation between the solitons. However, for a wide range of parameters,

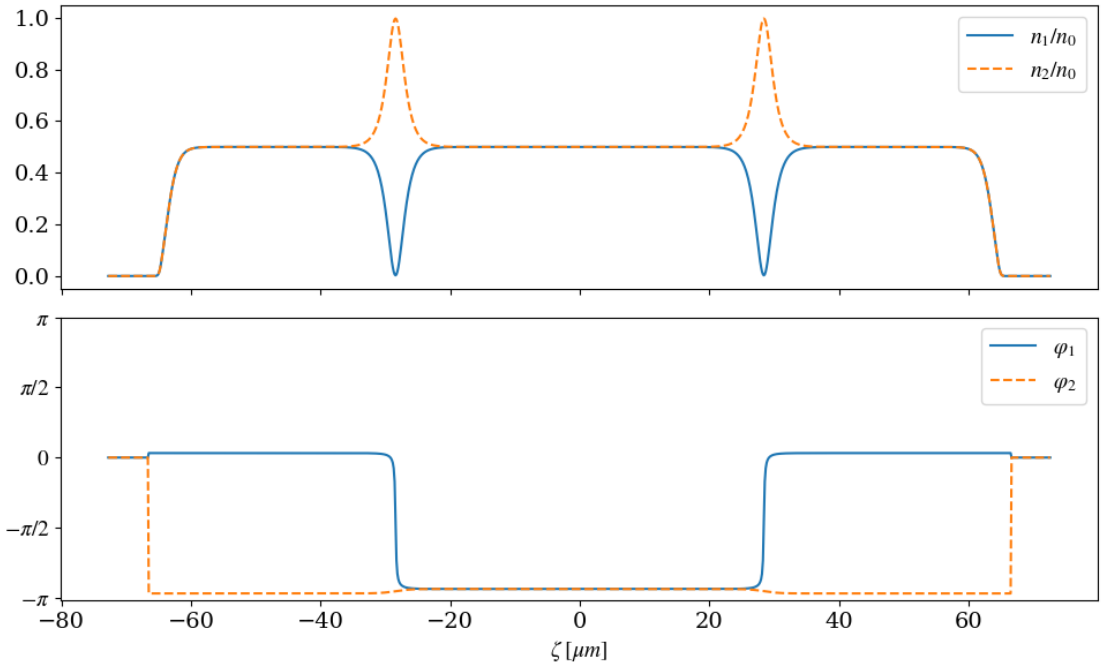

Figure 19: Sample initial state for the simulation of a collision between two solitary waves in the coupled GPEs. The background is obtained through imaginary-time evolution with $g_s/g = 0.005$, $\delta g = 0$, and the solitons are defined with nominal initial velocities $\pm 0.1 c_s$, with $c_s = 1.2$ mm/s.

this procedure is observed to result in an evolution in which two well-defined objects move at constant velocities and collide, retaining their individual characteristics after the collision. Although these objects are not solitons in the strict sense, since they exist in a non-integrable system, the situation may be conceptualized as an initial structure which is relatively close to a stationary state (up to a change of reference frame) of the system, which when allowed to evolve according to the coupled GPEs emits some radiation in addition to a solitary wave with a well-defined velocity (which may not match the nominal velocity u that appears in the functional form of the initial state). When two solitary waves created in this way collide, they remain distinct, and we can measure their phase shifts as the difference between the position of the minimum of the magnetization at some final time (when the wave is far away both from the other wave and from the system's edges) and the position it would have reached by traveling at the constant velocity observed in its initial motion. We illustrate a few collision dynamics in Fig. 20 and display results for the phase shifts in Fig 21.

As expected, we find that the numerically computed separation shifts are in excellent agreement with the exact results for the integrable theory for the smallest values of g_s/g we ran simulations with. However, we also find that the same prediction, scaled to the appropriate value of the spin healing length, works remarkably well for fairly large values of g_s/g. For a miscible mixture one has $|g_s|/g \in (0, 1]$ (where $g_s/g = 1$ is achieved in the decoupled case $g_{12} = 0$), yet in the case $|g_s|/g = 0.5$, the IST prediction captures the observed behavior reasonably well, and even at $|g_s|/g = 0.9$ it gives the order of magnitude of the separation

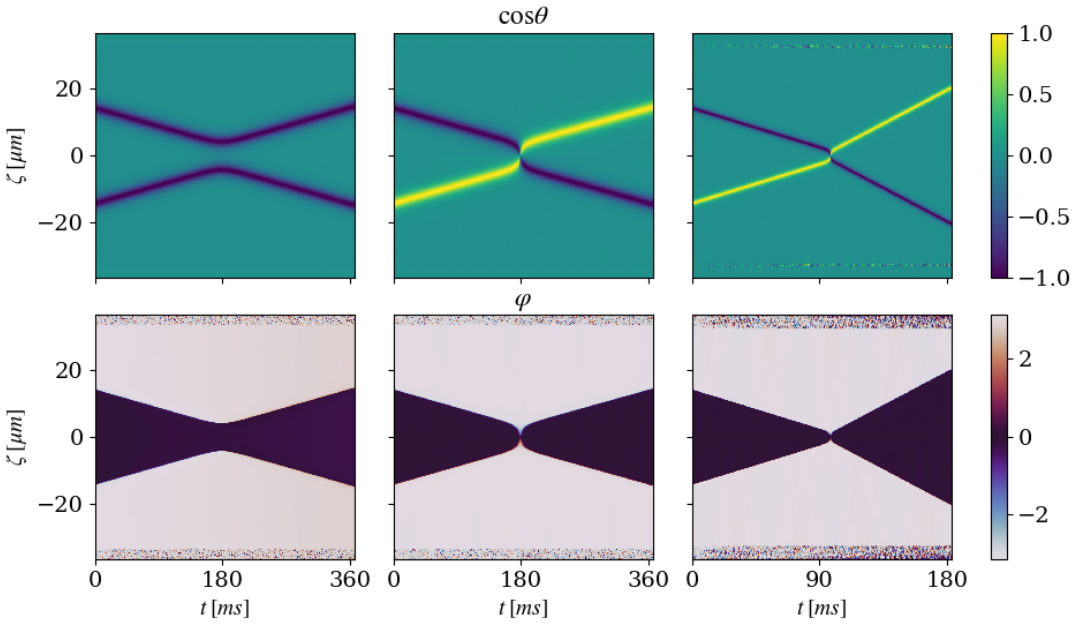

Figure 20: Relative density and phase during sample solitary wave collision simulations. The third column reports a simulation in which a higher value of $g_s/g = 0.05$ causes the collision to be noticeably inelastic, (in the first two columns, $g_s/g = 0.01$).

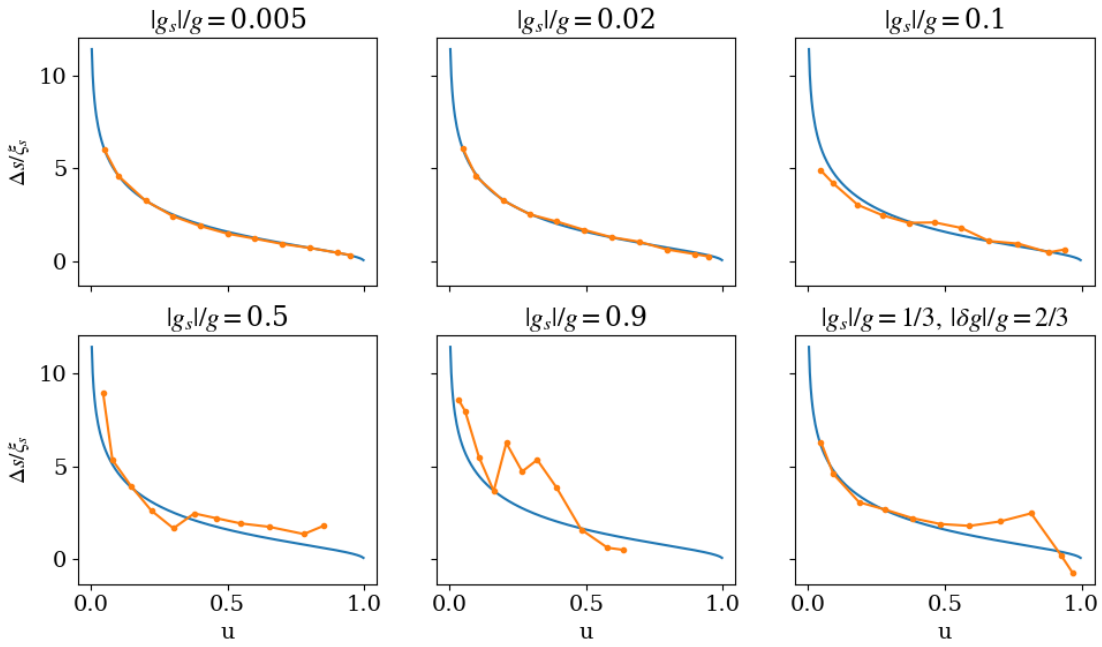

Figure 21: Observed separation shifts in collisions between two solitary waves in GPE simulations (points) compared to the analytical result Eq. 76 given by the IST method for the Landau-Lifshitz equation (lines) for different values of the interaction constants g_{ij}. Here the two waves have equal and opposite velocities $\pm u$, and correspondingly undergo equal and opposite phase shifts $\pm\Delta s$. Increasing values of g_s and δg bring the system further away from integrability and correspondingly larger deviations from the IST prediction are observed. Where not specified, $\delta g = 0$.

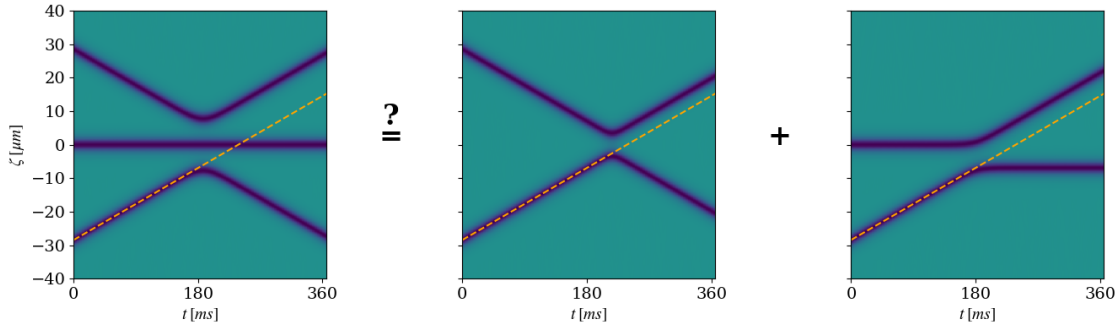

Figure 22: To investigate whether solitary waves away from the integrable limit exhibit three-body interactions, we compare simulations of collisions involving three such objects with simulations of pairwise collisions. If only two-body interactions occur, one expects the phase shift of the fastest solitary wave in the three-way collision to be the sum of those it experiences in two-way collisions with each of the other waves involved.

shifts accurately. The same is true even when we break the mixture's $\mathbb{Z}_2$ symmetry by including a non-zero δg, introducing a further qualitative difference with respect to the strictly integrable case. The further away from the Manakov limit we go, the more radiation we see emitted at the beginning of a numerical evolution by the initial object, but the solitary wave that is left behind and its soliton-like behavior persist. We characterize this observation as an unexpected robustness of such solitary waves' quasiparticle nature, in the sense that they can be thought of as singular objects with definite properties which they retain after interacting with each other.

4.2 Three-body collisions

In addition to their simple behavior in two-way collisions, solitons are characterized by the fact that they are subject only to two-body interactions. In particular, the phase shifts resulting from an interaction involving any number of solitons are simply the sums of those that would result from separate pairwise collisions. It is interesting to investigate whether the breaking of integrability in the coupled GPEs leads to deviations from this behavior, separately from any deviations in the phase shifts themselves from their Manakov-limit values. To do so, we perform simulations of collisions between three solitons, where all three are close to each other simultaneously. In a collision between solitons of velocities $u_1,\ u_2,\ u_3$, the integrable prediction for the phase shift of the first soliton is $\Delta\phi_1 = \Delta\phi(u_1, u_2) + \Delta\phi(u_1, u_3)$. We compare our numerical results to the analytical value of this quantity, but deviations from it could be attributable to a change in the value of the two-body phase shifts. To separate out this effect, we compare the observed phase shifts in a simulation of a three-way collision to those observed in simulations of two-way collisions between the respective pairs of solitons involved (see Fig. 22). In this way, we specifically study the deviation of this aspect of solitary wave interaction from the behavior expected assuming only pairwise interactions occur.

We report results for the case where the sign of the magnetization is the same in all three solitary waves and where two of them have equal and opposite velocities $\pm u$ and the third one is stationary. However, varying these conditions does not lead to a qualitative difference in the conclusions. With this simplification, the soliton traveling at $+u$ accrues, in the integrable theory, the phase shift

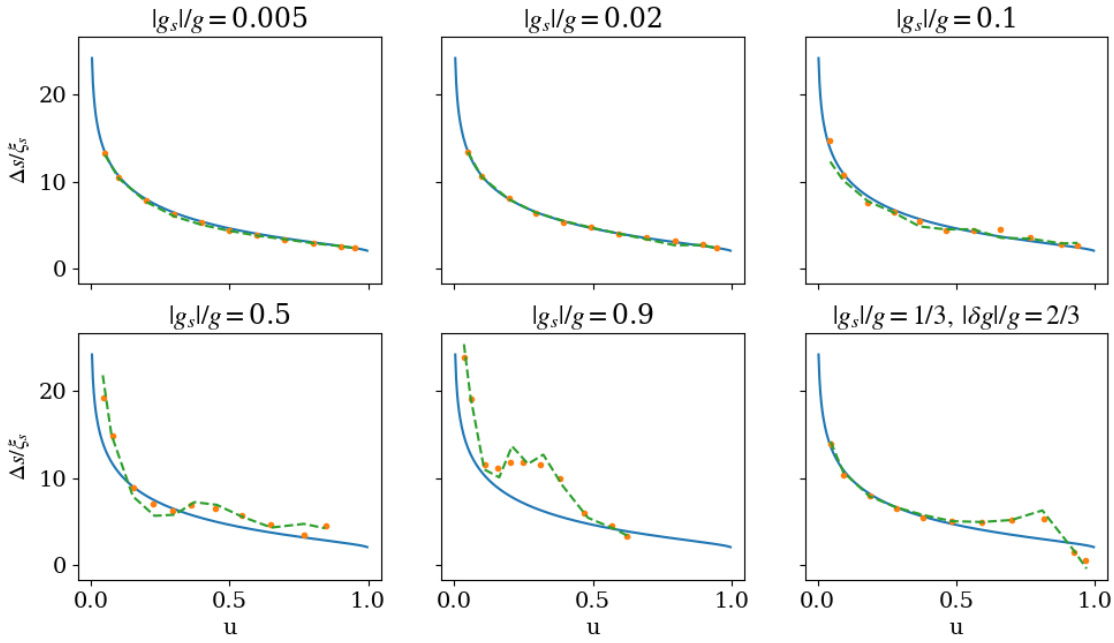

Figure 23: Observed shifts in collisions between three solitary waves in GPE simulations (points) compared to the analytical result Eq. 75 given by the IST method for the Landau-Lifshitz equation (solid lines) and to the sums of the shifts observed in the corresponding pairwise collisions (dashed lines) for different values of the interaction constants g_{ij}. Two of the waves have equal and opposite velocities $\pm u$, while the third is stationary. The phase shift of the wave traveling at $+u$ is recorded. The three-body shifts closely match the summed two-body shifts in all observed cases, even very far from integrability and when the IST does not accurately predict the observed shifts.

$$\Delta\phi_1 = \Delta\phi(u,0) + \Delta\phi(u,-u) = \frac{2}{\sqrt{1-u^2}} \ln\left(\frac{1+\sqrt{1-u^2}}{u^2}\right). \tag{77}$$

This function has similar properties to that in Eq. 76, but its limit for $u \to 1$ is 2 rather than 0. This finite limit is due to the presence of the stationary soliton. Figure 23 compares the results of simulations of three solitary waves both with this analytical expression and with the sum of the shifts observed in simulations of two solitary waves.

We could find no appreciable deviation from the two-body nature of solitary wave interaction. This negative result provides further evidence of behavior similar to that found at integrability in wide ranges of the parameter space of the coupled GPEs, and of the robustness of their solitary waves as quasiparticles.

4.3 Solitons impinging on sharp density gradients

In this section, we discuss another instance of solitary wave behavior in a miscible mixture in circumstances of broken integrability. The integrability-breaking element we introduce here is that of a non-constant total

density: in particular, we consider two regions of different uniform densities, connected by a sharp step (see Fig. 24). We are interested in the behavior of a solitary wave which propagates towards the interface. Moti-

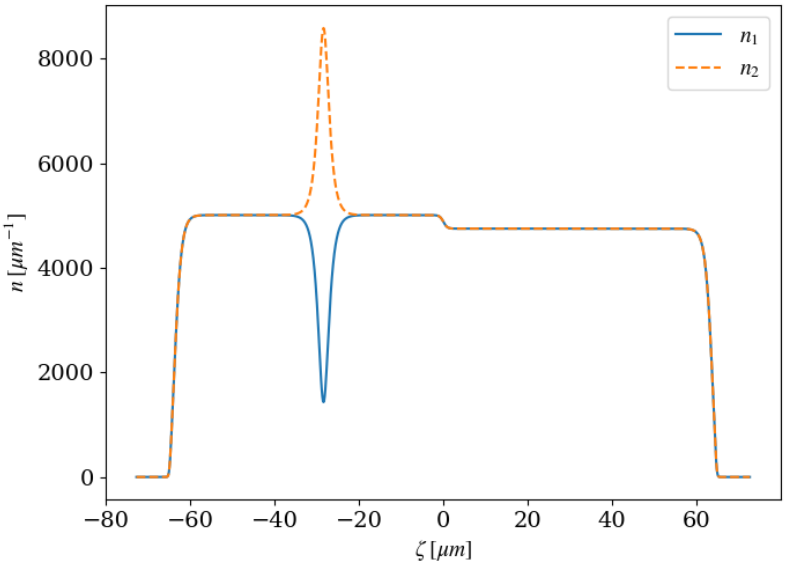

Figure 24: Example of the initial state in a simulation where a soliton defined in the left region propagates towards a density step. Here $n_R/n_L = 0.948$.

vated by the indications of the robustness of the soliton-like properties of solitary waves in the non-integrable coupled GPEs, we devote our attention to the question of whether a solitary wave impinging on such an interface can be satisfactorily described as a quasiparticle whose trajectory is determined by its dispersion relation. If this is the case, the problem of transmission and reflection of the solitary wave can be formulated with a simple energy-conservation argument, leading to the expectation that either complete reflection or complete transmission of the wave will occur, depending on its initial energy. If not, it is conceivable that partial transmission may occur, with a split into a reflected solitary wave and a transmitted one. This case, in which the quasiparticle picture fails, would require a treatment based on the decomposition of the solitary wave into the elementary excitations of the system. The behavior of such excitations at an interface has the notable property that their reflection coefficient does not approach unity at low energies, leaving a residual transmission in this limit (see [72] and references therein). This does not automatically imply that the same is true of a soliton in the same system, as a consequence of the non-trivial nature of the decomposition of a nonlinear excitation into the elementary modes. To investigate these alternatives, we first find a prediction for the transmission properties of solitary waves in the quasiparticle picture, then compare it to the results of numerical simulations.

The two regions (left and right) which the system is divided into differ in their characteristic length and time scales because of their differing densities n_L and n_R, but they are qualitatively equivalent. In particular, both regions admit the same families of solitary wave solutions, whose properties depend parametrically on the background density. If we take for granted that a solitary wave, which for concreteness we take to travel in the positive ζ direction starting in the region to the left of the interface, evolves in this system as a quasiparticle, it follows from conservation of energy that it will be transmitted across the interface only if there

exists a solitary wave state in the same family and with the same energy as the initial wave's. Momentum is not conserved because the system is inhomogeneous. We will describe these solitary waves using the results for the single-parameter family of easy-plane soliton solutions described in section 2.5, for which we have an explicit expression for their energy as a function of their velocity. In this approximation, the condition for energy conservation during transmission through the barrier at an outgoing velocity v_{out} of a solitary wave with incoming velocity v_{in} is

$$E_L = E_R \iff n_L \hbar c_L \sqrt{1 - \frac{v_{\text{in}}^2}{c_L^2}} = n_R \hbar c_R \sqrt{1 - \frac{v_{\text{out}}^2}{c_R^2}}, \tag{78}$$

where c_L and c_R are the spin speeds of sound in the left and right region, respectively. The maximum energy is achieved by the stationary soliton, which has the energy $E_{L,R}(v_{L,R} = 0) = n_{L,R}\hbar c_{L,R}$. Therefore, our quasiparticle approach predicts that transmission takes place at any initial velocity v_{in} when $n_R \geq n_L$. We will proceed under the assumption that $n_R < n_L$, which we expect to be the more interesting case admitting both reflection and transmission. Solving the energy conservation condition for the outgoing velocity in terms of the incoming velocity yields

$$\frac{v_{\text{out}}}{c_R} = \sqrt{1 - \left(\frac{n_L}{n_R}\right)^3 \left(1 - \frac{v_{\text{in}}^2}{c_L^2}\right)}, \tag{79}$$

where we have used the fact that $c_{L,R} = \sqrt{|g_s| n_{L,R}/2m}$. This expression is imaginary for incoming velocities below the critical value

$$\frac{v_0}{c_L} = \sqrt{1 - \left(\frac{n_R}{n_L}\right)^2}, \tag{80}$$

which is the minimum incoming velocity for which states with $E_R = E_L$ exist, that is, the velocity for which the incoming soliton has an energy equal to the maximum energy of the soliton states in the region to the right of the interface. Of course, v_0 is defined only for $n_R \leq n_L$. The case $v_{\text{in}} = v_0$ is of special interest, since if the quasiparticle picture holds, a soliton impinging on the interface at v_0 should excite a stationary soliton of the right region located at the interface. For $v_{\text{in}} < v_0$, our argument predicts reflection of the solitary wave at velocity $-v_{\text{in}}$. At the other extreme, the soliton energy approaches zero as its speed approaches the spin speed of sound for any value of the density, so that we always have $v_{\text{out}}(v_{\text{in}} \to c_L) = c_R$. The expected outgoing velocities are visualized in Fig. 25.

We compare the prediction of the quasiparticle picture with numerical simulations. Our procedure is similar to that described previously: first, we obtain a ground state (using imaginary-time evolution) for equal potentials $V_{\text{ext},1} = V_{\text{ext},2}$ where we add a sharp step at $\zeta = 0$ to the box potential. We then use the expression in Eq. 56 to create a soliton in the uniform region at negative ζ, obtaining an initial state like that in Fig. 24. After simulating its evolution, we measure the solitary wave's velocity both before and after it has been reflected or transmitted by the interface, at a position where it is far away from both the interface and the system's edges. We repeat this at various values of the initial velocity, and for several values of $n_R/n_L < 1$, while we take $g_s/g = 0.01$ and $\delta g = 0$ throughout. Qualitatively, we observe that the solitary waves remain well-defined in every simulation we performed. Some sample trajectories are shown in Fig. 26.

The outgoing velocities as well as the critical velocity for transmission are well predicted by the expressions we obtained from the energy-conservation argument, as can be seen in Fig. 27. This is true even for

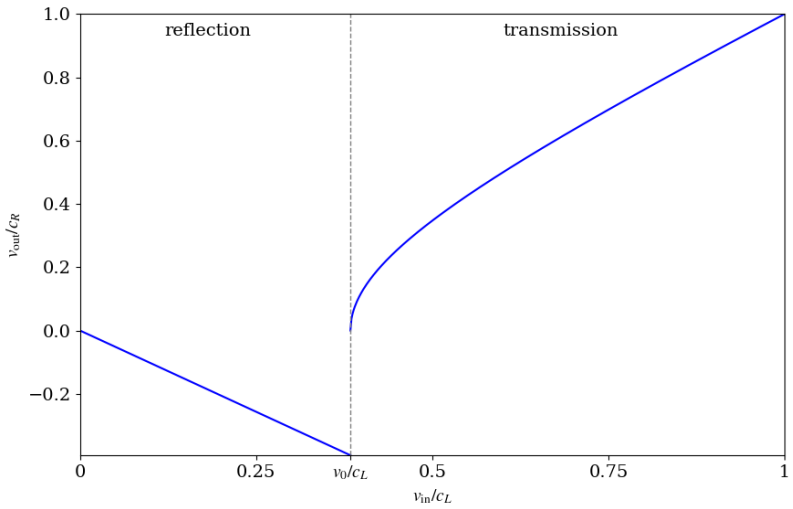

Figure 25: Prediction of the quasiparticle picture for the outgoing velocity of a soliton impinging on a density step as a function of its incoming velocity. At velocities less than the critical value v_0, perfect reflection is predicted. This plot is for $n_R/n_L = 0.948$.

the most extreme density ratios we tested. It is not obvious that this should be true when the density drops by over half, an amount comparable to or greater than the amplitude of the impinging solitary wave, in the second case illustrated in the figures, and over a much smaller distance than the typical size of the waves at higher velocities - in fact, tweaking the width of the density step between that set by the interaction strengths (the density healing length, which is a factor 10 smaller than the spin healing length) and a scale several times the healing length did not significantly affect our results for the outgoing velocities. We consider this a further indication of the robustness of the quasiparticle-like behavior of the solitary waves we are studying, in the sense that the properties of the solitons they are related to can be applied to effectively describe their behavior in conditions of broken integrability.

Several features of the simulated evolutions merit further attention. One is the emission of radiation at the interface between the two regions. As is visible in Fig. 26 and Fig. 28, the transmission of a solitary wave is associated with the emission of radiation in both directions, with the effect becoming more noticeable at smaller values of n_R/n_L. This is an inevitable feature of transmission within the quasiparticle picture, since the number of particles in a soliton in the left-hand or right-hand system is $N_{L,R} = \pi n_{L,R}\xi_{L,R}$, independent of its energy, where $\xi_{L,R}$ are the respective spin healing lengths. Thus, if transmission takes place, we expect a number

$$N_L - N_R = -\pi(n_L\xi_L - n_R\xi_R) = -\frac{\pi\hbar}{\sqrt{2mg_s}}\left(\sqrt{n_L} - \sqrt{n_R}\right) \tag{81}$$

of particles to be radiated away from the solitary wave, where the minus sign accounts for the negative z-magnetization in the waves. We measure this quantity in our simulations by integrating the z-magnetization in the vicinity of the solitary wave after the radiation has traveled as far away as possible, and find that it matches the above expression to within 2% in all cases. This strengthens the interpretation of the transmission event as one in which the outgoing wave has the same properties as the incoming one, and that these are essentially

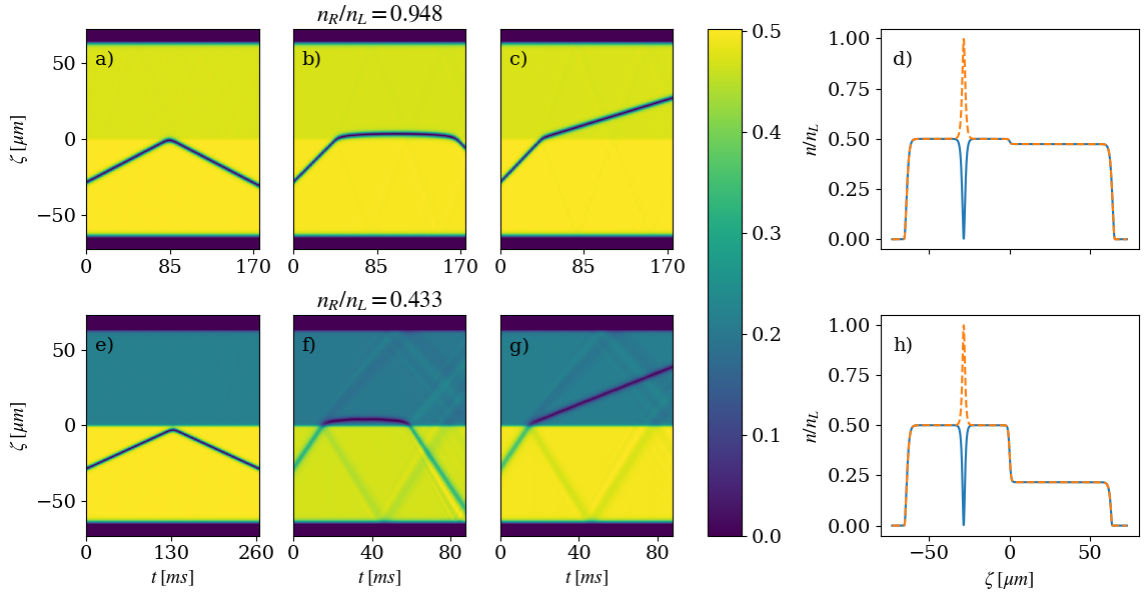

Figure 26: Some numerical evolutions of solitary waves impinging on a density step at the largest (panels a through d) and smallest (panels e through h) values of n_R/n_L we used. The color plots show the minority component density n_1/n_L as a function of position and time. Panels a and e refer to evolutions where the initial velocity is significantly below the theoretical critical value for transmission, panels c and g to velocities above v_0, and in panels b and f, the velocity entering the functional form of the soliton is chosen equal to the critical value. In practice, the actual velocity is close to but slightly lower than v_0. Panels d and h illustrate sample initial states for the two values of n_R/n_L, with n_1/n_L as the solid line and n_2/n_L as the dashed line.

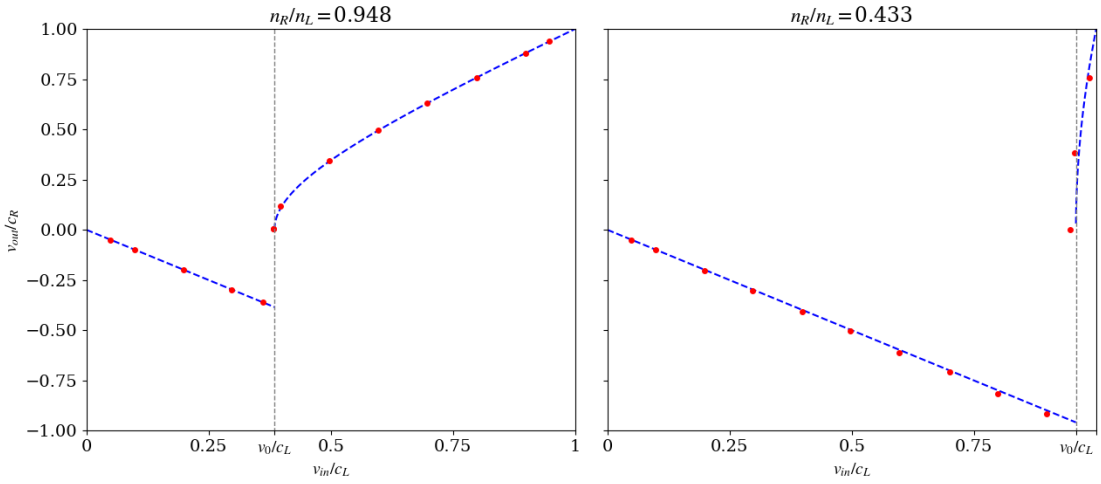

Figure 27: Comparison between the outgoing velocities observed in simulations (points) and the prediction of the quasiparticle picture (dashed lines) for two different values of n_R/n_L.

those of the easy-plane magnetic solitons. Indeed, Eq. 81 is fulfilled if the dependence of the energy of both the incoming and outgoing solitary wave on their velocities is given by the solitonic expression used above.

As shown in Fig. 28, radiation is also observed after reflection, and is much stronger at higher velocities and lower n_L/n_R. Emission is to be expected for a solitary wave being accelerated by an external force, as its energy changes during acceleration and the rest of the system must compensate to keep the total energy constant. This is, at least in part, a different phenomenon from the radiation that is produced during transmission. Indeed, the total magnetization carried by the radiation after a reflection is always close to zero, whereas it is sizeable in the case of a transmission, in connection to the change in the solitary wave profile. This is consistent with the fact that the reflected solitary wave is nearly identical to the incoming one, with reflection taking place nearly elastically (though not perfectly so - some energy is lost by the solitary wave to radiation, as is visible in Fig. 27 in the fact that $(v_{\text{out}}/c_R)^2 > (v_{\text{in}}/c_L)^2$ at high v_{in}/c_L). Rather than the solitary wave decomposing into more than one solitary wave and a certain amount of radiation, it retains its identity and excites a spin wave packet during its interaction with the sharp interface. This mechanism is closely connected to the fact that the density at the interface varies rapidly with respect to the solitary wave width, taking the system out of the regime in which the adiabatic approximation should be expected to hold. The adiabatic scenario was studied in reference [73].

For both solitary wave transmission and reflection, the emitted excitations are similar to packets of spin waves whose group velocity is around the spin speed of sound in the region where they are propagating, with the most evident difference between the two cases being the much higher energy and total z-magnetization carried by the radiation produced during solitary wave transmission. A more precise understanding of this emission remains as a question for future research.

The other feature of special interest is the behavior of the solitary wave at incoming velocities very close to the critical value v_0. Although it is not possible to achieve the exact condition $v_{\text{in}} = v_0$, values just below it exhibit the peculiar behavior shown in panels b and f of Fig. 26. In the quasi-particle picture, the expectation is for a stationary solitary wave of the right-hand region to be excited at the interface. This is

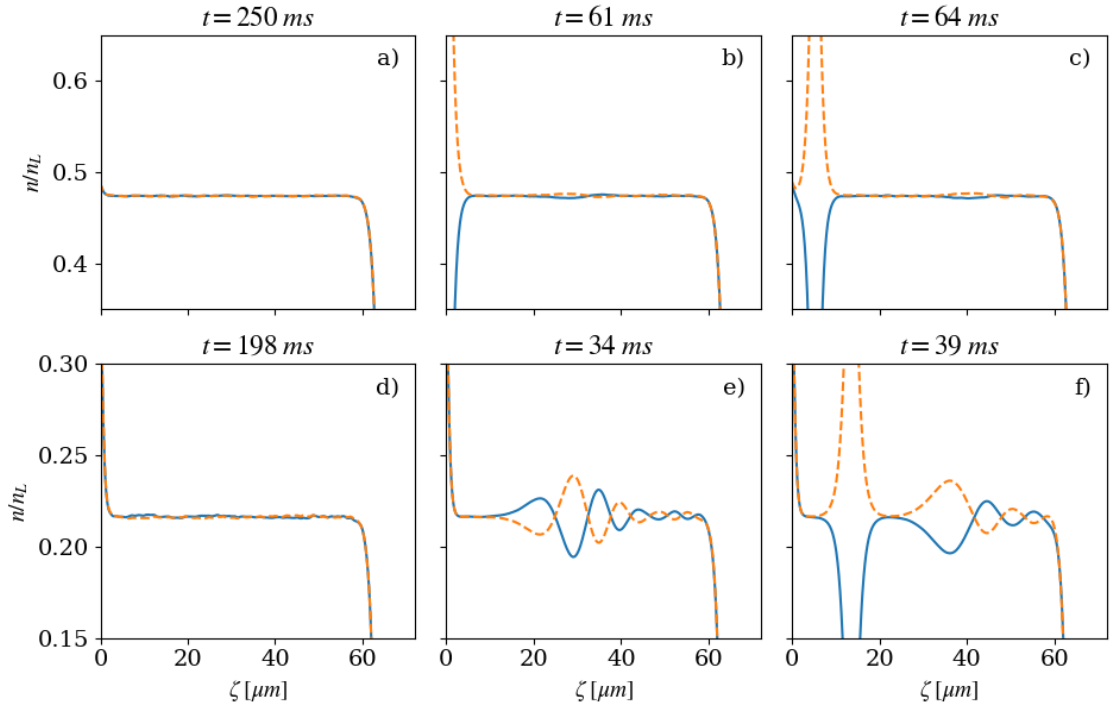

Figure 28: Condensate densities in the right half of the system after the solitary wave reaches the density step for different values of density ratio and incoming velocity. In panels a through c, $n_R/n_L = 0.948$, while in panels d through f, $n_R/n_L = 0.433$. Panels a and d show the system after reflection of a wave with an incoming velocity $v_{\rm in}/c_L = 0.1$, significantly below the crtical value v_0. Panels b and e show it after reflection of an incoming wave with $v_{\rm in} = 0.95 v_0$. Panels c and f portray the system after transmission of the incoming wave. The situation for $v_{\rm in} \approx v_0$ (as in panels b and f of Fig. 26) is very similar to the transmitted case. Similar excitations are emitted into the left half of the system in all cases. Solid lines give n_1/n_L and dashed lines give n_2/n_L.

broadly consistent with what is seen in our simulations, although it is ambiguous whether our observations should be interpreted in this way. Indeed, a quasi-stationary wave is seen, but it exists only for a finite amount of time before turning into a reflected wave, an event accompanied by a second emission of radiation. The presence of two radiation events, which carry a non-zero magnetization, can be seen as an indication that the dynamics may be interpreted as a first transmission exciting a stationary wave in the right-hand region, followed by a second transmission back into the left-hand region. However, in part due to the inevitably finite width of the density step (in combination with the fact that the solitary waves themselves are not pointlike), this situation is approached continuously: as v_{in} approaches v_0, the velocity of the solitary wave varies more and more gradually during reflection, which becomes less and less similar to an instantaneous reversal in the trajectory. Notably, we never observed a case in which a quasi-stationary wave was excited and then gave rise to a transmitted wave propagating in the right-hand region. It is likely that this scenario should be understood by characterizing the interaction of the solitary wave with the density step and their possible bound states, another question for future research.

In conclusion, the quasiparticle approach based on a simple energy-conservation argument is adequate in its prediction of the outgoing velocities of reflected and transmitted solitary waves and of the value of the critical incoming velocity separating the two cases. In the cases we examined, it was never made inapplicable by the destruction of the solitary waves. However, this approach makes no attempt to describe the production of other linear or nonlinear excitations of the system during its evolution. In both cases, the validity of the quasiparticle picture actually implies the emission of radiation, yet we do not have a detailed account of the emission mechanism, nor of the process whereby the accuracy of the predictions of a model that ignores it is preserved.

5 Preliminary results and outlook

In this chapter, we present interesting phenomena observed during simulations for which we have not yet developed a convincing theoretical treatment. Elucidating the mechanisms behind these observations may be of interest as a direction for future research. We present two categories of simulated evolutions, each of which exhibits behavior that differs from that of the solitonic solutions discussed previously, although in both cases the system remains close to the regime of constant total density throughout its evolution, making it possible to apply the mapping to the LLE. The two categories are distinguished by the different integrability-breaking elements at play. In the first case, these are only the finite value of g_s, the discretization of the system, and its finite size, which were present in the previous sections but now are likely identifiable as sources of qualitative deviations from integrable behavior. In the second case, integrability is also broken by the presence of coherent coupling between the condensates, a feature which alters the physics of the mixture at a fundamental level even for weak values of the coupling.

5.1 Soliton bound states

The first behavior we present is the formation, highly sensitive to the choice of initial conditions, of what we will refer to as soliton bound states of finite lifetime in the mean-field coupled miscible mixture. The initial state of the system is obtained in much the same way as the initial states of the two-soliton collisions studied in chapter 4, as the sum of two single-soliton solutions, except that the positions of the solitons are chosen so that they cannot be considered well-separated, as illustrated in Fig. 29. Unlike the well-separated states studied previously, this differs considerably from a two-soliton solution (including at times when the two objects in such a solution are close together), so we cannot expect to observe simple solitonic collisional behavior. Indeed, if we conceptualize the evolution as that of two distinct solitary waves, the interactions between the two are important already in the initial state and cannot be reduced to the emergence of asymptotic phase shifts. When the z-magnetization in the two waves is of the same sign, the interaction is repulsive, so that a bound state does not form and the evolution is like that in panel a of Fig. 32. In the opposite case, the interaction is attractive, and the two waves form a bound state, oscillating about a common center for a variable number of periods before the bound state breaks and the two propagate away from each other at constant velocities. A few examples of the phenomenon are illustrated in Fig. 30. Bound state formation is observed at small initial separations and velocities. For vanishing initial velocities, it is seen at considerably larger initial separations than at small finite velocities. The duration of the bound state and the outgoing velocities after it breaks are highly sensitive to these initial parameters. Some amount of radiation is emitted during the oscillations, though radiation is more prevalent when the initial state is highly overlapping or when g_s is larger; see Fig. 31. Bound states of finite lifetime are seen even for small values of g_s/g and $\delta g/g$, including those at which excellent agreement was found between the integrable prediction for the values of the phase shifts and those observed numerically. Accordingly, the total density is nearly (within 2%, a similar deviation to that observed in the simulations used to calculate the phase shifts) uniform and constant, so that we expect the system to be well-described by the LLE. Since no external fields are present, except those confining the system to a finite size, this suggests that the bound state dynamics are describable within an integrable theory. However, as we will see, there are indications to the contrary, despite the weakness of the deviation from integrability.

The observed dynamics are closely reminiscent of phenomena that have long been studied in the literature, under the name of soliton bound states or soliton molecules, and such research provides several possibilities to investigate in attempting to explain our observations.

It was shown through the inverse scattering method in [18] that the self-focusing NLSE (equivalent to the

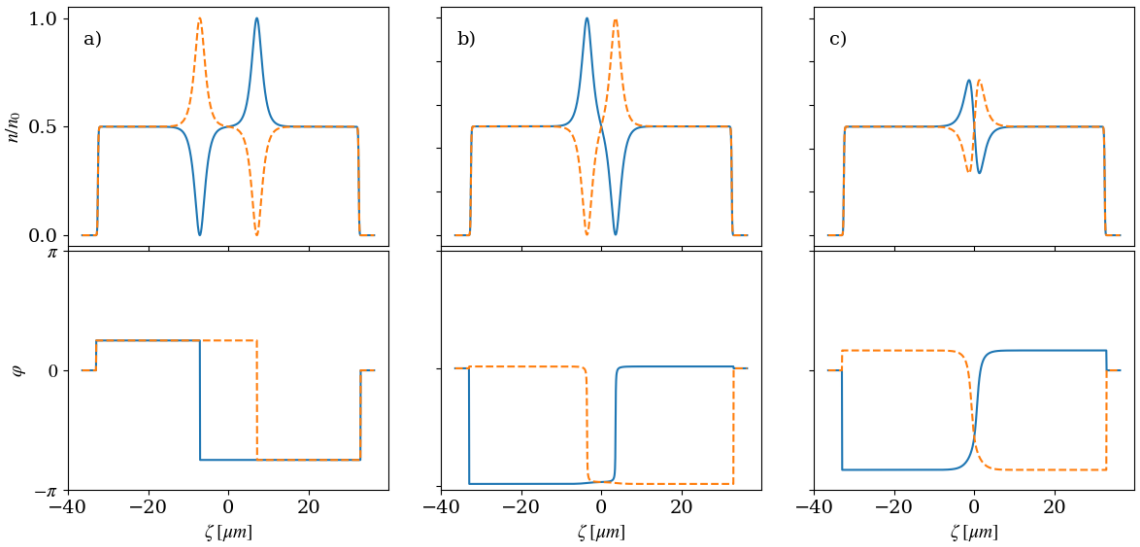

Figure 29: Sample initial states used in the simulations reported in this section. Solid lines give the density and phase of component 1, and dashed lines those of component 2. Panel a is obtained by imprinting two stationary magnetic solitons on the box-trap miscible ground state, and is the initial state of the evolution in panel b of Fig. 30. Panel b shows two solitons with finite initial velocities $v = \pm 0.05 c_s$ and a smaller separation, and corresponds to panel d of Fig. 30. Panel c displays solitons with velocities $v = \pm 0.5 c_s$ and very small separation, and the corresponding evolution is shown in panel a of Fig. 31.

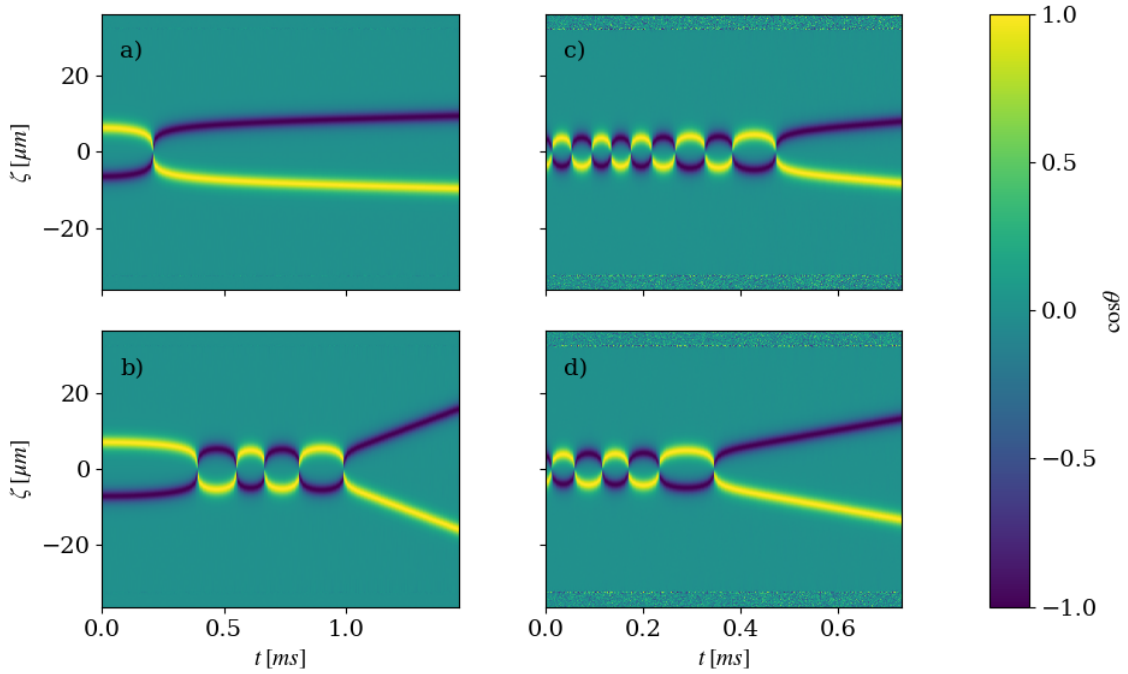

Figure 30: Numerical evolutions in or near conditions of short-lived solitary wave bound state formation in the miscible mixture at $g_s/g = -0.01$. In panels a and b, the initial state is defined by imprinting two stationary magnetic solitons close enough for their attractive interaction to result in a collision. The initial separation is 12.8 μm in panel a and 14.2 μm in panel b (see also panel a of Fig. 29. In panels c and d, the initial state is the sum of two magnetic solitons of equal and opposite velocities at a separation of 7.1 μm. The velocities are $v = \pm 0.04 c_s$ in panel c and $v = \pm 0.05 c_s$ in panel d. In all cases, the spin healing length is $\xi_s = 1.13$ μm. These examples demonstrate the sensitivity of bound state formation and lifetime and of the outgoing velocities to the initial conditions, as well as the non-periodic nature of the oscillations.

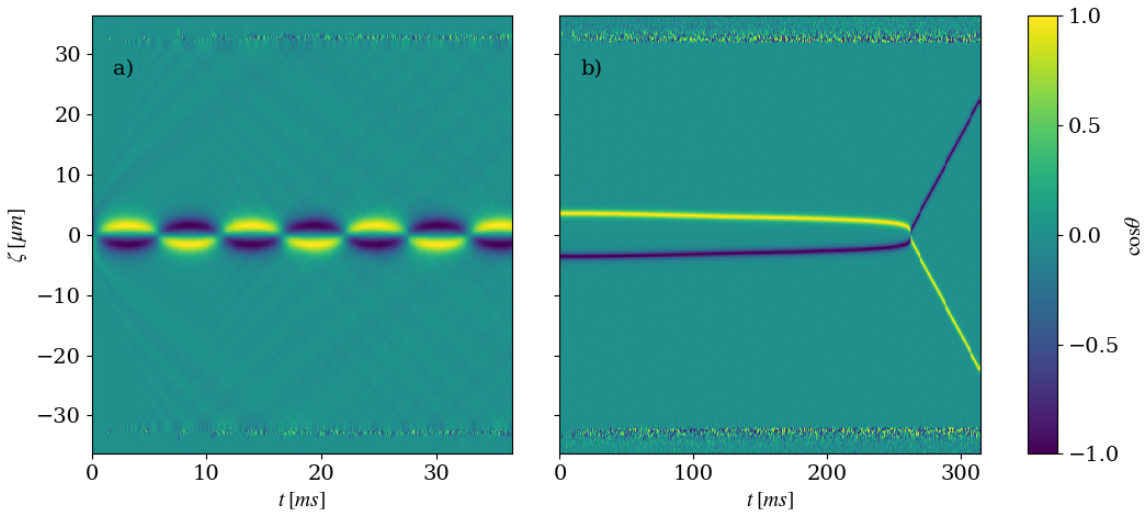

Figure 31: In panel a, the evolution of an initial state defined by two highly overlapping magnetic solitons at $g_s/g = -0.01$ (see panel c of Fig. 29). Their separation is 1.42 μm for a healing length of $\xi_s = 1.13$ μm, and their initial velocities are $v = \pm 0.5 c_s$. A considerable amount of radiation is emitted at the beginning of the evolution, since the initial state is far from a solitonic state, but the bound state that is formed seems quite stable - we show only the first few oscillations for clarity, but the simulation was carried out up to 732 ms, in which time 140 oscillations occur without noticeable changes, even in the presence of radiation. It is likely that this case is describable as the excitation of a state close to a multi-parameter soliton of the integrable limit. In panel b, an initial state composed of two stationary magnetic solitons at a separation of 7.11 μm results in a highly inelastic collision. Here $g_s/g = -0.1$ and $\xi_s = 0.36$ μm. The larger value of g_s means an appreciable amount of radiation is emitted at the beginning of the evolution, although it is not visible in this plot. Emission also occurs (with varying intensity according to the initial separation) at the collision event. At this value of g_s, bound state formation is observed at correspondingly smaller initial separations. In this regime, one may expect, if such mechanisms are present, resonant energy transfer and radiative processes to be more significant than when g_s is smaller, and radiationless energy exchange less so. Inelasticity in collisions without bound state formation is also observed at smaller g_s, but less frequently and less dramatically.

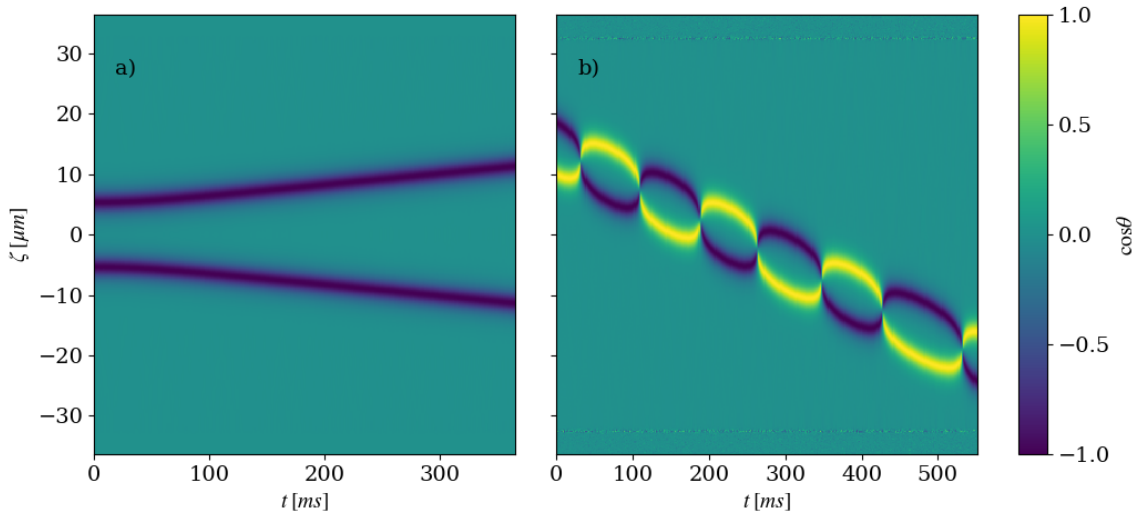

Figure 32: Panel a shows the evolution of an initial state defined by two stationary magnetic solitons of the same sign. In this case, the two objects interact repulsively and bound state formation is never observed. Panel b demonstrates that bound states can form with a non-zero center-of-mass velocity.

attractive GPE) admits bound states of N bright solitons of different amplitudes, which are periodic solutions for $N = 2$. In [74], an interaction potential between two bright solitons was derived as a function of their separation and their phase difference, as had already been achieved in [75], and the formation of bound states was predicted between solitons with finite relative velocity. The authors report that a bound state will always form if the solitons are in phase and their positions and velocities are small enough for the kinetic energy of their relative motion not to exceed their potential energy.

Such bound states are unstable ([76]), since small perturbations can change the soliton velocities. The behavior we observe may be analogous: in our simulations, too, small separations and velocities favor bound state formation, with the distinction that the presence of solitons with amplitudes of either sign meaning that bound states are allowed between solitons whose amplitudes have the same absolute value. In this case, the eventual breaking of the bound state may be due to the presence of radiation, which is emitted by the non-solitonic initial state, or possibly to finite-size effects. However, the bound state oscillations we observe are, at least in some cases, noticeably non-periodic (as in Fig. 30), suggesting a different origin for the bound states.

A system closer to ours was considered in [77] and [78], where bright solitary waves in the (non-integrable) coupled self-focusing NLSE (equivalent to the coupled GPEs with negative interaction constants) are studied, under the name of vector solitons. In addition to the sign of the nonlinearity, these differ from magnetic solitons in that a vector soliton consists of a bright-soliton-like object in one component, while the other component is constant. Pairs of such vector solitons (one in either component) are shown to undergo complicated internal oscillations whose effects include oscillations of the two objects about their common center, with the emission of radiation taking energy away from the pair.

It is also possible that the phenomenon we observe is a consequence of the breaking of integrability in our system, due to the finite value of g_s/g, the finite system size, and the discretization of the system. That these elements, however weak, are crucial to understanding the observations in question is suggested by

the fact that the bound states are seen to break after some time. The formation of bound states with finite lifetimes has been extensively studied in the literature dealing with solitary waves in non-integrable systems (see references [79, 80, 81, 82, 83, 84, 85, 86, 87]).

In this context, several mechanisms responsible for the formation and eventual breaking of the bound states have been identified. One is the phenomenon of resonant energy transfer (see, e.g., [81]), which is due to an exchange between translational energy and internal energy of the solitary waves. During collision, some of their kinetic energy may be transferred to excite a (discrete) internal oscillation mode of the waves. This results in an inelastic collision and may be sufficient to form a bound state. The energy can be transferred back into the translational mode during a subsequent collision if the phase of the internal mode and the translational motion are tuned appropriately, that is, if the collision takes place close to a whole number of periods of the internal mode. The sensitivity of energy transfer to this tuning is reflected in a chaotic structure, which, however, is a more general occurrence than the mechanism of resonant energy transfer.

A characteristic feature of collisions in non-integrable systems is the presence of fractal structures in the velocities of the outgoing solitary waves resulting from the breaking of a bound state. In a typical scenario where the incoming velocities are equal and opposite, there is some critical velocity above which the collision never results in capture into a bound state (viewing this simple scattering event as a reflection, the waves are said to undergo a single bounce). However, not all velocities below the critical value result in a bound state. Rather, there exist windows below the critical velocity within which the waves are captured, undergo two bounces, then escape. Furthermore, in the vicinity of these two-bounce windows are narrower three-bounce windows, in the vicinity of which are four-bounce windows, and so on. Thus, if the ingoing velocity is varied gradually within the region where bound states form, the resulting dynamics vary rapidly and unpredictably. This structure is a widespread feature of non-integrable systems, and is always present in quasi-integrable ones, however weak the integrability-breaking perturbation is. It is not a specific feature of the function $v_{\mathrm{out}}(v_{\mathrm{in}})$, having also been found in the behavior of the final velocity as a function of the solitons' initial separation [84, 88] and phases [83]. Given such generality, it is reasonable to expect the structure to manifest in our simulations, and the sensitivity to initial conditions observed is qualitatively consistent with its presence.

Resonant energy transfer is not the only mechanism that may be involved in non-integrable solitary-wave collisions. A distinct phenomenon named radiationless energy exchange is also known, and is dominant in the limit of weak perturbations away from integrability (see references [89, 90, 91, 92, 93, 94, 95, 96, 97]). This effect has been described in a variety of quasi-integrable systems, including weakly perturbed self-focusing NLSE, weakly perturbed sine-Gordon equations, and generalized NLSE. In short-lived bound states attributable to radiationless energy exchange, the occurrence of multiple oscillations is due to the transferral at each collision of only a small amount of energy. That this is a different mechanism from resonant energy transfer is made evident in the fact that it exhibits a different scaling with the strength of the perturbation [84], and is emphasized by the success of effective quasi-particle models not involving internal modes in capturing the features of scattering in such systems, including inelasticity, the formation of short-lived bound states, and fractal structure in the outgoing velocities after the bound state breaks. In this picture, developed for two-way collisions in the self-focusing NLSE perturbed by weak discretization in [83], for three-way collisions in a similarly perturbed sine-Gordon equation in [84], and for bright solitons in strongly coherently coupled GPEs in [98], the solitary waves are treated as massive particles interacting via a two-body potential whose properties are chosen to match the interactions between solitons of the corresponding integrable system. This is capable of describing scattering trajectories and predicting the scaling properties of the probability of a bound state with a certain lifetime forming. In this type of inelastic collisions, radiationless energy exchange occurs when the system is near separatrix multi-soliton states of the corresponding integrable equation, in which case very small perturbations can lead to very different outcomes of the scattering

event (see [84], where the effective particle model reflects this in an intuitive way in an interaction potential landscape possessing separatrices near which trajectories vary intricately). This line of research may be fruitful in explaining our case of magnetic solitons in the completely repulsive coupled GPEs, though the different dependence of energy on velocity of magnetic solitons with respect to the solitons considered in the cited works might be relevant, as might the difference in degrees of freedom: the magnetic solitons we have thus far worked with have only one free parameter, and the system is subject to the conservation of energy and momentum as well as total z-magnetization, which constrain outgoing soliton parameters in collisions. For inelasticity to be admitted in a model of two-way collisions may therefore require the consideration of multi-parameter solitons.

It may be the case that nonlinear excitations close to (multi-parameter) solitons of the integrable theory, resonant and radiationless energy transfer mechanisms, and radiative phenomena all play a role in the various scenarios we have come across. Distinguishing their effects may be attempted by characterizing the probabilistic properties of bound state lifetimes and of n-bounce windows, and by studying the scaling of the respective energy transfers with the strength of the perturbation. The latter should also be important in discerning whether the non-integrable behavior is entirely attributable to the discretization or if it is also a function of the value of g_s, and thus whether finite-lifetime bound states may be observed in actual condensate mixtures. On general grounds, as mentioned, the phenomenon should be expected, since it is related to any perturbation away from integrability.

5.2 Effects of coherent coupling

We now present some interesting observations encountered in simulations where the coherent coupling Ω is non-zero. The presence of coherent coupling does not simply introduce an external force acting on the objects we have considered thus far in its absence, but fundamentally alters the nature and dynamics of the nonlinear excitations of the system, since it changes the system's very symmetries, and with them its ground state and dynamical properties. For instance, since the relative phase is now fixed by the phase of Ω, the system admits domain walls of relative phase with a relative phase jump of 2π [21]. Similarly, one can expect solitary-wave excitations across which the relative phase must vary by an integer multiple of 2π, as demonstrated for weak coherent coupling in [99]. Nevertheless, we set out in the spirit of a perturbative approach to investigate the effects of the transverse field on the magnetic structures of the integrable theory, although we will also present some cases where the value of Ω is not small with respect to $g_s n_0/2\hbar$. Thus, the simulations reported here were carried out by integrating the coupled GPEs with $\Omega \neq 0$ with an initial state obtained from the analytical expressions for solitons from the LLE or via imaginary-time evolution with $\Omega = 0$. We will first present phenomena observed for an initial state derived in the immiscible regime, then more briefly consider the miscible regime (these terms refer to the initial state, since they are not applicable to the coherently coupled system). Throughout, the total density is seen to be constant to a good approximation, so we focus on the relative density and relative phase as dynamical variables and use the precisely applicable language of the Landau-Lifshitz equation where convenient.

5.2.1 Immiscible

The most interesting phenomena we observed occurred for initial states similar to magnetic solitons of the immiscible mixture evolving in the ferromagnetic regime (small Ω). These simulations were prompted by our focus on solitons, but the objects in question can be more properly characterized as small spin domains, whose similarity to the excitations of the integrable theory is not crucial. On the other hand, as we will see, it is crucial that the objects are small. This less stringent definition is reminiscent of the results of chapter 3,

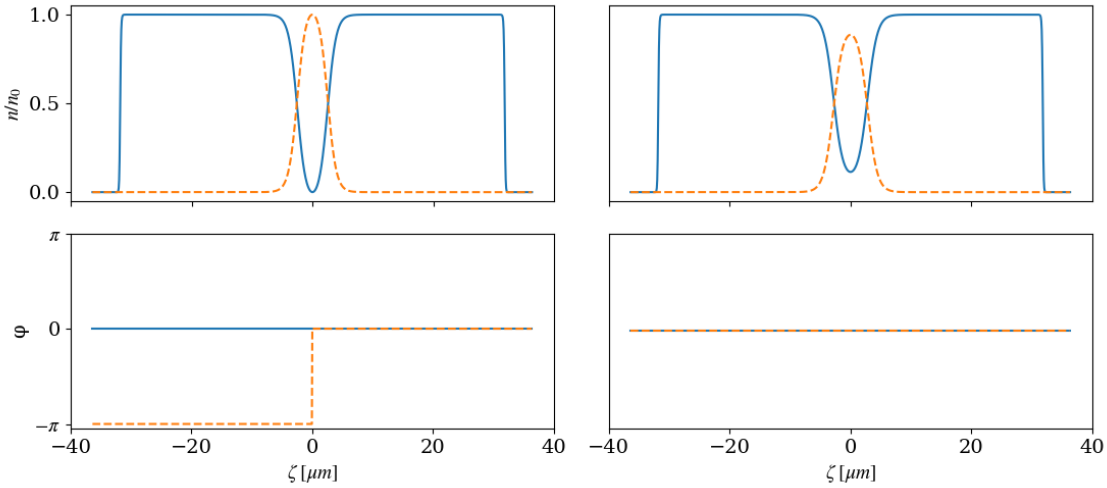

Figure 33: Sample initial states subjected to numerical evolution in the presence of coherent coupling, with real and odd ψ_1 (left) and real and even ψ_1 (right).

but here we find qualitatively different dynamics according to whether the relative phase jump $\Delta\varphi$ across the domain is zero or π, while the same distinction in the context of the mobile Josephson junction simply reflects itself in two different values of the initial momentum, and therefore leads only to a shift in the oscillatory trajectory. In the present case, we describe the two classes separately, beginning with the case $\Delta\varphi = 0$. The initial state for these simulations (Fig. 33) is obtained through imaginary-time evolution at $\Omega = 0$, resulting in initial order parameters which are real and even. Accordingly, we will refer to this structure as an even spin domain and to its counterpart with $\Delta\varphi = \pi$ as an odd spin domain. The resulting dynamics are remarkably simple for small Ω.

We find two qualitatively different dynamical regimes according to the strength of the coherent coupling. For the smallest values of Ω, the spin domain remains stationary and undergoes oscillations in its width and amplitude. Two frequencies are evident in the density and phase dynamics, as is visible in Fig. 34. The higher frequency is that of phase rotation and connected relative density dynamics outside of the spin domain, which are recognizable as the oscillatory particle transfer contributed by coherent coupling to the dynamics of a uniform system, though here they are of course coupled to spatial dynamics. These are such that the slope of the relative density in the overlap region where it changes sign undergoes small oscillations at about the same frequency as the relative population dynamics. The lower frequency is that of the width oscillations. It decreases as Ω increases, while their amplitude increases, up to a threshold frequency Ω_0^* (the subscript serves to distinguish this quantity from a similar one that appears in the dynamics of the odd spin domain). The relative phase inside the spin domain is approximately uniform and decreases at a constant rate, resulting in phase rotation at the same frequency as the width oscillations. The threshold frequency is higher for smaller spin domains, i.e. for smaller minority component particle numbers N_2. We give some considerations on the oscillatory behavior below, after presenting periodic dynamics observed for odd spin domains. Above the threshold frequency, the spin domain again has a stationary center of mass, but its width increases indefinitely rather than oscillating (see Fig. 35). Its broadening accelerates from zero velocity to a constant velocity which it maintains until the system's edges are reached. The high-frequency dynamics

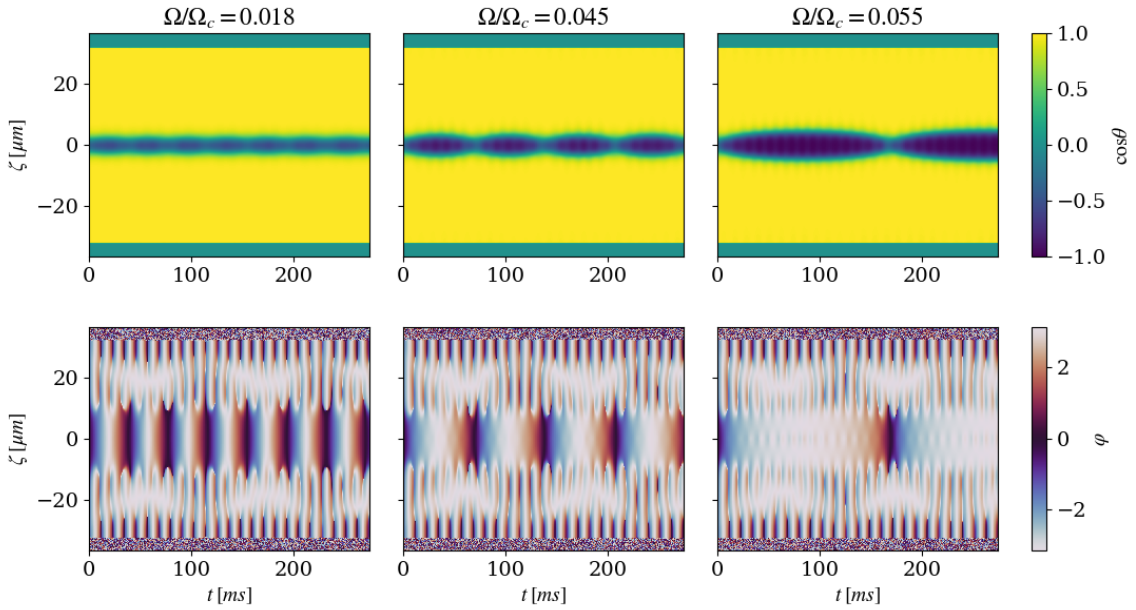

Figure 34: Evolution of a small even spin domain at three values of $\Omega < \Omega_0^*$. The frequency of the width oscillations decreases with increasing Ω, while their amplitude increases. The frequency of the spin oscillations outside the domain does not depend on Ω.

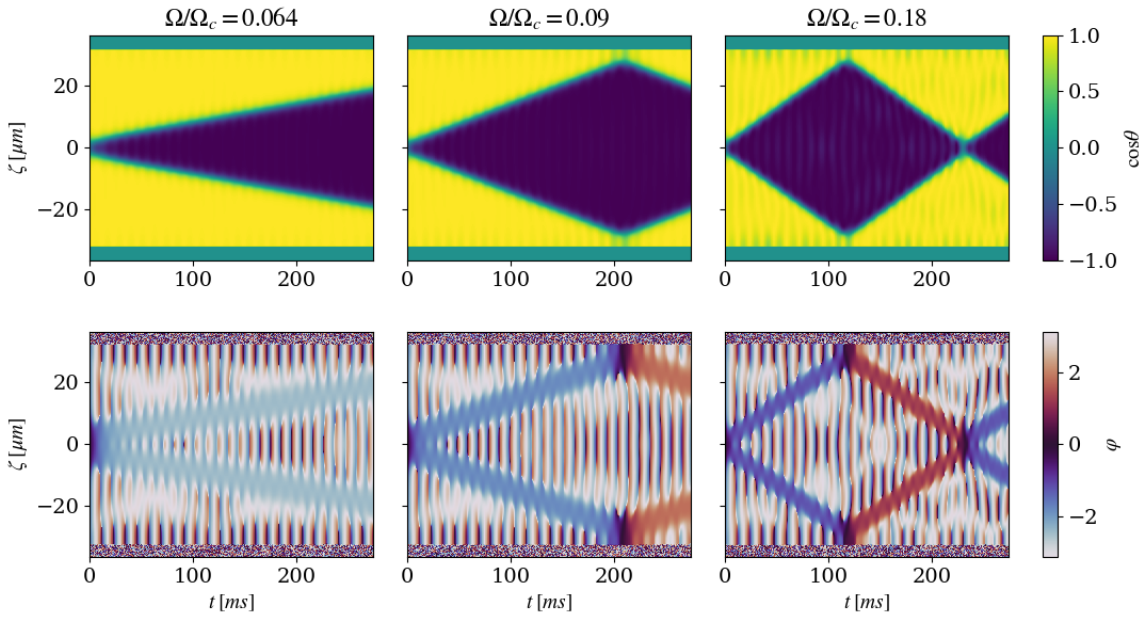

Figure 35: Evolution of a small even spin domain at three values of $\Omega > \Omega_0^*$. The speed at which the domain broadens increases with Ω. High-frequency oscillations to those seen below Ω_0^* are visible.

outside the spin domain are still present and quite similar to those seen at smaller Ω. Meanwhile, the relative phase is uniform and constant (except for a decrease during the acceleration) in the overlap region. The speed of the broadening increases with increasing values of the coherent coupling. However, as Ω approaches its critical value $\Omega_c = g_s n_0/2\hbar$, marking the magnetic phase transition, the amplitude and spatial size of the relative density oscillations increase, eventually destroying the simple dynamics described. This seems to occur at around $\Omega = \Omega_c/2$. For $\Omega > \Omega_c$, large-amplitude relative population oscillations dominate the dynamics. Evolution at these higher values of the coherent coupling is illustrated in Fig. 36.

The properties of the broadening dynamics suggest an interpretation in terms of two domain walls of the z-magnetization which are initially close to each other and then separate due to a repulsive interaction between them. The evolution would in this way be framed as a clear illustration of the new dynamics which the presence of coherent coupling can induce in the structures of the magnetic system. Domain walls of magnetization, which are a solitonic solution of the easy-axis LLE, are stationary in the integrable system, since the total z-magnetization N is an integral of motion. A domain wall separates regions of opposite magnetization, so a change in its position would mean a change in N and is therefore forbidden. The presence of a transverse field, however, breaks this conservation law and so allows motion of domain walls. In our case, one may hope to show that an effective repulsive interaction exists at short range between domain walls of the kind used here, providing the initial acceleration, and that once a domain wall is set in motion it will propagate at constant speed. The initial repulsion may be related to the higher quantum pressure associated with the curvature of the minority component when the spin domain is small. However, this model should also account for the previously mentioned fact that a small enough spin domain will not broaden at a fixed Ω, presumably by providing for the possibility of bound state formation due to attractive interaction between domain walls at even shorter ranges. These considerations motivate simulations of single domain walls under

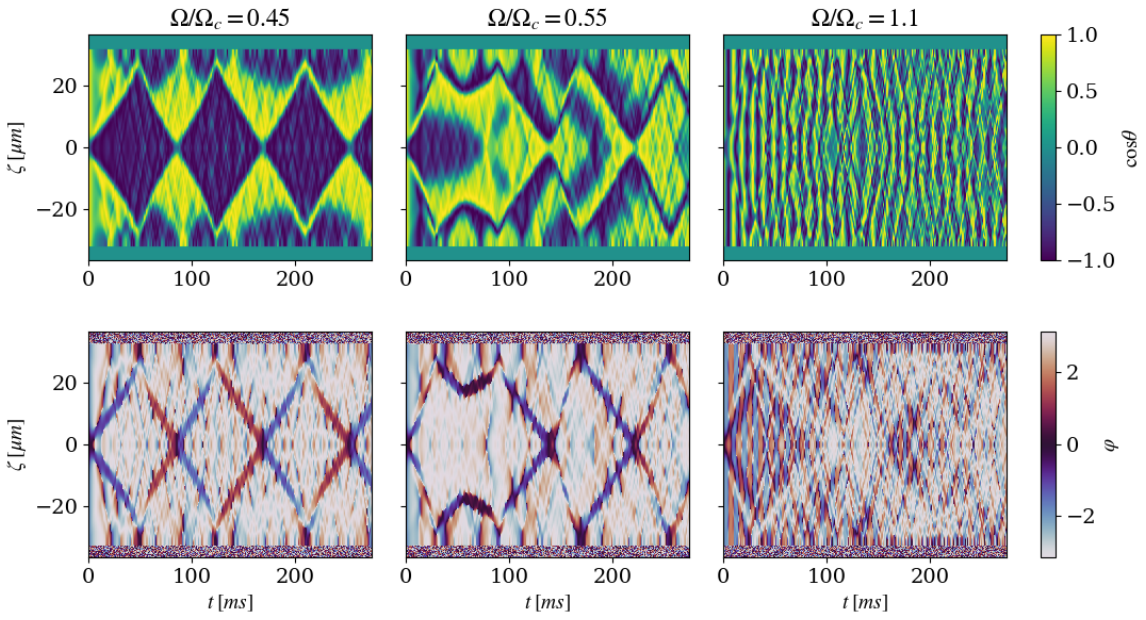

Figure 36: Evolution of a small even spin domain for values of $\Omega > \Omega_0^*$ just below $\Omega_c/2$ (left), just above $\Omega_c/2$ (middle), and just above Ω_c (right).

coherent coupling, which we report below.

The behavior of a small spin domain with $\Delta\varphi = \pi$ has analogies to the $\Delta\varphi = 0$ case, as well as marked differences: for an initial state obtained through imaginary-time evolution at $\Omega = 0$ with the constraint that ψ_1 changes sign at $\zeta = 0$, resulting in real odd ψ_1 and real even ψ_2 at the initial time, the spin domain is observed to have an oscillating trajectory while the number of particles in each component is nearly conserved. This is illustrated in Figs. 37 and 38. Again, two frequency scales are evident in the evolution. The higher frequency is seen in the relative density as quasi-periodic population transfer in the uniform regions and as small shape oscillations of the spin domain, and in the relative phase as a faster rotation outside the spin domain. This is quite similar to what is seen for the even spin domain. The lower frequency is that of translational oscillations, and on the corresponding time scale the system evolves nearly rigidly, with the order parameters reasonably well approximated by functions of $\zeta - X(t)$. The relative phase in the region of the spin domain maintains its π discontinuity at the domain's central position, and is nearly (piecewise) uniform, but not constant: it undergoes rotation at the same frequency as the translational oscillations. The frequency of the translational oscillations decreases with increasing Ω, and their amplitude increases. Furthermore, a drift in the center of the oscillations is visible at larger Ω. Whether this motion is a simple acceleration in one direction or possibly a third, very low frequency is inconclusive, since in all trials the drift led the spin domain to reach the edge of the system. The drift is noticeably affected by changes in the simulated system size, indicating that it is likely a finite-size effect (see Fig. 38).

In this case, an interpretation in terms of a bound state of two domain walls, now interacting attractively thanks to the relative phase between them, may be possible, but seems to leave open the question of why the center of mass of the bound state should move. On the other hand, the rigidity of the evolution suggests that it may be fruitful to ask why the system maintains itself close to a stationary state of the non-coherently-coupled

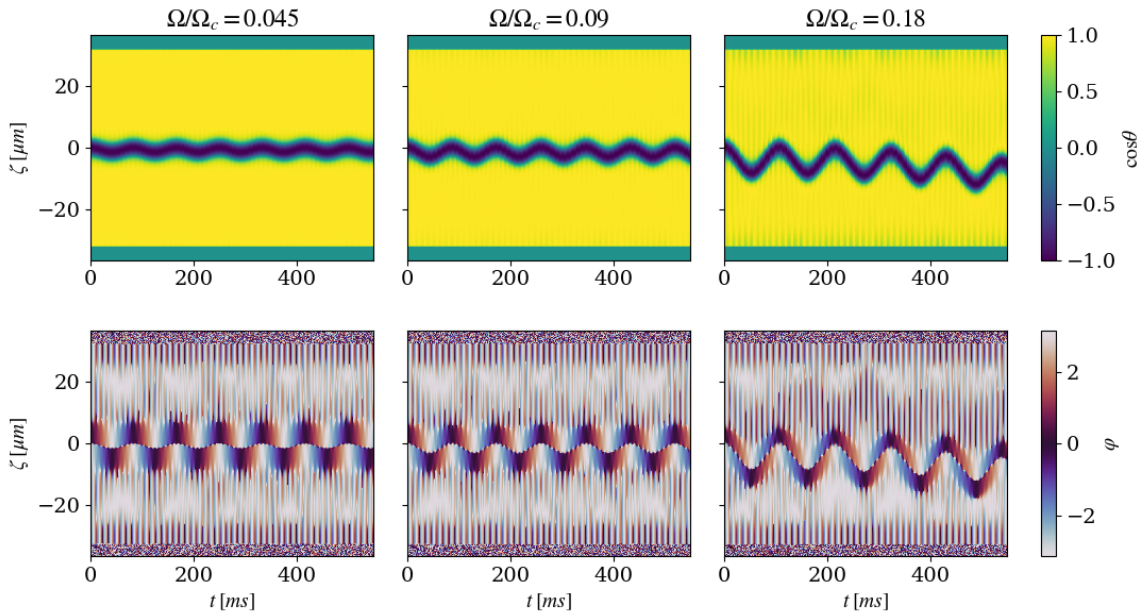

Figure 37: Relative density and relative phase during numerical evolutions of small spin domains with $\Delta\varphi = \pi$ for three different values of the coherent coupling below the threshold value Ω_1^*. The frequency of the spin domain's oscillations decreases with increasing Ω, while their amplitude increases. A drift in the center of the oscillations is noticeable at higher Ω.

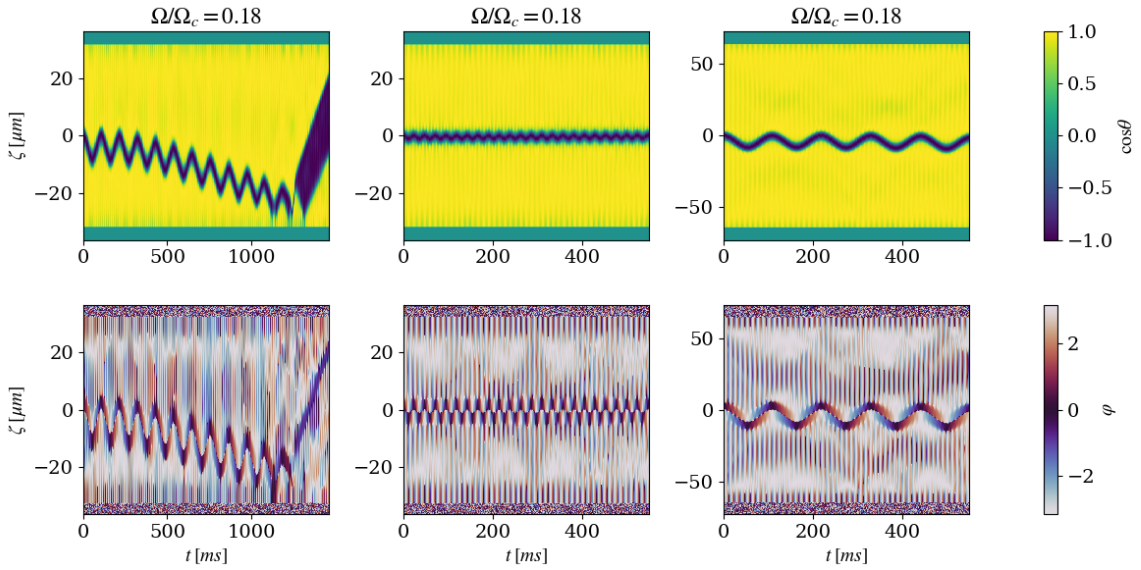

Figure 38: Further examples of evolution of an odd spin domain under coherent coupling. The left column shows the rest of the evolution in the right column of Fig. 37, up to when the domain reaches the system's edge. The middle column shows the effect on oscillation frequency and amplitude of changing the number of particles in the minority component: here, $N_2 = 10000$ while the rest of the simulations plotted use $N_2 = 15000$. The right column reports a simulation where the system is twice as large as in the other examples, demonstrating that the frequency and amplitude of the oscillations are unaffected by this change, while providing an indication that the drift may be a finite-size effect (the other parameters are equal to those used in the right column of Fig. 37).

system, and what mechanisms come into play given this restriction on the dynamics. We have no satisfactory answer to the first question, but taking it as a given and considering the second may lead to some useful guidelines for thinking about the problem. In this perspective, it seems likely that the effect of the coherent coupling is to transfer to the center-of-mass dynamics a periodicity which stems from the phase dynamics and is already present at $\Omega = 0$. In this case, the initial state we consider is a stationary state, and it evolves by phase rotation determined by the two distinct chemical potentials μ_j. Far from the spin domain, n_2 vanishes, so φ_2 is not defined and the time evolution is described by $\dot{\varphi}_1 = \mu_1/\hbar$. The situation at finite Ω is analogous, with the phase dynamics now coupled to population dynamics. Inside the spin domain, on the other hand, both components have non-zero density. For $\Omega = 0$, therefore, we have the stationary evolution $\dot{\varphi}_j = \mu_j/\hbar$, and so the relative phase dynamics $\dot{\varphi} = \Delta\mu/\hbar \equiv (\mu_2 - \mu_1)/\hbar$. For a uniform system the chemical potential difference is $\Delta\mu = g_s n_0 \cos\theta$. Now consider a non-zero coherent coupling: the system, strictly speaking, has a single chemical potential. Nevertheless, the quantity $g_s n_0 \cos\theta$ remains significant: for a uniform system, Eq. 33d reads

$$\dot{\varphi} = \frac{g_s n_0 \cos\theta}{\hbar}\left(1 - \frac{\Omega}{\Omega_c}\frac{\cos\varphi}{\sin\theta}\right). \tag{82}$$

As Ω increases, the rate of relative phase rotation decreases until it reaches zero at a fraction $\sin\theta/\cos\varphi$ of the magnetic transition frequency. Of course, here θ and φ are generally functions of time even in a uniform system (in a coherently coupled stationary state, $\dot{\varphi} = 0$, since the true chemical potential difference vanishes). However, in our special case of rigid motion, this reasoning - although we have no justification for why the motion is rigid in the first place - provides a little initial insight into the dynamics, correctly suggesting that the frequency of the oscillatory dynamics should decrease with increasing Ω, vanishing in the limit of a threshold frequency $\Omega_1^* < \Omega_c$. This is borne out by simulations, illustrated in Fig. 39, which yield observed values of Ω_1^* dependent on the size of the spin domain. Phenomena exhibiting critical values of the coherent coupling related but not identical to the magnetic transition frequency are known: for instance, domain walls of relative phase are a metastable configuration of the mixture for $\Omega < \Omega_c/3$ [21], and running phase modes of the internal Bose-Josephson dynamics in the uniform coherently coupled mixture exist for $\Omega < \Omega_c/2$ [9]. Indeed, a possible interpretation of the phenomenon reported here is as a transferral onto the translational degree of freedom of the low-Ω dynamics of the Bose-Josephson equations. The system may be conceptualied as being nearly uniform, and thus expected to admit running phase modes as a result of coherent coupling, with a localized impurity, whose motion is coupled to the phase dynamics of the mixture in much the same way as discussed in chapter 3. The vanishing of the oscillation frequency as Ω approaches Ω_1^* is then reminiscent of the critical slowing down seen in the Bose-Josephson system. In this perspective, the importance of the spin domain being small may be seen as a requirement for its interpretation as a weak coupling forming a mobile Josephson junction.

Above the threshold frequency, the observed dynamics are qualitatively different, as illustrated in Fig. 39. In this case, in addition to the increasingly untidy magnetization dynamics in the uniform regions, the spin domain broadens and accelerates towards negative ζ (the region where the relative phase is initially $-\pi$), and the relative phase in it no longer rotates. It is now well-defined on its margins, that is, in the overlap regions, and there is more or less uniform and constant. This is similar to the behavior of the even domain discussed above, and is more plausibly describable in terms of domain wall motion. In our simulations, the broadening domain always continued to accelerate until it reached the edge of the system.

Unfortunately, the mechanism whereby the relative phase rotation is accompanied by translational oscillations and the reason for the system evolving almost rigidly remain obscure. A related observation likely to be of relevance is the fact that for this class of initial states the conservation of each species' particle number is broken only weakly. The connection between this and rigid motion is rather close, since it is easy to check that $\partial_t(N_1 - N_2)$ vanishes if ψ_1 and ψ_2 are real. If this is the case at all times, the chemical potentials can be

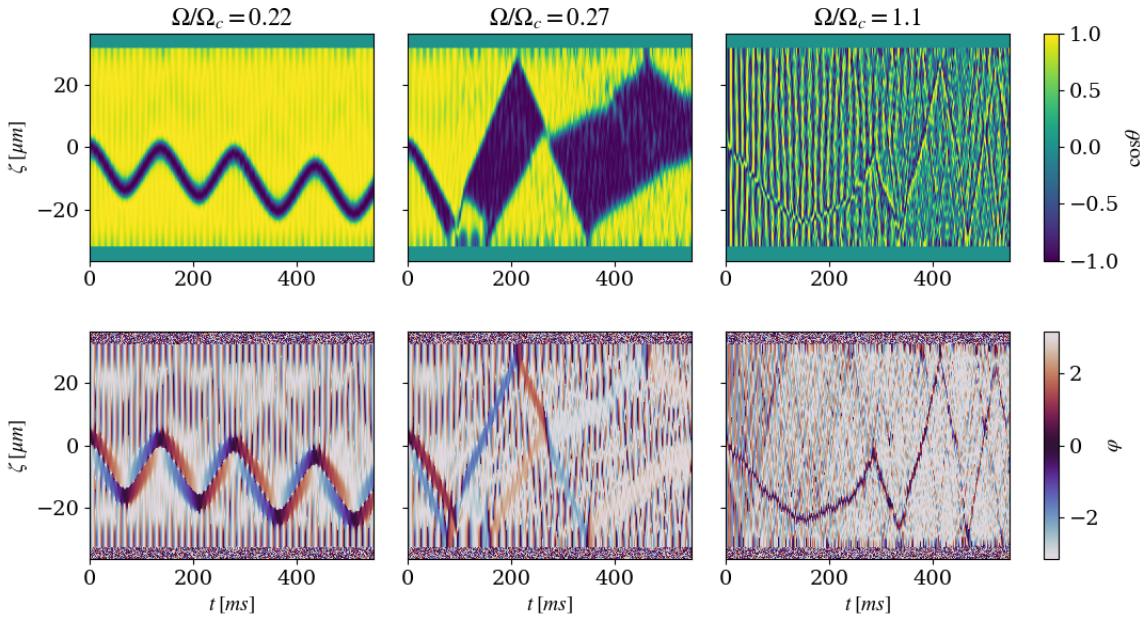

Figure 39: Relative density and relative phase during numerical evolutions of small spin domains with $\Delta\varphi = \pi$ for values of Ω just below the threshold frequency Ω_1^* (left), just above it (middle), and above the magnetic critical frequency Ω_c (right). For the initial state considered here, Ω_1^*/Ω_c seems to be very close to $1/4$. The differences between the dynamics below and above the threshold are marked even for small changes in Ω: simulations at $\Omega/\Omega_c = 0.245$ and $\Omega/\Omega_c = 0.255$ exhibit the same differences. We prefer to report the simulations shown here because they display the relevant behavior more clearly. When Ω is larger than Ω_1^* but still considerably below Ω_c, there are hints of the formation and breaking of domain-wall bound states. Above the magnetic critical frequency, the dynamics are dominated by precession about the transverse field.

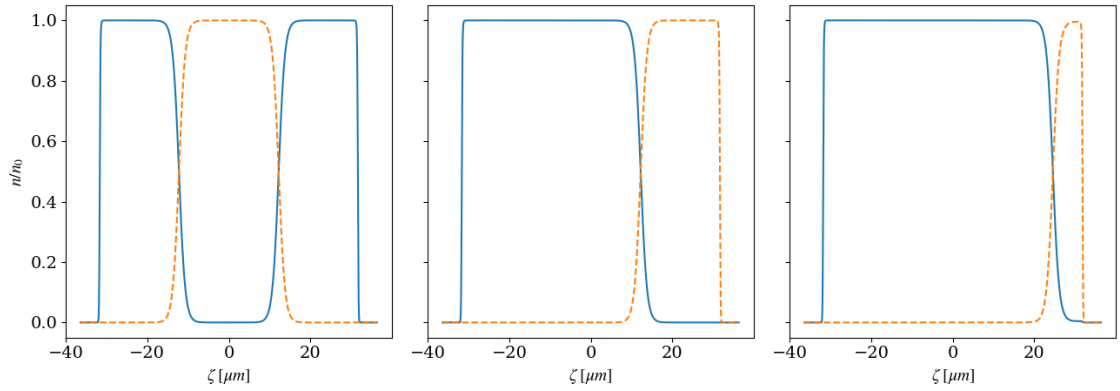

Figure 40: Initial states of simulations of large spin domains (left, corresponding to panel a of Fig. 41) and domain walls (the middle panel corresponding to panel b and the right panel to panel c of Fig. 41).

individually defined, and, calculating them as $\mu_j = \int \psi_j^* \hat{H} \psi_j \, \mathrm{d}x \, / N_j$, they bear a contribution proportional to Ω, but their difference is equal to its value at $\Omega = 0$.

Beyond these hints regarding the frequency of the observed oscillations, much remains to be understood, including the Ω dependence of their amplitude and the center-of-mass drift. The analogies between the behavior of odd and even domains suggests a unified description should be possible, with the differences, in particular the prevalence of center-of-mass or of width dynamics, clearly stemming from the difference in symmetry. Note that the simulations presented here were all obtained for $g_s/g = 0.01$. We obtained similar results for larger deviations from the miscibility transitions, up to $g_s/g = 1$.

We now briefly consider the evolution of larger spin domains and of single domain walls under coherent coupling, in order to assess the relevance of domain wall dynamics to explaining the observations found for small spin domains. Representative simulations are reported in Fig. 41. The initial states (Fig. 40) were obtained through imaginary-time evolution. Although, as already stated, domain wall motion is allowed by coherent coupling, the application of $\Omega \neq 0$ was not in itself enough to set in motion an initially stationary domain wall in our simulations. The dynamics of a single domain wall well-separated from the system's edges consists in a width oscillation which coexists with the usual magnetization and phase dynamics also present in the uniform system. Correspondingly, large spin domains which can presumably be analyzed as two separate domain walls do not display any of the peculiar features of small domain walls discussed above. Rather, each domain wall composing them evolves much as it would on its own. Proximity of a domain wall to the edges of the system, where the condensate densities are forced to vanish, does set the domain wall in motion, possibly as an effect of the quantum pressure of the small region between them, and it then moves at constant velocity. When the domain wall initially has a uniform relative phase of π (to mimic the situation in an odd spin domain), a bound state may form. These observations suggest that the broadening of small even spin domains can fruitfully be analyzed as the evolution of two separate domain walls, but not the oscillatory phenomena seen at small Ω.

5.2.2 Miscible

Here we consider the effect of coherent coupling on magnetic solitons of the weakly miscible mixture - that is, we simulate the evolution of initial states obtained in the way described in chapter 4. Since we

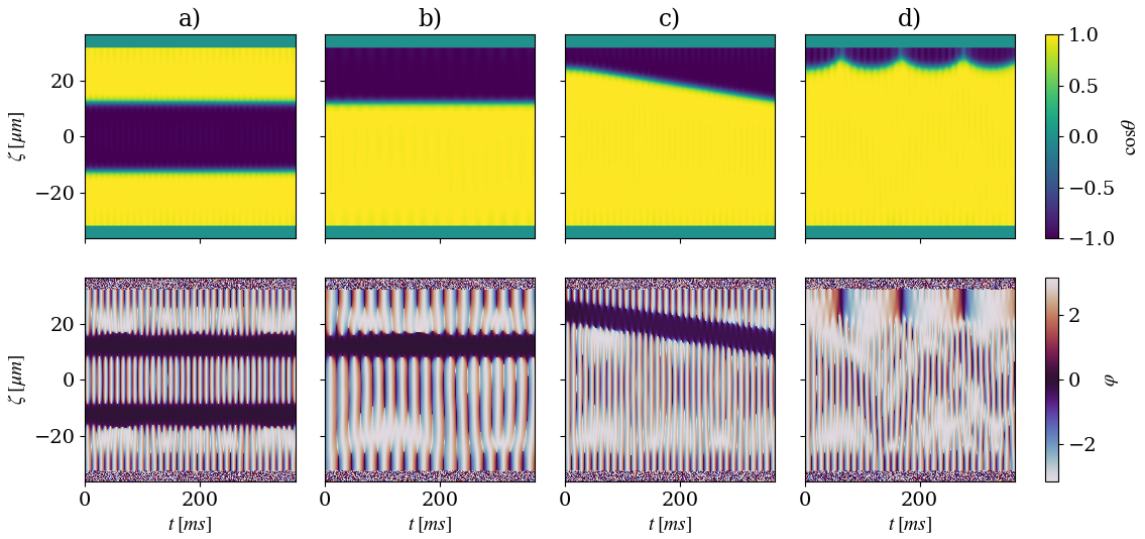

Figure 41: Numerical evolutions of domain walls under coherent coupling $\Omega/\Omega_c = 0.09$ at $g_s/g = 0.01$. In column a, a large even spin domain is nearly stationary, with some slope oscillations at its edges, and is describable as a pair of domain walls. This is demonstrated by column b, which shows a single domain wall with an initial uniform relative phase of zero, well-separated from the system's edges. The behaviors of a large odd spin domain and of a domain wall with a uniform relative phase of π are very similar to the cases shown here, so we omit them. In column c, a domain wall with $\varphi = 0$ is repelled by the nearby edge of the system and propagates away at constant velocity. In column d, a domain wall with $\varphi = \pi$ forms a bound state with the nearby edge.

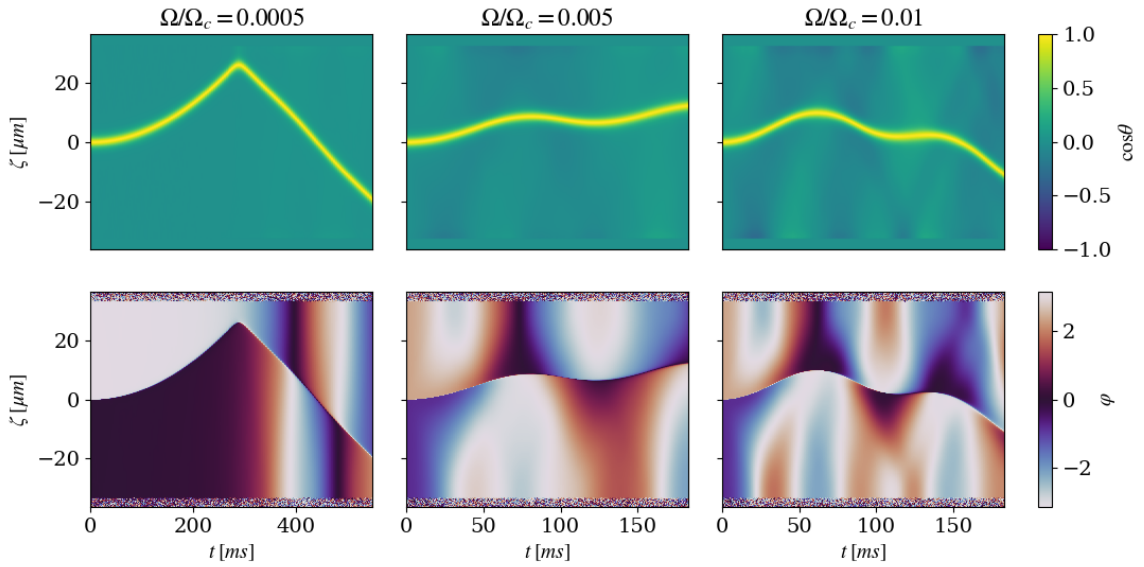

Figure 42: Evolution of a magnetic soliton of the miscible Manakov limit under three values of the coherent coupling at $g_s/g = -0.01$. The coherent coupling is given in units of the interaction frequency scale $\Omega_c \equiv |g_s|n_0/2\hbar$, even though, since $g_s < 0$, the system has no magnetic transition as a function of Ω. For very small Ω, the trajectory is simple (the bounce being due to the solitary wave reaching the system's edge), while it quickly becomes more complicated at higher Ω.

keep $g_{12} < g$, we are now working in the paramagnetic phase. We find that a weak transverse field can leave the solitary wave intact while acting on it as an external force. The resulting trajectory for a single solitary wave is relatively complicated except for the smallest values of Ω, coupled to significant background magnetization and current dynamics, and varies greatly with changes in Ω (see Fig. 42). Consistently with the paramagnetic character of the system, much smaller values of Ω suffice to destroy the quasiparticle-like dynamics compared to the ferromagnetic case presented above. It should be noted that, even when Ω is small enough to preserve the solitary wave, the relative phase undergoes significant variations in space and time, which distinguishes these dynamics from the more strictly quasiparticle-like behavior observed in preceding sections in the absence of coherent coupling, where the relative phase was uniform and constant. Interestingly, the dynamics of pairs of solitary waves is in some ways simpler (see Fig. 43). Initially stationary solitary waves of opposite signs are consistently accelerated towards each other and form bound states for considerably larger initial separations than those observed to result in bound state formation at $\Omega = 0$, while solitary waves of the same sign are accelerated away from each other. In both cases, the relative phase is closer to being piecewise uniform and constant, as for $\Omega = 0$. Here, too, the bound states have finite lifetimes, and their duration and outcome depend strongly on initial conditions. Much the same considerations as those given in section 5.1 apply, with an additional perturbation away from integrability presumably increasing the importance of the relevant phenomena. The formation of bound states, in particular, seems to happen more easily in the presence of coherent coupling.

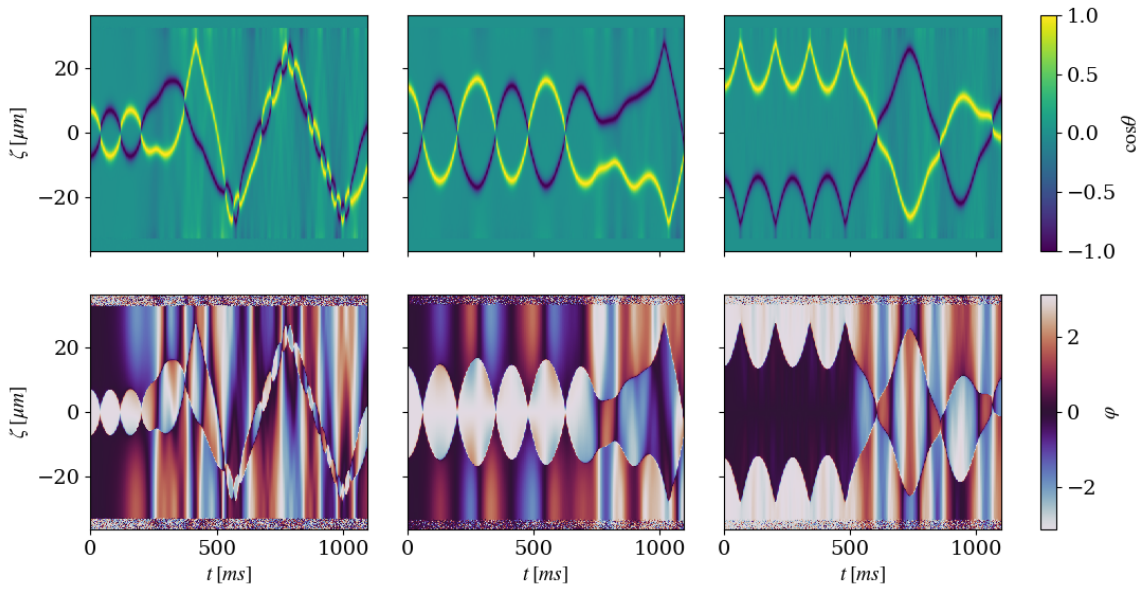

Figure 43: Evolution of pairs of magnetic solitons of the miscible Manakov limit at $g_s/g = -0.01$ and $\Omega/\Omega_c = 0.005$. In the left column, their initial separation is 14.1 μm, while in the middle and right columns it is 28.2 μm. In the right column, an initial uniform relative phase shift of π has been applied, which is equivalent to giving Ω a phase $\varphi_\Omega = \pi$.

5.3 Conclusion

The material presented in this chapter provides some interesting problems for future research. At present, the phenomenon of finite-lifetime bound state formation in the absence of coherent coupling seems likely to be susceptible to an explanation in relatively easily identified terms, within the framework of well-understood mechanisms that have been extensively documented and studied in a variety of similar cases in the literature. Barring surprises, what remains is to apply the available theory in the particular case of the repulsive coupled GPEs. A point to clarify is whether it is straightforward to apply the same framework in the coherently coupled case, where relative phase dynamics in simulations indicate a possible complication with respect to the simpler quasiparticle models in which such dynamics are taken to be trivial. However, coherently coupled mixtures have been studied in this context [98, 97], so any additional difficulties should not be insurmountable.

The questions that present themselves for the dynamics of small spin domains in the ferromagnetic coherently coupled mixture are of a somewhat more basic nature. Here what is necessary is to identify the mechanisms leading to the phenomena seen in simulations. A promising direction to investigate is the role of internal Bose-Josephson dynamics coupled to a mobile Josephson junction constituted by the small spin domain. We intend to produce a publication addressing these phenomena, as well as one reporting the results of chapter 4 on solitary wave collisions.

Several questions raised in previous sections also remain open for future investigation. As regards the behavior of solitary waves impinging on sharp density interfaces, an explanation, and a way to calculate the lifetime, of the quasi-static wave excited near the critical incoming velocity could be looked for. The role of radiation should be clarified, characterizing the types and intensity of excitations, linear and nonlinear, emitted during transmission and seeking to describe the differences in the properties of the radiation observed during reflection. Furthermore, one may attempt to clarify whether the zero-energy limit is purely reflective for solitary waves, unlike for elementary excitations. Research along these lines would help to understand why the simple quasiparticle picture employed adequately describes the outgoing velocities while ignoring radiation, and would benefit from the extensive knowledge of the LLE's spectrum of solitons (including potentially relevant multi-parameter families) and radiation.

The work presented on magnetic soliton dynamics under external field gradients raises the possibility of observing oscillations of impurities in other quasi-one-dimensional systems, since we expect the phenomenon to occur in any case in which a mobile barrier acts as a weak link between regions of broken symmetry. Since the requirements for this are rather generic, the mobile Josephson junction dynamics can be expected in a wide variety of physical systems. Besides this, a fuller understanding is needful of why the system we considered is seen in simulations to keep itself in the constant-density regime, where the linear Josephson effect arises, so accurately even for large deviations from the Manakov limit. Furthermore, it may be of interest to investigate how the phenomenon breaks down as the quasi-one-dimensional limit is gradually abandoned.

Appendix: Numerical methods

We made use of numerical simulations to integrate the coupled GPEs in order to check analytical results obtained under approximations and to probe situations for which we do not have approximate analytical predictions. The algorithms used employ a split-step pseudospectral method in which, at each iteration, the state of the system is propagated forward in time first by half a time step during which only the kinetic term of the Hamiltonian is taken into account, then by another half-step during which only the potential and interaction terms are used. This allows efficient treatment of both contributions by allowing each to be evaluated in a basis of functions which diagonalizes it: the kinetic term using Fourier-transformed state functions (allowing the use of the fast Fourier transform), and the potential and interaction terms in the position representation. Such a scheme yields the correct evolution in the limit of small time steps.

In more detail, if we express the coupled GPEs for the order parameter vector $\Psi(\zeta,t) = (\psi_1(\zeta,t)\ \psi_2(\zeta,t))^T$ in units of an arbitrary length ℓ_0 and time $m\ell_0^2/\hbar$ as

$$i\frac{\partial\Psi}{\partial t} = \hat{H}[\Psi]\Psi = -\frac{1}{2}\frac{\partial^2\Psi}{\partial\zeta^2} + \hat{U}[\Psi]\Psi \tag{83}$$

where

$$\hat{U} \equiv \begin{pmatrix} V_{\mathrm{ext},1} + g_{11}|\psi_1|^2 + g_{12}|\psi_2|^2 & \Omega \\ \Omega^* & V_{\mathrm{ext},2} + g_{22}|\psi_2|^2 + g_{21}|\psi_1|^2 \end{pmatrix},$$

the numerical integration is based on the Trotter-like expression

$$\Psi(\zeta,t) \approx \prod_{n=0}^{N_t=t/\Delta t} e^{-i\hat{H}[\Psi(\zeta,n\Delta t)]\Delta t}\Psi(\zeta,0), \tag{84}$$

which becomes exact in the limit $\Delta t \to 0,\ N_t \to +\infty$. In practice, the algorithm should be used with a suitably small Δt; in particular, it is stable if the diffusion limit condition $\Delta t < \Delta\zeta^2/2$ is satisfied for a given spatial discretization step[10] $\Delta\zeta$. To evaluate the exponential in Eq. 84, one uses the approximation

$$e^{i\hat{H}\Delta t} \approx e^{i\hat{U}\Delta t}e^{-i\frac{\Delta t}{2}\frac{\partial^2}{\partial\zeta^2}},$$

which also becomes exact in the limit $\Delta t \to 0$. Having done this, the first half-step is reduced to a product in Fourier space as

$$e^{-i\frac{\Delta t}{2}\frac{\partial^2}{\partial\zeta^2}}\Psi(\zeta,(n-1)\Delta t) = \mathcal{F}^{-1}[e^{i\frac{\Delta t}{2}k^2}\mathcal{F}[\Psi(\zeta,(n-1)\Delta t)](k)],$$

then the second half-step is calculated using $\hat{U}[e^{-i(\Delta t/2)\partial_\zeta^2}\Psi(\zeta,(n-1)\Delta t)]$, yielding $\Psi(\zeta,n\Delta t)$. The diagonal part of $\hat{U}$ gives rise to a product directly, since the exponential of a diagonal matrix is the diagonal matrix of the exponentials of its diagonal elements. To deal with a non-zero value of Ω, we again use the approximation

$$e^{-i\hat{U}\Delta t} \approx e^{-i\hat{U}_{\mathrm{diag}}\Delta t}e^{-i\Omega_x\hat{\sigma}_x\Delta t}e^{i\Omega_y\hat{\sigma}_y\Delta t},$$

[10] In our simulations, we discretized our system into 1024 or 2048 points with $\Delta\zeta \approx 0.07\mu m$.

where Ω_x and Ω_y are the real and imaginary parts of Ω. The exponentials involving Ω are

$$\begin{aligned} e^{-i\Omega_x\hat{\sigma}_x\Delta t} &= \sum_{n=0}^{\infty}\frac{(-i\Omega_x\hat{\sigma}_x\Delta t)^n}{n!} \\ &= \sum_{n=0}^{\infty}\frac{(-i\Omega_x\Delta t)^{2n}}{(2n)!}\mathbb{1} + \sum_{n=0}^{\infty}\frac{(-i\Omega_x\Delta t)^{2n+1}}{(2n+1)!}\hat{\sigma}_x \\ &= \cos\big(\Omega_x\Delta t\big)\mathbb{1} - i\sin\big(\Omega_x\Delta t\big)\hat{\sigma}_x, \end{aligned}$$

where we have used the fact that the Pauli matrices square to the identity matrix; likewise,

$$e^{i\Omega_y\hat{\sigma}_y\Delta t} = \cos\big(\Omega_y\Delta t\big)\mathbb{1} + i\sin\big(\Omega_y\Delta t\big)\hat{\sigma}_y.$$

Thus, every term of the time evolution operator is implemented by successive multiplications of the state vectors and their Fourier transforms by appropriate quantities. Finally, the state vectors are normalized to the set atom numbers at each iteration (separately for $\Omega = 0$ and in sum for $\Omega \neq 0$) to ensure this conservation law is strictly satisfied. This outlines the approach of the code to the integration of the coupled GPEs. To complete the discussion of numerical methods, we mention the use of imaginary-time evolution. In this method, the same algorithm described schematically for the evolution of the system is run with an imaginary value of the time step $\Delta t = i|\Delta t|$, including normalization at every iteration. This leads to a strictly decreasing value for the Gross-Pitaevskii energy, which is evaluated at every iteration, so that the imaginary-time evolution converges to the system's ground state (except for certain initial states, for which the procedure leads to an excited stationary state). The code is stopped when the difference in energy in consecutive iterations drops below a set convergence threshold. This allows a good approximation of the ground state to be found and then used as an initial state for the real-time evolution algorithm. In the case of imaginary-time evolution under a linear hermitian operator, $-\partial_t\psi = \hat{H}_{\text{lin}}\psi$, this fact has a very intuitive grounding: any function ψ can be expressed as a linear combination of the eigenfunctions ϕ_n of $\hat{H}_{\text{lin}}$, yielding an equation for the time dependence of the coefficients:

$$\begin{aligned} \psi_(\zeta,t) = \sum_n c_n(t)\phi_n(\zeta) \implies -\frac{\partial\psi}{\partial t} = -\sum_n \dot{c}_n\phi_n = \hat{H}_{\text{lin}}\sum_n c_n\phi_n = \sum_n E_n c_n\phi_n \\ \implies \dot{c}_n = -E_n c_n \implies \psi(\zeta,t) = \sum_n c_n(0)e^{-E_n t}\phi_n. \end{aligned}$$

Thus, every eigenstate composing the initial state falls away exponentially during imaginary-time evolution except for the ground state, which has $E_0 = 0$, so any initial state with non-zero $c_0(0)$ approaches the ground state for $t \to +\infty$. This derivation is not valid for the nonlinear Gross-Pitaevskii equation, for which $\hat{H}\sum_n c_n\phi_n \neq \sum_n c_n\hat{H}\phi_n$. However, it can be explicitly shown that the energy is non-increasing during imaginary-time evolution. For Eq. 83 with the replacement $t \to -it$, we have

$$\begin{aligned} \frac{\mathrm{d}E}{\mathrm{d}t} &= \sum_{j=1,2}\left[\frac{\mathrm{d}}{\mathrm{d}t}\int_{-\infty}^{+\infty}\frac{1}{2}\left|\frac{\partial\psi_j}{\partial\zeta}\right|^2 + V_{\text{ext},j}|\psi_j|^2 + \frac{g_{jj}}{2}|\psi_j|^4 + \frac{g_{12}}{2}|\psi_1|^2|\psi_2|^2\,\mathrm{d}\zeta\right] \\ &= \sum_{j=1,2}\left[\int_{-\infty}^{+\infty}\frac{\partial\psi_j^*}{\partial t}\left(-\frac{1}{2}\frac{\partial^2\psi_j}{\partial\zeta^2} + V_{\text{ext},j}\psi_j + g_{jj}|\psi_j|^2\psi_j + g_{12}|\psi_{2-j}|^2\psi_j\right)\mathrm{d}\zeta\right] + \text{c.c.} \\ &= \sum_{j=1,2}\left[2\int_{-\infty}^{+\infty} -\left|\frac{\partial\psi_j}{\partial t}\right|^2\mathrm{d}\zeta\right] \leq 0, \end{aligned}$$

with the inequality saturated only when Ψ is a stationary state. Thus imaginary-time evolution of the coupled GPEs converges to a stationary state. This will be the ground state for an appropriate choice of the initial state.

We report here the FORTRAN code employed in our simulations, thanking Arko Roy for contributing it. Note that in the absence of coherent coupling, the lines involving the variable CC should be commented out and normalization should be performed separately on each order parameter.

```
MODULE BASIC_DATA
  REAL (8), PARAMETER :: PI = 4.0D0*ATAN(1.0D0)
  COMPLEX (8), PARAMETER :: CI = (0.0D0, 1.0D0)
  INTEGER, PARAMETER :: NITER = 100000
  REAL(8), PARAMETER :: DX =  0.01D0, DT = 0.1D0*DX*DX
  INTEGER, PARAMETER :: NX = 1024, NX2 = NX/2+1, NXX = NX-1
  REAL(8), PARAMETER :: LX = DX*NX!
  INTEGER, PARAMETER :: STP = NINT(0.1D0/DT),  NSTP = 360000
  INTEGER, PARAMETER :: NSV = 250
  REAL (8), PARAMETER :: AMU = 1.66D-27, HBAR = 1.054560653D-34, AU = 0.529177208D-10
  COMPLEX (8) :: CDT
END MODULE BASIC_DATA

MODULE CGPE_DATA
  USE BASIC_DATA  , ONLY : NX, AMU, AU
  REAL (8), PARAMETER :: M = (23.0D0*AMU)
  REAL (8), PARAMETER          :: G011 = 54.54D0, G012 = 55.0854D0, &
                                  G021 = 55.0854D0, G022 = 54.54D0
  REAL (8), PARAMETER :: NUZ = 8.7D0, LAM1 = 67.24D0,LAM2=67.24D0,&
                         KAP1 = 67.24D0, KAP2 = 67.24D0
  REAL (8), PARAMETER :: NATOMS = 200000
  REAL (8), PARAMETER :: TOL = 1.0D-6
  REAL (8), DIMENSION(1:NX) :: X, X2
  REAL (8), DIMENSION(1:NX) :: KX
  REAL (8), DIMENSION(1:NX, 1:2) :: V
  REAL (8), DIMENSION(1:NX) :: R2
  COMPLEX (8), DIMENSION(1:NX, 1:2) :: PHI, PHIF, PHI_OLD, PHI_TEMP
  REAL (8), DIMENSION(1:NX) :: PHA
  REAL (8), DIMENSION(1:NX) :: PHB
  REAL (8), PARAMETER :: U = 0.05D0
  REAL (8), PARAMETER :: XIS = 0.21316D0
  REAL (8) :: RMOD, RPH
  REAL (8) :: G11, G22, G12, G21 , DETUN = 0.0D0
  REAL (8) :: AOSC, OMEGAM
  REAL (8) :: CC = 0.5D0  ! the time evolution and energy calculation
   need to be modified for complex cc
  INTEGER, PARAMETER :: SWITCH_IM = 2,  OPTION_P_C = 1
END MODULE CGPE_DATA

MODULE FFTW3
```

```
  USE, INTRINSIC :: ISO_C_BINDING
  INCLUDE 'fftw3.f03'
END MODULE FFTW3

MODULE FFTW_DATA
  USE BASIC_DATA, ONLY : NX
  USE FFTW3
  COMPLEX(C_DOUBLE_COMPLEX), DIMENSION(NX) :: FFTFX, FFTBX
  TYPE(C_PTR) :: PLANFX, PLANBX
END MODULE FFTW_DATA

!+++++++++++++++++++++++++++++++++++++++++++++++++++++++++++++++
!                        Main Program - CGPE2D
!
!+++++++++++++++++++++++++++++++++++++++++++++++++++++++++++++++

PROGRAM CGPE2D
  USE BASIC_DATA
  USE CGPE_DATA
  USE FFTW3

  IMPLICIT NONE

  INTERFACE
    SUBROUTINE INITIALIZE2C()
      IMPLICIT NONE
    END SUBROUTINE INITIALIZE2C

    SUBROUTINE KE2C()
      IMPLICIT NONE
    END SUBROUTINE KE2C

    SUBROUTINE SP2C()
      IMPLICIT NONE
    END SUBROUTINE SP2C

    SUBROUTINE NORM2C(PHI, NORM)
      USE BASIC_DATA, ONLY : NX
      IMPLICIT NONE
      COMPLEX (8), DIMENSION(1:NX, 1:2), INTENT(IN) :: PHI
      REAL (8), DIMENSION(1:2), INTENT(OUT) :: NORM
    END SUBROUTINE NORM2C

    SUBROUTINE NORM2T(PHI, NORMT)
      USE BASIC_DATA, ONLY : NX
      IMPLICIT NONE
```

```
    COMPLEX (8), DIMENSION(1:NX, 1:2), INTENT(IN) :: PHI
    REAL (8), INTENT(OUT) :: NORMT
  END SUBROUTINE NORM2T

  SUBROUTINE RAD2C(PHI, RMS)
    USE BASIC_DATA, ONLY : NX
    IMPLICIT NONE
    COMPLEX (8), DIMENSION(1:NX, 1:2), INTENT(IN) :: PHI
    REAL (8), DIMENSION(1:2), INTENT(OUT) :: RMS
  END SUBROUTINE RAD2C

  SUBROUTINE ENERGY2C(PHI, MU, EN)
    USE BASIC_DATA, ONLY : NX
    IMPLICIT NONE
    COMPLEX (8), DIMENSION(1:NX, 1:2), INTENT(INOUT) :: PHI
    REAL (8), DIMENSION(1:2), INTENT(OUT) :: MU
    REAL (8), INTENT(OUT) :: EN
  END SUBROUTINE ENERGY2C

  SUBROUTINE FFT2C()
    IMPLICIT NONE
  END SUBROUTINE FFT2C

  SUBROUTINE BFT2C()
    IMPLICIT NONE
  END SUBROUTINE BFT2C

  SUBROUTINE CREATE_PLANS()
    IMPLICIT NONE
  END SUBROUTINE CREATE_PLANS

  SUBROUTINE DESTROY_PLANS()
    IMPLICIT NONE
  END SUBROUTINE DESTROY_PLANS

END INTERFACE

INTEGER :: I, J, K, II, IOSTAT
REAL (8), DIMENSION(1:2) :: NORM, RMS, MU
REAL (8) ::  EN, START, FINISH, NORMT
REAL (8), DIMENSION(1:4) :: TMP
INTEGER :: START_CLOCK, STOP_CLOCK, CLOCK_RATE, CLOCK_MAX, idum = -1234
CHARACTER (LEN=10) DATE, TIME, ZONE
INTEGER, DIMENSION(1:8) :: VALUES
REAL (8) :: CONV = 0.0D0
CALL CPU_TIME(START)
```

```
SELECT CASE(SWITCH_IM)
  CASE(1)
    CDT = -CI*DT
    OPEN (2, FILE='file1_im_2C.dat', STATUS='UNKNOWN',FORM='FORMATTED',&
         ACTION='WRITE')
    OPEN (3, FILE='file2_im_2C.dat', STATUS='UNKNOWN',FORM='FORMATTED',&
         ACTION='WRITE')
    OPEN (8, FILE='solution_file_im_2C.dat', STATUS='UNKNOWN',FORM='FORMATTED',&
         ACTION='WRITE')
    OPEN (9, FILE='convergence_2C.dat', STATUS='UNKNOWN',FORM='FORMATTED',&
         ACTION='WRITE')
  CASE(2)
    CDT = DT
    OPEN (1, FILE='initial_sol_2C.dat', IOSTAT=iostat, STATUS='OLD',FORM='FORMATTED',&
         ACTION='READ')
    OPEN (2, FILE='file1_re_2C.dat', STATUS='UNKNOWN',FORM='FORMATTED',&
         ACTION='WRITE')
    OPEN (3, FILE='file2_re_2C.dat', STATUS='UNKNOWN',FORM='FORMATTED',&
         ACTION='WRITE')
    OPEN (8, FILE='solution_file_re_2C.dat', STATUS='UNKNOWN',FORM='FORMATTED',&
         ACTION='WRITE')
END SELECT

OMEGAM = 2.0D0*PI*NUZ
AOSC = SQRT(HBAR/(M*OMEGAM))

G11 = 2.0D0*SQRT(LAM1*KAP1)*G011*AU/AOSC
G12 = 2.0D0*SQRT(LAM1*KAP1)*G012*AU/AOSC
G21 = 2.0D0*SQRT(LAM1*KAP1)*G021*AU/AOSC
G22 = 2.0D0*SQRT(LAM2*KAP2)*G022*AU/AOSC


WRITE(2,*)
WRITE(2,900) SWITCH_IM, OPTION_P_C
WRITE(2,*)
WRITE(2,902) NX
WRITE(2,903) NITER, NSTP
WRITE(2,904) G11, G12, G22
WRITE(2,905) DX
WRITE(2,906) DT, LX
WRITE(2,907) OMEGAM, AOSC
WRITE(2,*)
WRITE(2,908) CC
WRITE(2,*)

900 FORMAT('SWITCH_IM = ',I2,', OPTION_P_C = ', I2)
```

```
  902 FORMAT('Grid points NX = ',I8, 'NY =', I8 )
  903 FORMAT('Iteration : NITER = 'I9,', NSTP = ',I9)
  904 FORMAT('G11 = ', F12.6, ', G12 = ', F12.6, ', G22 = ', F12.6 ' (all in units of Bohr radius)')
  905 FORMAT('Space Step DX = ',F10.6)
  906 FORMAT('Time Step  DT = ', F10.6, ', LX = ', F10.6)
  907 FORMAT('OMEGAM = ', F10.6,', AOSC = ', F12.6 ' m')
  908 FORMAT('CC = ', F12.6 ' in units of OMEGAM')

  IF((SWITCH_IM.NE.1))THEN
    IF(IOSTAT.NE.0) THEN
      PRINT*, 'Check if the "initial_sol_2C.dat" is available'
      STOP
    END IF
     DO I = 1, NX
          READ(1,*) X(I), (TMP(K), K = 1, 4)
          PHI(I,1) = SQRT(TMP(1))*EXP(CI*TMP(2))
          PHI(I,2) = SQRT(TMP(3))*EXP(CI*TMP(4))
       END DO
   END IF

  CALL INITIALIZE2C()

do i = 1, nx
          write(200, '(5f12.4)') x(i), (abs(PHI(I, K))**2, &
            ATAN2(AIMAG(PHI(I, K)),REAL(PHI(I, K))), K = 1, 2)
        end do

  CALL NORM2T(PHI, NORMT)
  write(*,*) "N_at = ", NORMT

  CALL NORM2C(PHI, NORM)
  CALL RAD2C(PHI, RMS)
  CALL ENERGY2C(PHI, MU, EN)
  write(*,*) "E = ", en
  WRITE (2, 1001)
  WRITE (2, 1002)
  WRITE (2, 1001)
  WRITE (2, 1003) SUM(NORM), EN, (MU(K), K = 1, 2), (ABS(PHI(NX2, K)), K = 1, 2)
  1001 FORMAT (18X, 70('-'))
  1002 FORMAT (19X, 'Norm',7X, 'EN', 11X, 'MU1', 9X, 'MU2', 8X,'|psi1(0)|', 8X, '|psi2(0)|')
  1003 FORMAT ('Initial : ', 3X, 1F11.4, 3F12.5, 2F12.5)

  CALL CREATE_PLANS()
OPEN (100, FILE='n_tot.dat', STATUS='UNKNOWN',FORM='FORMATTED',&
           ACTION='WRITE')
  DO II = 1, NITER
```

```
      CALL FFT2C()
      CALL KE2C()
      CALL BFT2C()
      CALL SP2C()

      PHI_TEMP(:,1) = PHI(:,1)

!equations for real cc
      PHI(:,1) = PHI(:,1)*COS(CC*DT) - CI*SIN(CC*DT)*PHI(:,2)
      PHI(:,2) = PHI(:,2)*COS(CC*DT) - CI*SIN(CC*DT)*PHI_TEMP(:,1)

!equations for complex cc
      !PHI(:,1) = PHI(:,1)*COS(CC*DT) - CI*(CC/ABS(CC))*SIN(ABS(CC)*DT)*PHI(:,2)
      !PHI(:,2) = PHI(:,2)*COS(CC*DT) - CI*(CONJG(CC)/ABS(CC))*SIN(ABS(CC)*DT)*PHI_TEMP(:,1)

      CALL NORM2T(PHI, NORMT)

      PHI(:,1) = (PHI(:,1)/SQRT(NORMT))*sqrt(NATOMS)
      PHI(:,2) = (PHI(:,2)/SQRT(NORMT))*sqrt(NATOMS)

      IF(MOD(II,STP).EQ.0)THEN
      CALL ENERGY2C(PHI, MU, EN)
      CALL RAD2C(PHI, RMS)
       IF(SWITCH_IM.EQ.1)THEN
         CONV = MAXVAL(ABS(PHI-PHI_OLD))/(2.0D0*DT)
         WRITE(9,*) II*DT, CONV
         IF(CONV.LE.TOL) EXIT
       END IF

      WRITE(3,'(F14.6, 4F16.8)') II*DT,  EN/2.0D0, (RMS(K), K = 1, 2)
      CALL NORM2C(PHI, NORM)
      write(100,*) NORM(1)-NORM(2)
      END IF
      PHI_OLD = PHI

      IF(MOD(II,NSV).EQ.0)THEN
           do i = 1, nx
           write(200 + (II/NSV), '(5f12.4)') x(i), (abs(PHI(I, 1)))**2, &
           ATAN2(AIMAG(PHI(I, 1)),REAL(PHI(I, 1))), (abs(PHI(I, 2)))**2, &
           ATAN2(AIMAG(PHI(I, 2)),REAL(PHI(I, 2)))
        end do
STATUS='replace',FORM='FORMATTED',ACTION='WRITE')
      END IF
  END DO

  CALL DESTROY_PLANS()
```

```
  CALL RAD2C(PHI, RMS)

  WRITE (2, 1001)
  WRITE (2, 1006) II-1, SUM(NORM), EN, (MU(K), K = 1, 2), (ABS(PHI(NX2, K)), K = 1, 2)
  1005 FORMAT('After NSTP iter.:', 1F7.4, 3F12.5, 2F12.5)
  1006 FORMAT('After  ', I8, ' iter.:', 1F7.4, 3F12.5, 2F12.5)
  WRITE (2, 1001)
  WRITE(2,*)

     DO I = 1, NX
       WRITE(8,'(5f12.4)') X(I), (ABS(PHI(I, K))**2, &
        ATAN2(AIMAG(PHI(I, K)),REAL(PHI(I, K))), K = 1, 2)
     END DO
  PRINT *,'Program execution complete'

  CALL CPU_TIME(FINISH)
  WRITE(2,1009) (FINISH-START)/60

  1007 FORMAT("Started on DAY/MONTH/YEAR, HOURS:MINUTES:SECONDS = ",I2,'/',I2,'/',I4,',',I3,':',I2,'
  1008 FORMAT("Ended on DAY/MONTH/YEAR, HOURS:MINUTES:SECONDS = ",I2,'/',I2,'/',I4,',',I3,':',I2,':'
  1009 FORMAT("Time elapsed = ", F18.8, "  min")
END PROGRAM CGPE2D

SUBROUTINE INITIALIZE2C()
  USE BASIC_DATA, ONLY : PI, NX, NX2, LX, DX, CI
  USE CGPE_DATA, ONLY : X, X2, R2, V, KX, PHI, PHA, PHB, U, XIS, NATOMS, RMOD, RPH
  IMPLICIT NONE
  INTEGER :: I, J
  DO I = 1, 1+NX/2
     KX(I) = (I-1.0d0)*2.0D0*PI/LX
  END DO
  DO I = 1,NX/2 -1
     KX(I+1+NX/2) = -KX(1-I+NX/2)
  END DO

   DO I = 1, NX
     X(I) = (-1.0d0 +2.0D0*(I-1.0D0)/NX)*LX/2.0D0
     X2(I) = X(I)*X(I)
  END DO

    DO I = 1,NX
     R2(I) = X2(I)
     !Homogeneous
     V(I,1) = 2500.0D0*(TANH(4*X(I)-1.7578D0*DX*NX) - TANH(4*X(I)+ 1.7578D0*DX*NX)) + 5000.0D0
     V(I,2) = 2500.0D0*(TANH(4*X(I)-1.7578D0*DX*NX) - TANH(4*X(I)+ 1.7578D0*DX*NX)) + 5000.0D0
```

```
! imprint static magnetic soliton
     !PHI(I, 1) = PHI(I,1)*SQRT((1 - 1/COSH((X(I))/XIS))) * EXP(CI*PI/4)
     !PHI(I, 2) = PHI(I,2)*SQRT((1 + 1/COSH((X(I))/XIS))) * EXP(CI*PI/4)
     !IF (X(I) > 0.0) THEN
!PHI(I, 1) = PHI(I,1)*EXP(-CI*PI)
     !END IF

        ! imprint moving miscible soliton

     !PHA(I) = ATAN2(-U,SINH(X(I)/XIS*SQRT(1-U*U)))
     !PHB(I) = ATAN2(-SQRT(1-U*U)*TANH(X(I)/XIS*SQRT(1-U*U)),U) - ATAN(SQRT(1-U**2)/U)
     !PHI(I, 2) = PHI(I,2) * SQRT((1 - SQRT(1-U*U)/COSH(X(I)/XIS*SQRT(1-U*U)))) &
      * EXP(CI*(PHB(I)-PHA(I))/2)
     !PHI(I, 1) = PHI(I,1) * SQRT((1 + SQRT(1-U*U)/COSH(X(I)/XIS*SQRT(1-U*U)))) &
      * EXP(CI*(PHB(I)+PHA(I))/2)

   END DO
END SUBROUTINE INITIALIZE2C

SUBROUTINE CREATE_PLANS()
  USE BASIC_DATA
  USE FFTW3
  USE FFTW_DATA

  IMPLICIT NONE
   PLANFX = fftw_plan_dft_1d(NX,fftfx,fftbx,FFTW_FORWARD, FFTW_ESTIMATE)
  PLANBX = fftw_plan_dft_1d(NX,fftbx,fftfx,FFTW_BACKWARD,FFTW_ESTIMATE)
END SUBROUTINE CREATE_PLANS

SUBROUTINE DESTROY_PLANS()
  USE FFTW3
  USE FFTW_DATA

  IMPLICIT NONE
  call fftw_DESTROY_PLAN(planfx)
  call fftw_DESTROY_PLAN(planbx)
END SUBROUTINE DESTROY_PLANS

SUBROUTINE KE2C()
  USE BASIC_DATA, ONLY : CI, NX, CDT
  USE CGPE_DATA, ONLY :  PHIF, KX

  IMPLICIT NONE
  INTEGER :: I

     DO I = 1, NX
```

```
       PHIF(I, 1) = exp(-CI*CDT*0.5D0*(KX(I)*KX(I)))*PHIF(I, 1)
       PHIF(I, 2) = exp(-CI*CDT*0.5D0*(KX(I)*KX(I)))*PHIF(I, 2)
     END DO
END SUBROUTINE KE2C

SUBROUTINE SP2C()
  USE BASIC_DATA, ONLY : CI, NX, CDT
  USE CGPE_DATA, ONLY : X2,  V, G11, G22, G12, G21, PHI, DETUN, X

  IMPLICIT NONE
  REAL (8), DIMENSION(1:2) :: TMP
  !REAL (8), DIMENSION(1:NX,NY) :: RHO, FZ
  INTEGER :: I, J

     DO I = 1, NX
        TMP(1) = (V(I,1) - DETUN + G11*ABS(PHI(I, 1))**2  + G12*ABS(PHI(I, 2))**2)
        TMP(2) = (V(I,2) + DETUN + G22*ABS(PHI(I, 2))**2  + G21*ABS(PHI(I, 1))**2)
        PHI(I, 1) = PHI(I, 1)*EXP((-CI*CDT)*TMP(1))
        PHI(I, 2) = PHI(I, 2)*EXP((-CI*CDT)*TMP(2))
     END DO
END SUBROUTINE SP2C

SUBROUTINE NORM2C(PHI, NORM)
  USE BASIC_DATA, ONLY : NX, DX

  IMPLICIT NONE
  COMPLEX (8), DIMENSION(1:NX,1:2), INTENT(IN) :: PHI
  REAL (8), DIMENSION(1:2), INTENT(OUT) :: NORM

  INTERFACE
    PURE FUNCTION SIMP(F, DX)
      IMPLICIT NONE
      REAL (8), DIMENSION(1:), INTENT(IN) :: F
      REAL (8), INTENT(IN) :: DX
      REAL (8) :: SIMP
    END FUNCTION SIMP
  END INTERFACE
  INTEGER :: I, J, K
  REAL (8), DIMENSION(1:NX) :: P1, P2
  REAL (8), DIMENSION(1:NX) :: TMP1D1, TMP1D2

  DO I = 1, NX
      P1(I) = ABS(PHI(I, 1))**2
      P2(I) = ABS(PHI(I, 2))**2
  END DO
```

```
  DO I = 1, NX
     TMP1D1(I) = P1(I)
     TMP1D2(I) = P2(I)
  END DO
  NORM(1) = SIMP(TMP1D1, DX)
  NORM(2) = SIMP(TMP1D2, DX)

END SUBROUTINE NORM2C


SUBROUTINE NORM2T(PHI, NORMT)
  USE BASIC_DATA, ONLY : NX, DX

  IMPLICIT NONE
  COMPLEX (8), DIMENSION(1:NX,1:2), INTENT(IN) :: PHI
  REAL (8),  INTENT(OUT) :: NORMT

  INTERFACE
    PURE FUNCTION SIMP(F, DX)
      IMPLICIT NONE
      REAL (8), DIMENSION(1:), INTENT(IN) :: F
      REAL (8), INTENT(IN) :: DX
      REAL (8) :: SIMP
    END FUNCTION SIMP
  END INTERFACE
  INTEGER :: I, J, K
  REAL (8), DIMENSION(1:NX) :: P1, P2
  REAL (8), DIMENSION(1:NX) :: TMP1D1, TMP1D2

  DO I = 1, NX
      P1(I) = ABS(PHI(I, 1))**2
      P2(I) = ABS(PHI(I, 2))**2
  END DO

  DO I = 1, NX
     TMP1D1(I) = P1(I) + P2(I)
  END DO
  NORMT = SIMP(TMP1D1, DX)

END SUBROUTINE NORM2T

SUBROUTINE RAD2C(PHI, RMS)
  USE BASIC_DATA, ONLY : NX, DX
  USE CGPE_DATA, ONLY : X2

  IMPLICIT NONE
```

```
  COMPLEX (8), DIMENSION(1:NX, 1:2), INTENT(IN) :: PHI
  REAL (8), DIMENSION(1:2), INTENT(OUT) :: RMS

  INTERFACE
    PURE FUNCTION SIMP(F, DX)
      IMPLICIT NONE
      REAL (8), DIMENSION(1:), INTENT(IN) :: F
      REAL (8), INTENT(IN) :: DX
      REAL (8) :: SIMP
    END FUNCTION SIMP
  END INTERFACE

  INTEGER :: I, J, K
  REAL (8), DIMENSION(1:NX) :: TMP2D1, TMP2D2
  REAL (8), DIMENSION(1:NX) :: TMP1D1, TMP1D2

     DO I = 1, NX
        TMP2D1(I) = (X2(I))*ABS(PHI(I,1))**2
        TMP2D2(I) = (X2(I))*ABS(PHI(I,2))**2
     END DO

  DO I = 1, NX
     TMP1D1(I) = TMP2D1(I)
     TMP1D2(I) = TMP2D2(I)
  END DO

  RMS(1) = SQRT(SIMP(TMP1D1, DX))
  RMS(2) = SQRT(SIMP(TMP1D2, DX))

END SUBROUTINE RAD2C

SUBROUTINE ENERGY2C(PHI, MU, EN)
  USE BASIC_DATA, ONLY : NX, NXX, DX, CI
  USE CGPE_DATA, ONLY : X, V, G11, G22, G12, G21, CC

  IMPLICIT NONE
  COMPLEX (8), DIMENSION(1:NX, 1:2), INTENT(INOUT) :: PHI
  REAL (8), DIMENSION(1:2), INTENT(OUT) :: MU
  REAL (8), INTENT(OUT) ::  EN

  INTERFACE
    PURE FUNCTION DIFF(P, DX) RESULT (DP)
      IMPLICIT NONE
      REAL (8), DIMENSION(1:), INTENT(IN) :: P
      REAL (8), INTENT(IN) :: DX
      REAL (8), DIMENSION(1:SIZE(P)) :: DP
```

```
    END FUNCTION DIFF
  END INTERFACE

  INTERFACE
    PURE FUNCTION SIMP(F, DX)
      IMPLICIT NONE
      REAL (8), DIMENSION(1:), INTENT(IN) :: F
      REAL (8), INTENT(IN) :: DX
      REAL (8) :: SIMP
    END FUNCTION SIMP

    SUBROUTINE NORM2C(PHI, NORM)
      USE BASIC_DATA, ONLY : NX
      IMPLICIT NONE
      COMPLEX (8), DIMENSION(1:NX, 1:2), INTENT(IN) :: PHI
      REAL (8), DIMENSION(1:2), INTENT(OUT) :: NORM
    END  SUBROUTINE NORM2C
  END INTERFACE
!---------------------------------------------------------------------

  INTEGER :: I, J, K
  REAL (8), DIMENSION(1:NX, 1:2) :: DP2
  REAL (8), DIMENSION(1:NX) :: TMP2D1 ,TMP2D2, TMP2D3
  REAL (8), DIMENSION(1:NX) :: TMP1D1, TMP1D2, TMP1D3
  REAL (8), DIMENSION(1:2) :: NORM

  CALL NORM2C(PHI, NORM)

  DP2(:, 1) = 0.5D0 * (DIFF(REAL(PHI(:, 1)), DX)**2 + DIFF(AIMAG(PHI(:, 1)), DX)**2)
  DP2(:, 2) = 0.5D0 * (DIFF(REAL(PHI(:, 2)), DX)**2 + DIFF(AIMAG(PHI(:, 2)), DX)**2)

   TMP2D1(:)  = V(:,1)*ABS(PHI(:,1))**2 + V(:,2)*ABS(PHI(:,2))**2 + G11*ABS(PHI(:,1))**4/2.0D0&
                        + G22*ABS(PHI(:,2))**4/2.0D0 + G12*ABS(PHI(:,1))**2*ABS(PHI(:,2))**2&
                        + DP2(:,1) + DP2(:,2) - CC*real(PHI(:,2)*CONJG(PHI(:,1))) &
                         - CC*real(PHI(:,1)*CONJG(PHI(:,2)))

   TMP2D2(:)  = V(:,1)*ABS(PHI(:,1))**2 + G11*ABS(PHI(:,1))**4  +&
                         G12*ABS(PHI(:,1))**2*ABS(PHI(:,2))**2 + DP2(:,1) &
 + CC*CONJG(PHI(:,1))*PHI(:,2)

   TMP2D3(:)  = V(:,2)*ABS(PHI(:,2))**2 + G22*ABS(PHI(:,2))**4  +&
                         G12*ABS(PHI(:,2))**2*ABS(PHI(:,1))**2 + DP2(:,2) &
   + CC*CONJG(PHI(:,2))*PHI(:,1)

  EN = SIMP(TMP2D1, DX)/SUM(NORM)
  MU(1) =  SIMP(TMP2D2,DX)/NORM(1)
```

```
  MU(2) =  SIMP(TMP2D3,DX)/NORM(2)

END SUBROUTINE ENERGY2C

PURE FUNCTION SIMP(F, DX)
  IMPLICIT NONE
  REAL (8), DIMENSION(1:), INTENT(IN) :: F
  REAL (8), INTENT(IN) :: DX
  REAL (8) :: SIMP
  REAL (8) :: F1, F2
  INTEGER :: I, N
  N = SIZE(F)  !N is even
  F1 = F(2) + F(N-4)
  F2 = F(3)
  DO I = 4, N-6, 2
     F1 = F1 + F(I)
     F2 = F2 + F(I+1)
  END DO
  SIMP = DX*(F(1) + 4.0D0*F1 + 2.0D0*F2 + F(N-3))/3.0D0+&
         3.0D0*DX*(F(N-3) + 3.0D0*(F(N-2)+F(N-1)) + F(N))/8.0D0
END FUNCTION SIMP

PURE FUNCTION DIFF(P,DX)
  IMPLICIT NONE
  REAL (8), DIMENSION(1:), INTENT(IN) :: P
  REAL (8), INTENT(IN) :: DX
  REAL (8), DIMENSION(1:SIZE(P)) :: DIFF
  INTEGER :: I, N
  N = SIZE(P)
  DIFF(1) = 0.0D0
  !DIFF(1) = (-3.0D0*P(1) + 4.0D0*P(2)-P(3))/(2.0D0*DX)
  DIFF(2) = (P(3) - P(1))/(2.0D0*DX)
  ! 5 point formula to calculate first order derivative at edges
  FORALL(I=3:4)
    DIFF(I) = (P(I-2)-8.0D0*P(I-1)+8.0D0*P(I+1)-P(I+2))/(12.0D0*DX)
  END FORALL
  FORALL(I=N-3:N-2)
    DIFF(I) = (P(I-2)-8.0D0*P(I-1)+8.0D0*P(I+1)-P(I+2))/(12.0D0*DX)
  END FORALL
  ! 9 point formula to calculate first order derivative
  FORALL(I=5:N-4)
    DIFF(I) = (3.0D0*P(I-4)-32.0D0*P(I-3)+168.0D0*P(I-2)-672.0D0*P(I-1)&
+ 672.0D0*P(I+1)-168.0D0*P(I+2)+32.0D0*P(I+3)-3.0D0*P(I+4))/&
              (840.0D0*DX)
  END FORALL
  DIFF(N-1) = (P(N) - P(N-2))/(2.0D0*DX)
```

```
  !DIFF(N) = (P(N-2) - 4.0D0*P(N-1)+3.0D0*P(N))/(2.0D0*DX)
  DIFF(N) = 0.0D0
END FUNCTION DIFF
SUBROUTINE FFT2C()
  USE BASIC_DATA, ONLY : NX
  USE CGPE_DATA
  USE FFTW3 , ONLY : fftw_execute_dft
  USE FFTW_DATA

  IMPLICIT NONE
  INTEGER :: L

  DO L = 1, 2
     FFTFX(:) = PHI(:,L)
     CALL fftw_execute_dft(planfx,FFTFX,FFTBX)
     PHIF(:,L) = FFTBX(:)
  END DO
END SUBROUTINE FFT2C

SUBROUTINE BFT2C()
  USE BASIC_DATA, ONLY : NX
  USE CGPE_DATA
  USE FFTW3 , ONLY : fftw_execute_dft
  USE FFTW_DATA
  IMPLICIT NONE
  INTEGER :: I, J, K, L

  DO L = 1, 2
     FFTBX(:) = PHIF(:,L)
     CALL fftw_execute_dft(planbx,FFTBX,FFTFX)
     PHI(:,L) = FFTFX(:)
        DO I = 1, NX
           PHI(I, L)= PHI(I, L)/REAL(NX)
        END DO
  END DO
END SUBROUTINE BFT2C

END INTERFACE
```

References

[1] L. P. Pitaevskii and S. Stringari. *Bose-Einstein Condensation and Superfluidity*. International Series of Monographs on Physics. Oxford, United Kingdom: Oxford University Press, 2016.

[2] Nick P. Proukakis and Brian Jackson. "Finite-temperature models of Bose?Einstein condensation". In: *J. Phys. B: At. Mol. Opt. Phys.* 41 (Oct. 2008), p. 203002. DOI: 10.1088/0953-4075/41/20/203002. URL: https://iopscience.iop.org/article/10.1088/0953-4075/41/20/203002.

[3] C. J. Pethick and H. Smith. *Bose?Einstein Condensation in Dilute Gases*. Cambridge University Press, 2002.

[4] Alexander L. Gaunt et al. "Bose-Einstein Condensation of Atoms in a Uniform Potential". In: *Phys. Rev. Lett.* 110 (20 May 2013), p. 200406. DOI: 10.1103/PhysRevLett.110.200406. URL: https://link.aps.org/doi/10.1103/PhysRevLett.110.200406.

[5] Marta Abad and Alessio Recati. "A study of coherently coupled two-component Bose-Einstein Condensates". In: *Eur. Phys. J. D* 67 (148 Jan. 2013). DOI: 10.1140/epjd/e2013-40053-2. URL: https://link.springer.com/article/10.1140/epjd/e2013-40053-2.

[6] Paolo Tommasini et al. "Bogoliubov theory for mutually coherent condensates". In: *Phys. Rev. A* 67 (2 Feb. 2003), p. 023606. DOI: 10.1103/PhysRevA.67.023606. URL: https://link.aps.org/doi/10.1103/PhysRevA.67.023606.

[7] A. Smerzi et al. "Quantum Coherent Atomic Tunneling between Two Trapped Bose-Einstein Condensates". In: *Phys. Rev. Lett.* 79 (25 Dec. 1997), pp. 4950–4953. DOI: 10.1103/PhysRevLett.79.4950. URL: https://link.aps.org/doi/10.1103/PhysRevLett.79.4950.

[8] S. Raghavan et al. "Coherent oscillations between two weakly coupled Bose-Einstein condensates: Josephson effects, π oscillations, and macroscopic quantum self-trapping". In: *Phys. Rev. A* 59 (1 Jan. 1999), pp. 620–633. DOI: 10.1103/PhysRevA.59.620. URL: https://link.aps.org/doi/10.1103/PhysRevA.59.620.

[9] Alessio Recati and Sandro Stringari. "Coherently Coupled Mixtures of Ultracold Atomic Gases". In: *Annu. Rev. Con. Mat. Phys.* 13 (Mar. 2022), pp. 407–432. DOI: https://doi.org/10.1146/annurev-conmatphys-031820-121316. URL: https://www.annualreviews.org/content/journals/10.1146/annurev-conmatphys-031820-121316.

[10] S. V. Manakov. "On the theory of two-dimensional stationary self-focusing of electromagnetic waves". In: *Zh. Eksp. Teor. Fiz.* 65 (Aug. 1973), pp. 505–516.

[11] E. M. Lifshitz and L. P. Pitaevskii. *Statistical Physics, Part 2 (Course of Theoretical Physics, volume 9)*. New York: Pergamon Press, 1980.

[12] T. Congy, A. M. Kamchatnov, and N. Pavloff. "Dispersive hydrodynamics of nonlinear polarization waves in two-component Bose-Einstein condensates". In: *SciPost Phys.* 1 (1 2016), p. 006. DOI: 10.21468/SciPostPhys.1.1.006. URL: https://scipost.org/10.21468/SciPostPhys.1.1.006.

[13] A. Farolfi et al. "Quantum-torque-induced breaking of magnetic interfaces in ultracold gases". In: *Nat. Phys.* 17.12 (Dec. 2021), pp. 1359–1363. ISSN: 1745-2481. DOI: 10.1038/s41567-021-01369-y. URL: https://doi.org/10.1038/s41567-021-01369-y.

[14] Chunlei Qu, Lev P. Pitaevskii, and Sandro Stringari. "Magnetic Solitons in a Binary Bose-Einstein Condensate". In: *Phys. Rev. Lett.* 116 (16 Apr. 2016), p. 160402. DOI: 10.1103/PhysRevLett.116.160402. URL: https://link.aps.org/doi/10.1103/PhysRevLett.116.160402.

[15] A. E. Borovik, S. Klama, and Kulinich S. I. “Integration of the Landau-Lifshitz equation with preferred-axis anisotropy by the method of the inverse scattering problem”. In: *Physica D* 32 (1 Aug. 1988), pp. 107–134. DOI: https://doi.org/10.1016/0167-2789(88)90089-9. URL: https://www.sciencedirect.com/science/article/abs/pii/0167278988900899.

[16] Clifford S. Gardner et al. “Method for Solving the Korteweg-deVries Equation”. In: *Phys. Rev. Lett.* 19 (19 Nov. 1967), pp. 1095–1097. DOI: 10.1103/PhysRevLett.19.1095. URL: https://link.aps.org/doi/10.1103/PhysRevLett.19.1095.

[17] Peter D. Lax. “Integrals of nonlinear equations of evolution and solitary waves”. In: *Communications on Pure and Applied Mathematics* 21.5 (1968), pp. 467–490. DOI: https://doi.org/10.1002/cpa.3160210503. eprint: https://onlinelibrary.wiley.com/doi/pdf/10.1002/cpa.3160210503. URL: https://onlinelibrary.wiley.com/doi/abs/10.1002/cpa.3160210503.

[18] V. E. Zakharov and A. B. Shabat. “Exact theory of two-dimensional self-focusing and one-dimensional self-modulation of waves in nonlinear media”. In: *Zh. Eksp. Teor. Fiz.* 61 (July 1971), pp. 118–134. URL: http://jetp.ras.ru/cgi-bin/dn/e_034_01_0062.pdf.

[19] Mark J. Ablowitz et al. “Nonlinear-Evolution Equations of Physical Significance”. In: *Phys. Rev. Lett.* 31 (2 July 1973), pp. 125–127. DOI: 10.1103/PhysRevLett.31.125. URL: https://link.aps.org/doi/10.1103/PhysRevLett.31.125.

[20] Mark J. Ablowitz et al. “The Inverse Scattering Transform-Fourier Analysis for Nonlinear Problems”. In: *Studies in Applied Mathematics* 53.4 (1974), pp. 249–315. DOI: https://doi.org/10.1002/sapm1974534249. eprint: https://onlinelibrary.wiley.com/doi/pdf/10.1002/sapm1974534249. URL: https://onlinelibrary.wiley.com/doi/abs/10.1002/sapm1974534249.

[21] D. T. Son and M. A. Stephanov. “Domain walls of relative phase in two-component Bose-Einstein condensates”. In: *Phys. Rev. A* 65 (6 June 2002), p. 063621. DOI: 10.1103/PhysRevA.65.063621. URL: https://link.aps.org/doi/10.1103/PhysRevA.65.063621.

[22] S. Novikov et al. *Theory of Solitons - the Inverse Scattering Method*. Regional Conference Series in Applied Mathematics. Society for Industrial and Applied Mathematics, 1985.

[23] Alan C. Newell. *Solitons in Mathematics and Physics*. Regional Conference Series in Applied Mathematics. Society for Industrial and Applied Mathematics, 1985.

[24] Yuri S. Kivshar and Boris A. Malomed. “Dynamics of solitons in nearly integrable systems”. In: *Rev. Mod. Phys.* 61 (4 Oct. 1989), pp. 763–915. DOI: 10.1103/RevModPhys.61.763. URL: https://link.aps.org/doi/10.1103/RevModPhys.61.763.

[25] P. G. Kevrekidis et al. “Families of matter-waves in two-component Bose-Einstein condensates”. In: *Eur. Phys. J. D* 28 (Feb. 2004), pp. 181–185. DOI: https://doi.org/10.1140/epjd/e2003-00311-6. URL: https://link.springer.com/article/10.1140/epjd/e2003-00311-6#citeas.

[26] A. M. Kamchatnov et al. “Nonlinear polarization waves in a two-component Bose-Einstein condensate”. In: *Phys. Rev. A* 89 (3 Mar. 2014), p. 033618. DOI: 10.1103/PhysRevA.89.033618. URL: https://link.aps.org/doi/10.1103/PhysRevA.89.033618.

[27] B. A. Ivanov, A. M. Kosevich, and I. V. Manzhos. “Algebraic soliton in a ferromagnet in the presence of the magnetic field directed along the anisotropy axis”. In: *Solid State Communications* 34 (6 May 1980), pp. 417–418. DOI: https://doi.org/10.1016/0038-1098(80)90640-7. URL: https://www.sciencedirect.com/science/article/pii/0038109880906407.

[28] I. M. Babick and A. M. Kosevich. "Nonlinear two-parameter excitations in an anisotropic ferromagnet". In: *Zh. Eksp. Teor. Fiz.* 82 (4 Apr. 1982), p. 127. URL: http://jetp.ras.ru/cgi-bin/e/index/e/55/4/p743?a=list.

[29] V. S. Gerdzhikov and P. P. Kulish. "Multicomponent nonlinear Schrödinger equation in the case of nonzero boundary conditions". In: *J Math Sci* 30 (Aug. 1985), pp. 2261–2269. DOI: https://doi.org/10.1007/BF02105343. URL: https://link.springer.com/article/10.1007/BF02105343.

[30] Yuri S. Kivshar and Barry Luther-Davies. "Dark optical solitons: physics and applications". In: *Physics Reports* 298 (2-3 May 1998), pp. 81–197. DOI: https://doi.org/10.1016/S0370-1573(97)00073-2. URL: https://www.sciencedirect.com/science/article/pii/S0370157397000732.

[31] Gino Biondini Barbara Prinari Mark J. Ablowitz. "Inverse scattering transform for the vector nonlinear Schrödinger equation with nonvanishing boundary conditions". In: *J. Math. Phys.* 47 (6 June 2006), p. 063508. DOI: https://doi.org/10.1063/1.2209169. URL: https://pubs.aip.org/aip/jmp/article/47/6/063508/897930/Inverse-scattering-transform-for-the-vector.

[32] Deng-Shan Wang; Da-Jun Zhang; Jianke Yang. "Integrable properties of the general coupled nonlinear Schrödinger equations". In: *J. Math. Phys.* 51 (Feb. 2010), p. 023510. DOI: https://doi.org/10.1063/1.3290736. URL: https://pubs.aip.org/aip/jmp/article/51/2/023510/928280/Integrable-properties-of-the-general-coupled.

[33] Barbara Prinari; Federica Vitale; Gino Biondini. "Dark-bright soliton solutions with nontrivial polarization interactions for the three-component defocusing nonlinear Schrödinger equation with nonzero boundary conditions". In: *J. Math. Phys.* 56 (July 2015), p. 071505. DOI: https://doi.org/10.1063/1.4926439. URL: https://pubs.aip.org/aip/jmp/article/56/7/071505/908830/Dark-bright-soliton-solutions-with-nontrivial.

[34] Gino Biondini and Daniel Kraus. "Inverse Scattering Transform for the Defocusing Manakov System with Nonzero Boundary Conditions". In: *SIAM Journal on Mathematical Analysis* 47.1 (2015), pp. 706–757. DOI: 10.1137/130943479.

[35] Gino Biondini Daniel Kraus and Gregor Kovačič. "The focusing Manakov system with nonzero boundary conditions". In: *Nonlinearity* 28 (9 Aug. 2015), p. 3101. DOI: 10.1088/0951-7715/28/9/3101. URL: https://iopscience.iop.org/article/10.1088/0951-7715/28/9/3101.

[36] Toshio Tsuzuki. "Nonlinear waves in the Pitaevskii-Gross equation". In: *J Low Temp Phys* 4 (1971), pp. 441–457. DOI: 10.1007/BF00628744. URL: https://link.springer.com/article/10.1007/BF00628744.

[37] A.M. Kosevich, B.A. Ivanov, and A.S. Kovalev. "Magnetic Solitons". In: *Phys. Rep.* 194.3 (1990), pp. 117–238. ISSN: 0370-1573. DOI: https://doi.org/10.1016/0370-1573(90)90130-T. URL: https://www.sciencedirect.com/science/article/pii/037015739090130T.

[38] Felix Bloch. "Über die Quantenmechanik der Elektronen in Kristallgittern". In: *Z. Physik* 52.7 (July 1929), pp. 555–600. ISSN: 0044-3328. DOI: 10.1007/BF01339455. URL: https://doi.org/10.1007/BF01339455.

[39] B.D. Josephson. "Possible new effects in superconductive tunnelling". In: *Physics Letters* 1.7 (1962), pp. 251–253. ISSN: 0031-9163. DOI: https://doi.org/10.1016/0031-9163(62)91369-0. URL: https://www.sciencedirect.com/science/article/pii/0031916362913690.

[40] Aron J Beekman. "Theory of generalized Josephson effects". In: *Prog. Theor. Exp. Phys.* 2020 (7 July 2020), 073B09. ISSN: 2050-3911. DOI: 10.1093/ptep/ptaa088. URL: https://doi.org/10.1093/ptep/ptaa088.

[41] O. Avenel and E. Varoquaux. "Josephson effect and quantum phase slippage in superfluids". In: *Phys. Rev. Lett.* 60 (5 Feb. 1988), pp. 416–419. DOI: 10.1103/PhysRevLett.60.416. URL: https://link.aps.org/doi/10.1103/PhysRevLett.60.416.

[42] S. V. Pereverzev et al. "Quantum oscillations between two weakly coupled reservoirs of superfluid ^{3}He". In: *Nature (London)* 388 (1997), pp. 449–451. DOI: 10.1038/41277.

[43] Kalyani Sukhatme et al. "Observation of the ideal Josephson effect in superfluid ^{4}He". In: *Nature (London)* 411 (2001), pp. 280–283. URL: https://doi.org/10.1038/35077024.

[44] F. S. Cataliotti et al. "Josephson Junction Arrays with Bose-Einstein Condensates". In: *Science* 293.5531 (2001), pp. 843–846. DOI: 10.1126/science.1062612. URL: https://www.science.org/doi/abs/10.1126/science.1062612.

[45] Michael Albiez et al. "Direct Observation of Tunneling and Nonlinear Self-Trapping in a Single Bosonic Josephson Junction". In: *Phys. Rev. Lett.* 95 (1 June 2005), p. 010402. DOI: 10.1103/PhysRevLett.95.010402. URL: https://link.aps.org/doi/10.1103/PhysRevLett.95.010402.

[46] S. Levy et al. "The a.c. and d.c. Josephson effects in a Bose-Einstein condensate". In: *Nature (London)* 449 (2007), pp. 579–583. DOI: 10.1038/nature06186.

[47] Kouki Nakata et al. "Josephson and persistent spin currents in Bose-Einstein condensates of magnons". In: *Phys. Rev. B* 90 (14 Oct. 2014), p. 144419. DOI: 10.1103/PhysRevB.90.144419. URL: https://link.aps.org/doi/10.1103/PhysRevB.90.144419.

[48] K. G. Lagoudakis et al. "Coherent Oscillations in an Exciton-Polariton Josephson Junction". In: *Phys. Rev. Lett.* 105 (12 Sept. 2010), p. 120403. DOI: 10.1103/PhysRevLett.105.120403. URL: https://link.aps.org/doi/10.1103/PhysRevLett.105.120403.

[49] A. V. Markelov. "Josephson effect on a spin current". In: *Sov. Phys. JETP* 67 (1988), pp. 520–523. URL: http://www.jetp.ras.ru/cgi-bin/e/index/e/67/3/p520?a=list.

[50] A. S. Borovik-Romanov et al. "Observation of a spin-current analog of the Josephson effect". In: *JETP Lett.* 47 (1988), p. 478. URL: http://jetpletters.ru/ps/1095/article_16545.shtml.

[51] F. S Nogueira and K.-H Bennemann. "Spin Josephson effect in ferromagnet/ferromagnet tunnel junctions". In: *EPL* 67.4 (Aug. 2004), pp. 620–626. DOI: 10.1209/epl/i2003-10305-x. URL: https://doi.org/10.1209/epl/i2003-10305-x.

[52] H. Chen and A. H. MacDonald. "Spin-Superfluidity and Spin-Current Mediated Nonlocal Transport". In: *Universal Themes of Bose-Einstein Condensation*. Ed. by Nick P. Proukakis, David W. Snoke, and Peter B.Editors Littlewood. Cambridge University Press, 2017, pp. 525–548. DOI: 10.1017/9781316084366.029.

[53] A. M. Kosevich. "Bloch oscillations of magnetic solitons as an example of dynamical localization of quasiparticles in a uniform external field". In: *Low Temp. Phys.* 27.7 (2001), pp. 513–541. DOI: 10.1063/1.1388415. URL: https://doi.org/10.1063/1.1388415.

[54] A. M. Kosevich et al. "Magnetic soliton motion in a nonuniform magnetic field". In: *J. Exp. Theor. Phys.* 87 (1998), pp. 401–407. URL: https://doi.org/10.1134/1.558674.

[55] Li-Chen Zhao et al. “Spin soliton with a negative-positive mass transition”. In: *Phys. Rev. A* 101 (4 Apr. 2020), p. 043621. DOI: 10.1103/PhysRevA.101.043621. URL: https://link.aps.org/doi/10.1103/PhysRevA.101.043621.

[56] Xiaoquan Yu and P. B. Blakie. “Propagating Ferrodark Solitons in a Superfluid: Exact Solutions and Anomalous Dynamics”. In: *Phys. Rev. Lett.* 128 (12 Mar. 2022), p. 125301. DOI: 10.1103/PhysRevLett.128.125301. URL: https://link.aps.org/doi/10.1103/PhysRevLett.128.125301.

[57] M. Schecter, D.M. Gangardt, and A. Kamenev. “Dynamics and Bloch oscillations of mobile impurities in one-dimensional quantum liquids”. In: *Ann. Phys. (N.Y.)* 327.3 (2012), pp. 639–670. ISSN: 0003-4916. DOI: https://doi.org/10.1016/j.aop.2011.10.001. URL: https://www.sciencedirect.com/science/article/pii/S0003491611001618.

[58] Florian Meinert et al. “Bloch oscillations in the absence of a lattice”. In: *Science* 356.6341 (2017), pp. 945–948. DOI: 10.1126/science.aah6616. URL: https://www.science.org/doi/abs/10.1126/science.aah6616.

[59] Michael Schecter, Dimitri M. Gangardt, and Alex Kamenev. “Quantum impurities: from mobile Josephson junctions to depletons”. In: *New J. Phys.* 18.6 (May 2016), p. 065002. DOI: 10.1088/1367-2630/18/6/065002. URL: https://doi.org/10.1088/1367-2630/18/6/065002.

[60] O. Gamayun, O. Lychkovskiy, and V. Cheianov. “Kinetic theory for a mobile impurity in a degenerate Tonks-Girardeau gas”. In: *Phys. Rev. E* 90 (3 Sept. 2014), p. 032132. DOI: 10.1103/PhysRevE.90.032132. URL: https://link.aps.org/doi/10.1103/PhysRevE.90.032132.

[61] Michael Schecter, Dimitri M. Gangardt, and Alex Kamenev. “Comment on "Kinetic theory for a mobile impurity in a degenerate Tonks-Girardeau gas"”. In: *Phys. Rev. E* 92 (1 July 2015), p. 016101. DOI: 10.1103/PhysRevE.92.016101. URL: https://link.aps.org/doi/10.1103/PhysRevE.92.016101.

[62] O. Gamayun, O. Lychkovskiy, and V. Cheianov. “Reply to “Comment on ‘Kinetic theory for a mobile impurity in a degenerate Tonks-Girardeau gas’ ””. In: *Phys. Rev. E* 92 (1 July 2015), p. 016102. DOI: 10.1103/PhysRevE.92.016102. URL: https://link.aps.org/doi/10.1103/PhysRevE.92.016102.

[63] Tilman Zibold et al. “Classical Bifurcation at the Transition from Rabi to Josephson Dynamics”. In: *Phys. Rev. Lett.* 105 (20 Nov. 2010), p. 204101. DOI: 10.1103/PhysRevLett.105.204101. URL: https://link.aps.org/doi/10.1103/PhysRevLett.105.204101.

[64] S. Giovanazzi, A. Smerzi, and S. Fantoni. “Josephson Effects in Dilute Bose-Einstein Condensates”. In: *Phys. Rev. Lett.* 84 (20 May 2000), pp. 4521–4524. DOI: 10.1103/PhysRevLett.84.4521. URL: https://link.aps.org/doi/10.1103/PhysRevLett.84.4521.

[65] L. P. Pitaevskii. “Dynamics of solitary waves in ultracold gases in terms of observable quantities”. In: *Phys.-Usp.* 59.10 (Oct. 2016), pp. 1028–1033. DOI: 10.3367/ufne.2016.08.037891. URL: https://doi.org/10.3367/ufne.2016.08.037891.

[66] A. Sartori and A. Recati. “Dynamics of highly unbalanced Bose-Bose mixtures: miscible vs. immiscible gases”. In: *Eur. Phys. J. D* 67 (2013), p. 260. URL: https://doi.org/10.1140/epjd/e2013-40635-x.

[67] C. A. Jones and P. H. Roberts. “Motions in a Bose condensate. IV. Axisymmetric solitary waves”. In: *J. Phys. A: Math. Gen.* 15.8 (Aug. 1982), pp. 2599–2619. DOI: 10.1088/0305-4470/15/8/036. URL: https://doi.org/10.1088/0305-4470/15/8/036.

[68] S. I. Shevchenko. “On quasi-one-dimensional superfluidity in Bose systems”. In: *Sov. J. Low Temp. Phys.* 14 (1988). [Fiz. Nizk. Temp. **14**, 1011 (1988)], p. 553.

[69] K. K. Likharev. “Superconducting weak links”. In: *Rev. Mod. Phys.* 51 (1 Jan. 1979), pp. 101–159. DOI: 10.1103/RevModPhys.51.101. URL: https://link.aps.org/doi/10.1103/RevModPhys.51.101.

[70] Chiara Menotti and Sandro Stringari. “Collective oscillations of a one-dimensional trapped Bose-Einstein gas”. In: *Phys. Rev. A* 66 (4 Oct. 2002), p. 043610. DOI: 10.1103/PhysRevA.66.043610. URL: https://link.aps.org/doi/10.1103/PhysRevA.66.043610.

[71] A. Gallemı et al. “Magnetic defects in an imbalanced mixture of two Bose-Einstein condensates”. In: *Phys. Rev. A* 97 (6 June 2018), p. 063615. DOI: 10.1103/PhysRevA.97.063615. URL: https://link.aps.org/doi/10.1103/PhysRevA.97.063615.

[72] A. Recati, N. Pavloff, and I. Carusotto. “Bogoliubov theory of acoustic Hawking radiation in Bose-Einstein condensates”. In: *Phys. Rev. A* 80 (4 Oct. 2009), p. 043603. DOI: 10.1103/PhysRevA.80.043603. URL: https://link.aps.org/doi/10.1103/PhysRevA.80.043603.

[73] S. K. Ivanov and A. M. Kamchatnov. “Motion of dark solitons in a non-uniform flow of Bose-Einstein condensate”. In: *Chaos* 32 (Nov. 2022), p. 113142. DOI: https://doi.org/10.1063/5.0123514. URL: https://pubs.aip.org/aip/cha/article/32/11/113142/2836057/Motion-of-dark-solitons-in-a-non-uniform-flow-of?pdfCoverIconEvent=cite.

[74] U. Al. Khawaja and H. T. C. Stoof. “Formation of matter-wave soliton molecules”. In: *New J. Phys.* 13 (Aug. 2011), p. 085003. DOI: 10.1088/1367-2630/13/8/085003. URL: https://iopscience.iop.org/article/10.1088/1367-2630/13/8/085003.

[75] J. P. Gordon. “Interaction forces among solitons in optical fibers”. In: *Opt. Lett.* 8 (11 Nov. 1983), pp. 596–598. DOI: 10.1364/OL.8.000596. URL: https://opg.optica.org/ol/abstract.cfm?uri=ol-8-11-596&origin=search.

[76] Gang Xu et al. “Breather Wave Molecules”. In: *Phys. Rev. Lett.* 122 (8 Feb. 2019), p. 084101. DOI: 10.1103/PhysRevLett.122.084101. URL: https://link.aps.org/doi/10.1103/PhysRevLett.122.084101.

[77] Tetsuji Ueda and William L. Kath. “Dynamics of coupled solitons in nonlinear optical fibers”. In: *Phys. Rev. A* 42 (1 July 1990), pp. 563–571. DOI: 10.1103/PhysRevA.42.563. URL: https://link.aps.org/doi/10.1103/PhysRevA.42.563.

[78] Jianke Yang. “Vector Solitons and Their Internal Oscilliations in Birefringent Nonlinear Optical Fibers”. In: *Studies in Applied Mathematics* 98.1 (1997), pp. 61–97. DOI: https://doi.org/10.1111/1467-9590.00041. eprint: https://onlinelibrary.wiley.com/doi/pdf/10.1111/1467-9590.00041. URL: https://onlinelibrary.wiley.com/doi/abs/10.1111/1467-9590.00041.

[79] Michael Peyrard and David K. Campbell. “Kink-antikink interactions in a modified sine-Gordon model”. In: *Physica D* 9 (1-2 Oct. 1983), pp. 33–51. DOI: 10.1016/0167-2789(83)90290-7. URL: https://www.sciencedirect.com/science/article/abs/pii/0167278983902907.

[80] David K. Campbell, Jonathan F. Schonfeld, and Charles A. Wingate. “Resonance structure in kink-antikink interactions in φ^4 theory”. In: *Physica D* 9 (1-2 Oct. 1983), pp. 1–32. DOI: 10.1016/0167-2789(83)90289-0. URL: https://www.sciencedirect.com/science/article/abs/pii/0167278983902890.

[81] Tamara I. Belova and Aleksandr E. Kudryavtsev. "Solitons and their interactions in classical field theory". In: *Physics-Uspekhi* 40 (1997), p. 359. DOI: 10.1070/PU1997v040n04ABEH000227. URL: https://iopscience.iop.org/article/10.1070/PU1997v040n04ABEH000227.

[82] Jianke Yang and Yu Tan. "Fractal Structure in the Collision of Vector Solitons". In: *Phys. Rev. Lett.* 85 (17 Oct. 2000), pp. 3624–3627. DOI: 10.1103/PhysRevLett.85.3624. URL: https://link.aps.org/doi/10.1103/PhysRevLett.85.3624.

[83] Sergey D. Dmitriev and Takeshi Shigenari. "Short-lived two-soliton bound states in weakly perturbed nonlinear Schrödinger equation". In: *Chaos* 12 (2 June 2002), pp. 324–331. DOI: https://doi.org/10.1063/1.1476951. URL: https://pubs.aip.org/aip/cha/article/12/2/324/134864/Short-lived-two-soliton-bound-states-in-weakly.

[84] Sergey V. Dmitriev, Panayotis G. Kevrekidis, and Yuri S. Kivshar. "Radiationless energy exchange in three-soliton collisions". In: *Phys. Rev. E* 78 (4 Oct. 2008), p. 046604. DOI: 10.1103/PhysRevE.78.046604. URL: https://link.aps.org/doi/10.1103/PhysRevE.78.046604.

[85] Vakhid A. Gani, Alexander E. Kudryavtsev, and Mariya A. Lizunova. "Kink interactions in the (1+1)-dimensional φ^6 model". In: *Phys. Rev. D* 89 (12 June 2014), p. 125009. DOI: 10.1103/PhysRevD.89.125009. URL: https://link.aps.org/doi/10.1103/PhysRevD.89.125009.

[86] A. Alonso-Izquierdo. "Kink dynamics in a system of two coupled scalar fields in two space-time dimensions". In: *Physica D* 365 (Feb. 2018), pp. 12–26. DOI: 10.1016/j.physd.2017.10.006. URL: https://www.sciencedirect.com/science/article/pii/S0167278917303159.

[87] G. A. Tsolias et al. "Kink-antikink interaction forces and bound states in a ϕ^4 model with quadratic and quartic dispersion". In: *J Phys. A: Math. Theor.* 54 (May 2021), p. 225701. DOI: 10.1088/1751-8121/abf611. URL: https://iopscience.iop.org/article/10.1088/1751-8121/abf611.

[88] Sergey V. Dmitriev, Yuri S. Kivshar, and Takeshi Shigenari. "Fractal structures and multiparticle effects in soliton scattering". In: *Phys. Rev. E* 64 (5 Oct. 2001), p. 056613. DOI: 10.1103/PhysRevE.64.056613. URL: https://link.aps.org/doi/10.1103/PhysRevE.64.056613.

[89] Helge Frauenkron, Yuri S. Kivshar, and Boris A. Malomed. "Multisoliton collisions in nearly integrable systems". In: *Phys. Rev. E* 54 (3 Sept. 1996), R2244–R2247. DOI: 10.1103/PhysRevE.54.R2244. URL: https://link.aps.org/doi/10.1103/PhysRevE.54.R2244.

[90] S.V. Dmitriev et al. "Dislocation nucleation mechanism in a one-dimensional model of a Frenkel-Kontorova crystal". In: *Russ. Phys. J.* 39 (Feb. 1996), pp. 164–167. DOI: 10.1007/BF02067682. URL: https://link.springer.com/article/10.1007/BF02067682#citeas.

[91] S. V. Dmitriev et al. "Effect of discreteness on a sine-Gordon three-soliton solution". In: *Phys. Lett. A* 246 (1-2 Sept. 1998), pp. 129–134. DOI: 10.1016/S0375-9601(98)00459-9. URL: https://www.sciencedirect.com/science/article/pii/S0375960198004599.

[92] A. E. Miroshnichenko et al. "Inelastic three-soliton collisions in a weakly discrete sine-Gordon system". In: *Nonlinearity* 13 (3 2000), p. 837. DOI: 10.1088/0951-7715/13/3/318. URL: https://iopscience.iop.org/article/10.1088/0951-7715/13/3/318.

[93] S. V. Dmitriev et al. "Kink-breather solution in the weakly discrete Frenkel-Kontorova model". In: *Phys. Rev. E* 61 (5 May 2000), pp. 5880–5885. DOI: 10.1103/PhysRevE.61.5880. URL: https://link.aps.org/doi/10.1103/PhysRevE.61.5880.

[94] Sergey V. Dmitriev et al. "Chaotic character of two-soliton collisions in the weakly perturbed nonlinear Schrödinger equation". In: *Phys. Rev. E* 66 (4 Oct. 2002), p. 046609. DOI: 10.1103/PhysRevE.66.046609. URL: https://link.aps.org/doi/10.1103/PhysRevE.66.046609.

[95] S. V. Dmitriev et al. “Two-soliton collisions in a near-integrable lattice system”. In: *Phys. Rev. E* 68 (5 Nov. 2003), p. 056603. DOI: 10.1103/PhysRevE.68.056603. URL: https://link.aps.org/doi/10.1103/PhysRevE.68.056603.

[96] Yi Zhu, Richard Haberman, and Jianke Yang. “Universal Map for Fractal Structures in Weak Interactions of Solitary Waves”. In: *Phys. Rev. Lett.* 100 (14 Apr. 2008), p. 143901. DOI: 10.1103/PhysRevLett.100.143901. URL: https://link.aps.org/doi/10.1103/PhysRevLett.100.143901.

[97] W.B. Cardoso and R.M.P. Teixeira. “Scattering of solitons in binary Bose-Einstein condensates with spin-orbit and Rabi couplings”. In: *Nonlinear Dyn.* 96 (Feb. 2019), pp. 1147–1167. DOI: 10.1007/s11071-019-04846-5. URL: https://link.springer.com/article/10.1007/s11071-019-04846-5.

[98] R. J. Dingwall et al. “Non-integrable dynamics of matter-wave solitons in a density-dependent gauge theory”. In: *New J. Phys.* 20 (Apr. 2018), p. 043004. DOI: 10.1088/1367-2630/aab29e. URL: https://iopscience.iop.org/article/10.1088/1367-2630/aab29e/meta.

[99] Chunlei Qu et al. “Magnetic solitons in Rabi-coupled Bose-Einstein condensates”. In: *Phys. Rev. A* 95 (3 Mar. 2017), p. 033614. DOI: 10.1103/PhysRevA.95.033614. URL: https://link.aps.org/doi/10.1103/PhysRevA.95.033614.